

© 2010

Po Ting Lin

ALL RIGHTS RESERVED

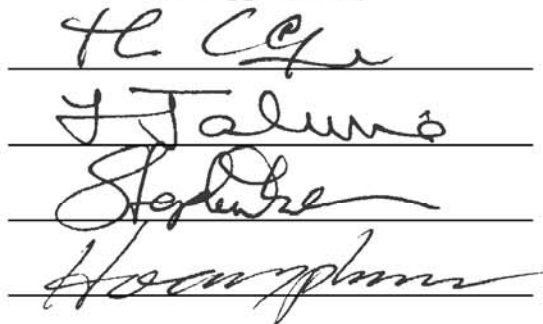
# PARAMETRIC MODELING AND OPTIMIZATION OF THERMAL SYSTEMS WITH DESIGN UNCERTAINTIES

By

PO TING LIN

A dissertation submitted to the  
Graduate School-New Brunswick  
Rutgers, The State University of New Jersey  
in partial fulfillment of the requirements  
for the degree of  
Doctor of Philosophy  
Graduate Program in Mechanical and Aerospace Engineering  
written under the direction of  
Professor Yogesh Jaluria and Professor Hae Chang Gea

and approved by

The block contains four handwritten signatures, each written on a horizontal line. From top to bottom, the signatures are: 1. A signature that appears to be 'H. C. Gea'. 2. A signature that appears to be 'Y. Jaluria'. 3. A signature that appears to be 'Stephen'. 4. A signature that appears to be 'H. C. Gea'.

New Brunswick, New Jersey

May, 2010

# **ABSTRACT OF THE DISSERTATION**

## **Parametric Modeling and Optimization of Thermal Systems with Design Uncertainties**

by Po Ting Lin

Dissertation Director:

Professor Yogesh Jaluria

Professor Hae Chang Gea

Thermal systems play significant roles in the engineering practices and our lives. To improve those thermal systems, it is necessary to model and optimize the operating conditions. More importantly, the design uncertainties should be considered because the failures of the thermal systems may be very dangerous and produce large loss. This study focuses on the parametric modeling and the optimization of the thermal systems with the considerations of the design uncertainties. As an example, the material processing thermal system, the Chemical Vapor Deposition (CVD), is simulated with different inlet velocities and susceptor temperatures. Several responses are considered to represent the

performance of the thin-film deposition, including the percentage of the working area, the mean of the deposition rate, the root mean square of the deposition, and the surface kurtosis. Those responses are then parametrically modeled by one of the Response Surface Method (RSM), the Radial Basis Function (RBF), and utilized to formulate the optimization problems to enhance the system performances. However, it is not until the design uncertainties are considered that the thermal system designs have high risk of the violations of the performance constraints. One of the Reliability-Based Design Optimization (RBDO) algorithms, the Reliability Index Approach (RIA), is used to solve the optimization problems with the design uncertainties. However, the algorithm suffers from a convergence problem when the design point falls into the infeasible domain during the optimization process. A Modified Reliability Index Approach (MRIA) is proposed with a modified definition of the reliability index, and utilized to solve the RBDO problems of the CVD process. The MRIA converts the design space to the standard normal space and finds the Most Probable Points (MPPs) to evaluate the failure probabilities of the performance constraints. The probabilistic optimization problem is then solved using the approximate probabilistic constraints generated in terms of the MPPs. The MRIA has been used to solve several different optimization formulations with both normally and lognormally distributed random variables. The Monte Carlo Simulation (MCS) results verify that the optimal solutions have acceptable failure probabilities. As a result, the proposed strategy of parametrically modeling and optimizing with design uncertainties can be applied to the experiments or the simulations of other thermal systems to improve their productivity, maintain the quality control, and reduce the probability of system failure.

## Acknowledgments

This dissertation was accomplished with the kind help from lots of people. My genuine appreciation comes to my thoughtful advisors, Dr. Yogesh Jaluria and Dr. Hae Chang Gea. With their invaluable guidance, they helped me through some difficult circumstances. This dissertation cannot be possible without their dedicated supports. With their constant advice, I was able to focus on my project throughout my academic years. I am grateful to all the committee members for the review. I would like to extend my grateful appreciation to Dr. Stephen Tse and Dr. Hoang Pham for their valuable comments. Thank you for giving me lots of useful advices to my research.

My appreciation goes to my lab mates at Mechanical and Aerospace Engineering, Rutgers University: Dr. Ching Jui (Ray) Chang, Dr. Bin Zheng, Eui Hark Lee, Wei Song, Xiao Bao Liu, Zhe Qi Lin, Xi Ke Zhao, Yan Ju Liu, Hui Hui Qi, Xiao Ling Zhang, Jian Tao Liu, and Yi Ru Ren. Their physical and mental supports push me forward. I would also like to give my great appreciation to my colleges at Mechanical and Aerospace Engineering, Rutgers University: Yuan Ping Chen, Wei Ju (Lisa) Chen, Chia Ju Lee, Hsiao Fang (Michelle) Lee, and all other colleges that may help me continue my research at some points.

Next, I would like to thank my friends who have joined my “studying group”: Yu Ching (Lisa) Kuo, Dr. Kuen Phon Wu, Yu Ming Chie, Hsiao Fang (Michelle) Lee, Yuan Ping Chen, Yu Chung (Sean) Chang, and Meng Tieh (Evelyn) Fang. Thank you for your

kind supports. Also, I want to send my great appreciation to my roommate, Pei Ming (Nick) Chen. Thank you for your great coffee which refreshes my every morning.

Most importantly, I would like to thank my lovely family: Chu Chin Lin, my dad; Chun Huan Chang, my mom; Chia Hui Lin, my sister; and Po Tsun Lin, my brother. Truly thank you all for your earnest encouragement and devoted support. You all built up my personality, self-confident, and the will to contribute to research. I love you all very much.

Lastly, I want to specially devote my appreciation to my lovely girlfriend, Po Yen (Ariel) Chen. Thank you for your sacrifice, love, and encouragement. It is nearly impossible for me to complete this research work without your accompany.

## **Dedications**

This dissertation is dedicated to my dear family.

# Table of Contents

<b>ABSTRACT OF THE DISSERTATION .....</b>	<b>ii</b>
<b>Acknowledgments.....</b>	<b>iv</b>
<b>Dedications.....</b>	<b>vi</b>
<b>List of Figures.....</b>	<b>x</b>
<b>List of Tables.....</b>	<b>xii</b>
<b>Nomenclature.....</b>	<b>xiii</b>
<b>Chapter 1. Introduction .....</b>	<b>1</b>
1.1. Motivation and Objective .....	1
1.2. Literature Reviews.....	3
1.2.1. Different Thermal Systems .....	3
1.2.2. Chemical Vapor Deposition Processes .....	11
1.2.3. Design of the CVD Process .....	19
1.3. Research Contributions .....	24
1.4. Overview of the Dissertation .....	26
<b>Chapter 2. Simulation and Responses of the CVD Process .....</b>	<b>29</b>
2.1. Introduction .....	29
2.2. Simulation of the CVD Process .....	29
2.3. Simulation Validation.....	34
2.4. Function Formulations of the Responses in CVD Process .....	37
2.4.1. Percentage of Working Area (PWA) .....	37
2.4.2. Mean of Deposition Rate (MDR).....	39
2.4.3. Root Mean Square (RMS) .....	40
2.4.4. Surface Kurtosis (KUR).....	42
2.5. Conclusion and Remarks .....	43
<b>Chapter 3. Parametric Modeling of the CVD Process .....</b>	<b>45</b>
3.1. Introduction .....	45
3.2. Review of Parametric Modeling Techniques .....	45
3.2.1. Polynomial Response Surface (PRS).....	47
3.2.2. Kriging.....	48
3.2.3. Geometric Modeling Curves and Surfaces .....	50
3.3. Radial Basis Function (RBF).....	52
3.3.1. Formulation of the RBF .....	52
3.3.2. Model Validation .....	53
3.4. Conclusion and Remarks .....	59



<b>Chapter 4. Optimization of the CVD Process .....</b>	<b>61</b>
4.1. Introduction .....	61
4.2. Problem Formulations.....	61
4.2.1. Example 1: Maximizing the PWA .....	62
4.2.2. Example 2: Maximizing the MDR.....	64
4.2.3. Example 3: A Multi-Objective Formulation .....	65
4.2.4. Example 4: Maximizing the PWA Subject to Constraint of Deposition Rate.....	67
4.2.5. Example 5: Maximizing the MDR Subject to Constraint of Working Area .....	68
4.2.6. Results.....	69
4.3. Optimization with Design Uncertainties.....	71
4.4. Conclusion and Remarks .....	72
<b>Chapter 5. Reliability-Based Design Optimization (RBDO) .....</b>	<b>74</b>
5.1. Introduction .....	74
5.2. Early Definitions of Reliability Indices .....	75
5.2.1. Cornell Reliability Index.....	75
5.2.2. Chance Constrained Programming (CCP) .....	77
5.2.3. Veneziano Reliability Index .....	79
5.3. Reliability Index Approach (RIA) .....	79
5.3.1. Hasofer-Lind Reliability Index .....	80
5.3.2. Most Probable Point (MPP)-Searching Algorithms.....	82
5.4. Other RBDO Algorithms .....	85
5.5. Convergence Problem of Traditional Reliability Index Approach (TRIA) .....	86
5.6. Conclusion and Remarks .....	90
<b>Chapter 6. Modified Reliability Index Approach (MRIA) for RBDO .....</b>	<b>92</b>
6.1. A New Reliability Index .....	92
6.1.1. Definition of the Modified Reliability Index .....	92
6.1.2. Implementation of MRIA .....	95
6.2. Numerical Examples.....	98
6.2.1. Example 6: Linear Mathematical Problem .....	98
6.2.2. Example 7: Nonlinear Mathematical Problem.....	102
6.3. MRIA with Non-Normally Distributed Random Variables .....	105
6.4. Conclusion and Remarks .....	110
<b>Chapter 7. RBDO of the CVD Process .....</b>	<b>112</b>
7.1. Introduction .....	112
7.2. RBDO Problems of the CVD Process with Normally Distributed Random Variables .....	113
7.2.1. Example 1: Maximizing the PWA .....	114
7.2.2. Example 2: Maximizing the MDR.....	115
7.2.3. Example 3: A Multi-Objective Formulation .....	116
7.2.4. Example 4: Maximizing the PWA Subject to Constraint of Deposition Rate.....	118
7.2.5. Example 5: Maximizing the MDR Subject to Constraint of Working Area .....	119
7.3. RBDO Problems of the CVD Process with Lognormally Distributed Random Variables.....	120
7.3.1. Example 1: Maximizing the PWA .....	121
7.3.2. Example 2: Maximizing the MDR.....	123
7.3.3. Example 3: A Multi-Objective Formulation .....	123

7.3.4. Example 4: Maximizing the PWA Subject to Constraint of Deposition Rate.....	126
7.3.5. Example 5: Maximizing the MDR Subject to Constraint of Working Area .....	126
7.4. Results .....	129
7.5. Conclusion and Remarks .....	130
<b>Chapter 8. Conclusion and Future Work.....</b>	<b>132</b>
8.1. Summary .....	132
8.2. Future Work.....	135
<b>Appendices .....</b>	<b>137</b>
<b>References .....</b>	<b>144</b>
<b>Acknowledgment for Previous Publications .....</b>	<b>152</b>
<b>Index .....</b>	<b>153</b>
<b>Curriculum Vitae .....</b>	<b>155</b>

# List of Figures

Figure 1.1. Different Types of Thermal Systems. ....	5
Figure 1.2. Schematic Sequence of Steps in CVD Process (Adapted from [18]).....	12
Figure 1.3. Different Applications of the CVD process. ....	13
Figure 1.4. Different Configurations of the CVD Reactors (Adapted from [18]). ....	18
Figure 1.5. Flowchart of the Proposed Research.....	25
Figure 2.1. Vertical Impinging CVD Reactor [41].....	30
Figure 2.2. Boundary Conditions of the Simulation for the Vertical CVD Reactor.....	32
Figure 2.3. A Typical Result of the Streamlines of the Flow.....	33
Figure 2.4. A Typical Result of the Temperature Distribution.....	33
Figure 2.5. Scheme of the Deposition Profile of Silicon.....	33
Figure 2.6. Horizontal CVD Reactor [41].....	34
Figure 2.7. Deposition Rate of Silicon in the Horizontal CVD Reactor Compared with Others [41, 45, 50, 56, 63]. ....	35
Figure 2.8. Mass Diffusivity of Silane with Different Temperature Exponent Compared with FLUENT database.....	36
Figure 2.9. Growth Rate of Silicon in the Horizontal CVD Reactor with Different Mass Diffusivity. ....	37
Figure 2.10. Deposition Profiles with Different PWA. ....	39
Figure 2.11. Deposition Profiles with Different RMS.....	41
Figure 2.12. Deposition Profiles with Different KUR.....	42
Figure 3.1. Sampling Data Sets.....	55
Figure 3.2. Response Surfaces of the PWA. ....	57
Figure 3.3. Response Surfaces of the MDR. ....	58
Figure 3.4. Response Surfaces of the RMS.....	58
Figure 3.5. Response Surfaces of the KUR.....	59
Figure 4.1. Optimal Solution of Maximizing the PWA. ....	63
Figure 4.2. Optimal Solution of Maximizing the MDR. ....	65
Figure 4.3. Optimal Solution of the Multi-Objective Formulation. ....	66
Figure 4.4. Optimal Solution of Maximizing the PWA Subject to the MDR Constraint. ....	68
Figure 4.5. Optimal Solution of Maximizing the MDR Subject to the PWA Constraint. ....	69
Figure 5.1. Scheme of Three Different Kinds of the Reliability Indices: Cornell, Veneziano, and Hasofer-Lind Reliability Indices.....	81
Figure 5.2. PDF of the Normally Distributed Random Variable, X.....	88
Figure 5.3. PDF of the Standard-Normally Distributed Random Variable, U. ....	88
Figure 5.4. PDF of the Standard-Normally Distributed Random Variable, U. ....	90
Figure 6.1. Flowchart of the MRIA.....	97

Figure 6.2. Iteration Process of Example 6 Using MRIA with an Initial Design (5, 5). .....	99
Figure 6.3. Iteration Process of Example 6 Using TRIA with an Initial Design (2, 2). .....	100
Figure 6.4. Iteration Process of Example 6 Using MRIA with an Initial Design (2, 2). .....	100
Figure 6.5. Iteration Process of Example 7 with an Initial Design (5, 5). .....	103
Figure 6.6. Iteration Process of Example 7 with the Lognormally Distributed Initial Design (5, 5).....	108
Figure 7.1. Optimal Solution of Maximizing the PWA with Normally Distributed Random Variables....	115
Figure 7.2. Optimal Solution of Maximizing the MDR with Normally Distributed Random Variables. ..	116
Figure 7.3. Optimal Solution of the Multi-Objective Formulation with Normally Distributed Random Variables. ....	117
Figure 7.4. Optimal Solution of Maximizing the PWA Subject to the MDR Constraint with Normally Distributed Random Variables.....	119
Figure 7.5. Optimal Solution of Maximizing the MDR Subject to the PWA Constraint with Normally Distributed Random Variables.....	120
Figure 7.6. Optimal Solution of Maximizing the PWA with Lognormally Distributed Random Variables. .....	122
Figure 7.7. Optimal Solution of Maximizing the MDR with Lognormally Distributed Random Variables. ....	124
Figure 7.8. Optimal Solution of the Multi-Objective Formulation with Lognormally Distributed Random Variables.....	125
Figure 7.9. Optimal Solution of Maximizing the PWA Subject to the MDR Constraint with Lognormally Distributed Random Variables.....	127
Figure 7.10. Optimal Solution of Maximizing the MDR Subject to the PWA Constraint with Lognormally Distributed Random Variables. ....	128

## List of Tables

Table 1.1.	Common Materials in Different Applications of the CVD Processes [18, 24-33].	15
Table 1.2.	Different Types of the CVD Processes.	17
Table 1.3.	Typical Design Variables and Responses in the CVD Designs [18, 28, 43-46].	21
Table 2.1.	Conditions and Uniformity Factors of Samples (1) to (6).	43
Table 3.1.	Different RSM Methods [1, 82-84].	46
Table 3.2.	Typical Coefficients for Polynomial Response Surface.	47
Table 3.3.	Common Covariance Functions for Different Kriging Techniques.	51
Table 3.4.	Sampling Data Sets: 9 Points, 13 Points, and 25 Points.	54
Table 4.1.	Optimal Solutions and the Corresponding Responses for Examples 1 to 5 with the 25-Point RBF Models and the 437-Sampling Simulations.	70
Table 4.2.	Monte Carlo Simulations at the Optimal Solutions with Design Uncertainties, $\sigma_v = 0.02$ and $\sigma_T = 20$ , for Examples 1 to 5.	72
Table 6.1.	Comparison of TRIA and MRIA in Example 6.	101
Table 6.2.	Comparison of TRIA and MRIA in Example 6.	101
Table 6.3.	Results of Example 7.	104
Table 6.4.	Comparison of TRIA and MRIA in Example 7.	105
Table 6.5.	Results of Example 3.	108
Table 6.6.	Comparison of TRIA and MRIA in Example 3.	109
Table 7.1.	The Optimal Solutions, the Corresponding Responses, and the Monte Carlo Simulation Results for Examples 1 to 5 with the Normally and the Lognormally Distributed Random Variables.	130
Table I.1.	Responses of the 437 Sampling Points.	137

## Nomenclature

$A$  = The pre-exponential factor for Arrhenius rate.

$A(\mathbf{x}^S)$  = A  $M \times K$  matrix of monomials for the Response Surface Method (RSM), whose  $s^{th}$  row is a  $1 \times K$  vector,  $\mathbf{B}^T(\mathbf{x}_s^S)$  ;

$$A(\mathbf{x}^S) = A_{st} \mathbf{e}_s \mathbf{e}_t = \sum_{s=1}^M \mathbf{B}^T(\mathbf{x}_s^S) \mathbf{e}_s = \sum_{s=1}^M \sum_{t=1}^K B_t(\mathbf{x}_s^S) \mathbf{e}_s \mathbf{e}_t .$$

$\mathbf{B}(\mathbf{x})$  = A combination of the monomials for the RSM;  $\mathbf{B}(\mathbf{x}) = B_t(\mathbf{x}) \mathbf{e}_t$  written in the Einstein notation.

$\mathbf{C}_x(\mathbf{x}, \mathbf{x}^S)$  = A vector of the covariance functions for Kriging;

$$\mathbf{C}_x(\mathbf{x}, \mathbf{x}^S) = \sum_{s=1}^M C_{x,s}(\mathbf{x}, \mathbf{x}_s^S) \mathbf{e}_s = \sum_{s=1}^M Cov(\mathbf{x}, \mathbf{x}_s^S) \mathbf{e}_s .$$

$\mathbf{C}(\mathbf{x}^S)$  = A matrix of the covariance functions for Kriging;

$$\mathbf{C}(\mathbf{x}^S) = \sum_{r=1}^M \sum_{s=1}^M C_{rs}(\mathbf{x}_r^S, \mathbf{x}_s^S) \mathbf{e}_r \mathbf{e}_s = \sum_{r=1}^M \sum_{s=1}^M Cov(\mathbf{x}_r^S, \mathbf{x}_s^S) \mathbf{e}_r \mathbf{e}_s .$$

$Cov(X_p, X_q)$  = The covariance between  $X_p$  and  $X_q$ .

$Cov(\mathbf{x}_r, \mathbf{x}_s)$  = The covariance function between two vectors:  $\mathbf{x}_r, \mathbf{x}_s \in \mathbb{R}^N$ .

$\mathbf{d}$  = The expected value of  $\mathbf{X}$  ;  $\mathbf{d} = E[\mathbf{X}] = d_j \mathbf{e}_j$ .

$\mathbf{d}_Y$  = The expected value of  $\mathbf{Y}$  ;  $\mathbf{d}_Y = E[\mathbf{Y}] = d_{Y,j} \mathbf{e}_j$ .

$D$  = Mass diffusivity of silane.

$D_0$  = The pre-exponential factor in the power law of the mass diffusivity.

$D_i$  = Deposition rate at the  $i^{th}$  sampling node.

$\mathbf{e}_j$  =  $j^{th}$  Normal basis of the design variables.

$\mathbf{e}_r$  =  $r^{th}$  Normal basis of the sampling points.

$\mathbf{e}_s$  =  $s^{th}$  Normal basis of the sampling points.

$E_a$  = The activation energy for Arrhenius rate.

$f_i(\mathbf{x})$  = The Joint Probability Density Function (JPDF) of  $g_i(\mathbf{X})$ .

$F(\mathbf{x})$  = An approximate function by Response Surface Method (RSM).

$F_\eta$  = The function value of a RSM model at  $\mathbf{x}_\eta$ ;  $F_\eta = F(\mathbf{x}_\eta)$ .

$\mathbf{F}^S(\mathbf{x}^S)$  = A vector of the responses in terms of the sampling points;

$$\mathbf{F}^S(\mathbf{x}^S) = \sum_{s=1}^M F_s^S(\mathbf{x}_s^S) \mathbf{e}_s = \sum_{s=1}^M F(\mathbf{x}_s^S) \mathbf{e}_s.$$

$F_X(\mathbf{x})$  = The Cumulative Distribution Function (CDF);  $F_X(\mathbf{x}) = P[\mathbf{X} \leq \mathbf{x}]$ .

$F_U(\mathbf{u})$  = The Standard Normal CDF;  $F_U(\mathbf{u}) = P[U \leq \mathbf{u}] = \Phi(\mathbf{u})$ .

$G_\eta$  = The simulated response in terms of  $\mathbf{x}_\eta$ .

$g_i = i^{th}$  Constraint;  $g_i(\mathbf{X}) > 0$  is considered as the failed design and  $g_i(\mathbf{X}) \leq 0$  represents the feasible domain.

$h$  = The index of the important sampling points;  $0 < \text{size of } h < N$ .

$i$  = The dimensional index of the constraint;  $i = 1, 2, \dots, n$ .

$j$  = The dimensional index of the design variable;  $j = 1, 2, \dots, N$ .

$k$  = The iteration index of the global optimization loop.

$K$  = The number of the parameters to be determined in a best fitting model;  $K < M$ .

$m$  = The iteration index of the MPP-searching sub-problem.

$M$  = The number of the sampling points.

$n$  = The number of the constraints.

$N$  = The number of the design variables.

$N(\mu, \sigma)$  = A normal distribution with the mean,  $\mu$ , and the standard deviation,  $\sigma$ .

$p$  = A dummy index;  $p = 1, 2, \dots, N$ .

$P[\bullet]$  = The probability of an event.

$P_{f,i}$  = The allowable failure probability with respect to  $i^{th}$  constraint.

$q$  = A dummy index;  $q = 1, 2, \dots, N$ .

$Q$  = The number of the uniformly distributed sampling nodes within the effective working area.

$r$  = A dummy index;  $r = 1, 2, \dots, M$ .

$R$  = The universal gas constant.

$s$  = A dummy index;  $s = 1, 2, \dots, M$ .

$S$  = The local slope between two nodes in the deposition profile from the numerical simulation.

$S_U$  = The acceptable limit of the local slope in the deposition profile.

$t$  = A dummy index;  $t = 1, 2, \dots, K$ .

$T$  = The susceptor temperature of the Chemical Vapor Deposition (CVD) process.

$T^*$  = The optimal susceptor temperature.

$T_L$  = The lower bound of the susceptor temperature.

$T_m$  = The maximum susceptor temperature.

$T_s^S = s^{th}$  Sampling susceptor temperature.

$T_U$  = The upper bound of the susceptor temperature.

$\mathbf{u}$  = The deterministic standard normal design variable;  $\mathbf{u} = u_j \mathbf{e}_j$  and

$$u_j = (x_j - d_j) / \sigma_j.$$

$\mathbf{u}^*$  = The Most Probable Point (MPP);  $\mathbf{u}^* = u_j^* \mathbf{e}_j$ .

$u_a$  = An active standard normal design variable;  $u_a = (x_a - d) / \sigma$ .

${}^\perp \mathbf{u}_i^{(m)}$  = The foot of the perpendicular from the origin to the linear constraint in standard normal space;  ${}^\perp \mathbf{u}_i^{(m)} = {}^\perp u_{i,j}^{(m)} \mathbf{e}_j$

$\mathbf{U}$  = The random standard normal design variable;  $\mathbf{U} = U_j \mathbf{e}_j$ .

$V$  = The inlet velocity of the CVD process.

$V^*$  = The optimal inlet velocity.

$V_L$  = The lower bound of the inlet velocity.

$V_m$  = The maximum inlet velocity.



$V_s^S = s^{th}$  Sampling inlet velocity.

$V_U$  = The upper bound of the inlet velocity.

$\mathbf{w}$  = The coefficients of the RSM models;  $\mathbf{w} = w_r \mathbf{e}_r$  for the exact fitting  
and  $\mathbf{w} = w_t \mathbf{e}_t$  for the best fitting.

$\mathbf{x}$  = The deterministic design variable;  $\mathbf{x} = x_j \mathbf{e}_j$ .

$\mathbf{x}^S$  = The sampling points;  $\mathbf{x}^S = x_{j,s}^S \mathbf{e}_j \mathbf{e}_s$  where  $x_{j,s}^S$  is the  $j^{th}$  design  
variable in the  $s^{th}$  sampling.

$\mathbf{x}_s^S$  = A vector of the  $s^{th}$  design sampling points;  $\mathbf{x}_s^S = x_{j,s}^S \mathbf{e}_j$ .

$x_a$  = An active design variable.

$\mathbf{x}_T$  = A design point for Taylor expansion;  $\mathbf{x}_T = x_{T,j} \mathbf{e}_j$ .

$\mathbf{x}_\eta = \eta^{th}$  Design variable for the model validation;  $\mathbf{x}_\eta = x_{\eta,j} \mathbf{e}_j$ .

$\mathbf{X}$  = The random design variable;  $\mathbf{X} = X_j \mathbf{e}_j$ .

$\mathbf{y}$  = The deterministic design variable;  $\mathbf{y} = y_j \mathbf{e}_j$ .

$\mathbf{Y}$  = The random design variable;  $\mathbf{Y} = Y_j \mathbf{e}_j$ .

$z$  = The cost function.

$err$  = The error measurement for the model validation.

EWA = The effective working area.

KUR = The Surface kurtosis of the deposition profile in the EWA.

$KUR_U$  = The upper bound of the KUR.

MDR = The mean of the deposition rate in the EWA.

$MDR_L$  = The lower bound of the MDR.

$LogN(\mu, \sigma)$  = A lognormal distribution with the mean,  $\mu$ , and the standard  
deviation,  $\sigma$ .

PWA = The percentage of the working area.

$PWA_L$  = The lower bound of PWA.

RMS = The root mean square of the deposition profile in the EWA.

$RMS_U$  = The upper bound of RMS.

$\alpha$  = The temperature exponent for the Arrhenius rate.

$\beta_C$  = The Cornell reliability index.

$\beta_{HL}$  = The Hasofer-Lind reliability index.

$\beta_{HL,f}$  = The Allowable Hasofer-Lind reliability index.

$\beta_M$  = The modified reliability index.

$\beta_{M,f}$  = The allowable modified reliability index.

$\beta_V$  = The Veneziano reliability index.

$\gamma$  = The temperature exponent for the mass diffusivity of the silane.

$\gamma_h$  = The parameter for the smoothness of the distance function.

$\delta_{pq}$  = The Kronecker delta;  $\delta_{pq} = 1$  if  $p = q$  otherwise  $\delta_{pq} = 0$ .

$\eta$  = The index of the design variable for the model validation;

$\eta = 1, 2, \dots, 437$ .

$\theta_j$  = Unknown parameters for the Gaussian correlation functions.

$\iota$  = The index of the uniformly distributed sampling nodes;  $\iota = 1, 2, \dots, Q$ .

$\kappa$  = The Arrhenius rate.

$\lambda$  = The Lagrangian multiplier.

$\boldsymbol{\mu}_i^{(m)}$  = A normalized vector of the gradient of the  $i^{th}$  constraint in the

$\mathbf{u}$ -space in the  $m^{th}$  iteration;  $\boldsymbol{\mu}_i^{(m)} = \nabla_{\mathbf{u}} g_i(\mathbf{u}_i^{(m)}) \left\| \nabla_{\mathbf{u}} g_i(\mathbf{u}_i^{(m)}) \right\|^{-1}$ .

$\nu_i^{(m)}$  = The coefficient of the updating scheme for the  $i^{th}$  constraint in the

$m^{th}$  iteration using the H-L iterative algorithm.

$\boldsymbol{\sigma}$  = The standard deviation of  $\mathbf{X}$ ;  $\boldsymbol{\sigma} = \sum_{j=1}^N \sigma_j \mathbf{e}_j \mathbf{e}_j$ .

$\boldsymbol{\sigma}_Y$  = The standard deviation of  $\mathbf{Y}$ ;  $\boldsymbol{\sigma}_Y = \sum_{j=1}^N \sigma_{Y,j} \mathbf{e}_j \mathbf{e}_j$

$\sigma^S$  = The standard deviation of the responses by the sampling points.

$\Sigma$  = A covariance matrix of the random variable,  $\mathbf{X}$  ;

$$\Sigma = \sum_{p=1}^N \sum_{q=1}^N Cov(X_p, X_q) \mathbf{e}_p \mathbf{e}_q^T \text{ and } \Sigma = \sigma^2 \text{ when } \mathbf{X} \text{ is mutually}$$

independent.

$\tau$  = The temperature for Arrhenius rate.

$\Phi$  = The Standard Normal CDF.

## **Chapter 1.**

### **Introduction**

This study presents the parametric modeling and the optimization of the thermal systems with the design uncertainties. The responses of the thermal systems are firstly parametrically modeled by the Radial Basis Functions (RBFs) and then utilized to formulate the optimization problems to enhance the system performances. Moreover, the Reliability-Based Design Optimization (RBDO) algorithms are used to solve the optimization problems of the thermal systems with the design uncertainties. In this research work, a Modified Reliability Index Approach (MRIA) is proposed to solve the RBDO problems without any convergence problems from which the Traditional Reliability Index Approach (TRIA) suffers. Session 1.1 presents the motivation, the objective and the scope of the proposed research. Session 1.2 contains the literature reviews in the related aspects of the proposed research. The research contributions are illustrated in Session 1.3 while the overview of the dissertation is shown in Session 1.4.

#### ***1.1. Motivation and Objective***

Thermal systems not only have been essential technologies in engineering practices but also play significant roles in our lives. With the continuously growing needs of the thermal systems in many different applications, such as power systems, air conditioning, energy conversion, chemical processing, material processing, aerospace,

and automobiles, the design and the optimization of the thermal systems have become very important research works in the engineering field.

The thermal systems are often very complicated because of the complex physics and mechanics involved in the systems, including fluidic mechanics, heat transfer, mass transfer, and chemical reactions. It is nearly impossible to realize the closed-form relationships between the system performances and all the involved variables. Therefore, it is important to firstly understand the basic characteristics of the thermal systems and subsequently determine the principal design variables which dominantly control the system performances.

A systematic strategy is then desired to model and optimize the thermal systems. This proposed strategy must be able to resolve the following questions:

- How to model the system performances in terms of the design variables so that the system performances can be accurately described by the proposed models?
- How to formulate the optimization problems in terms of the defined models for improving the system performances?

In the aspect of the modeling, the mathematical models that are able to quantitatively and literally represent the physical behaviors of the system performances are necessary. With the desired models, the optimization problems can then be formulated to achieve the goals of the thermal system designs.

Unfortunately, the existence of the design uncertainties is unavoidable. A traditional deterministic optimization algorithm often leads the optimal solution to the boundaries of the active constraints. Without the considerations of the design uncertainties, the optimal solution from the deterministic optimization formulation is unreliable and has high probabilities of violating the active constraints. Therefore, additional attentions should be drawn to the optimization problems with the design uncertainties and the following questions should be answered:

- How to formulate a non-deterministic optimization problem when the design variables are uncertain?
- How to solve this non-deterministic optimization problem and how to solve it efficiently?

## ***1.2. Literature Reviews***

In this session, the thermal systems are firstly reviewed. One of the material processing thermal systems, the Chemical Vapor Deposition (CVD), is then reviewed as an example. The design and the optimization of the CVD process are also reviewed.

### **1.2.1. Different Thermal Systems**

As described earlier, the thermal systems are very important in various applications and our lives. To design and optimize the thermal systems, the most fundamental step is to recognize their existence and classify them into different groups in

terms of their functionalities. A common classification of the thermal system is given as follows [1]:

- Manufacturing and materials processing systems.
- Energy systems.
- Cooling systems for electronic equipment.
- Environmental and safety systems.
- Aerospace systems.
- Transportation systems.
- Air conditioning, refrigeration, and heating systems.
- Fluid flow systems and equipment.
- Heat transfer equipment.
- Other thermal systems.

Figure 1.1 illustrates different types of the thermal systems using the classification in Ref. [1]. After understanding the physics and the mechanics behind the thermal systems, the control variables are chosen to determine the system performances. Therefore, the decision of the design variables is the key factor of the modeling and the optimization of the thermal systems.

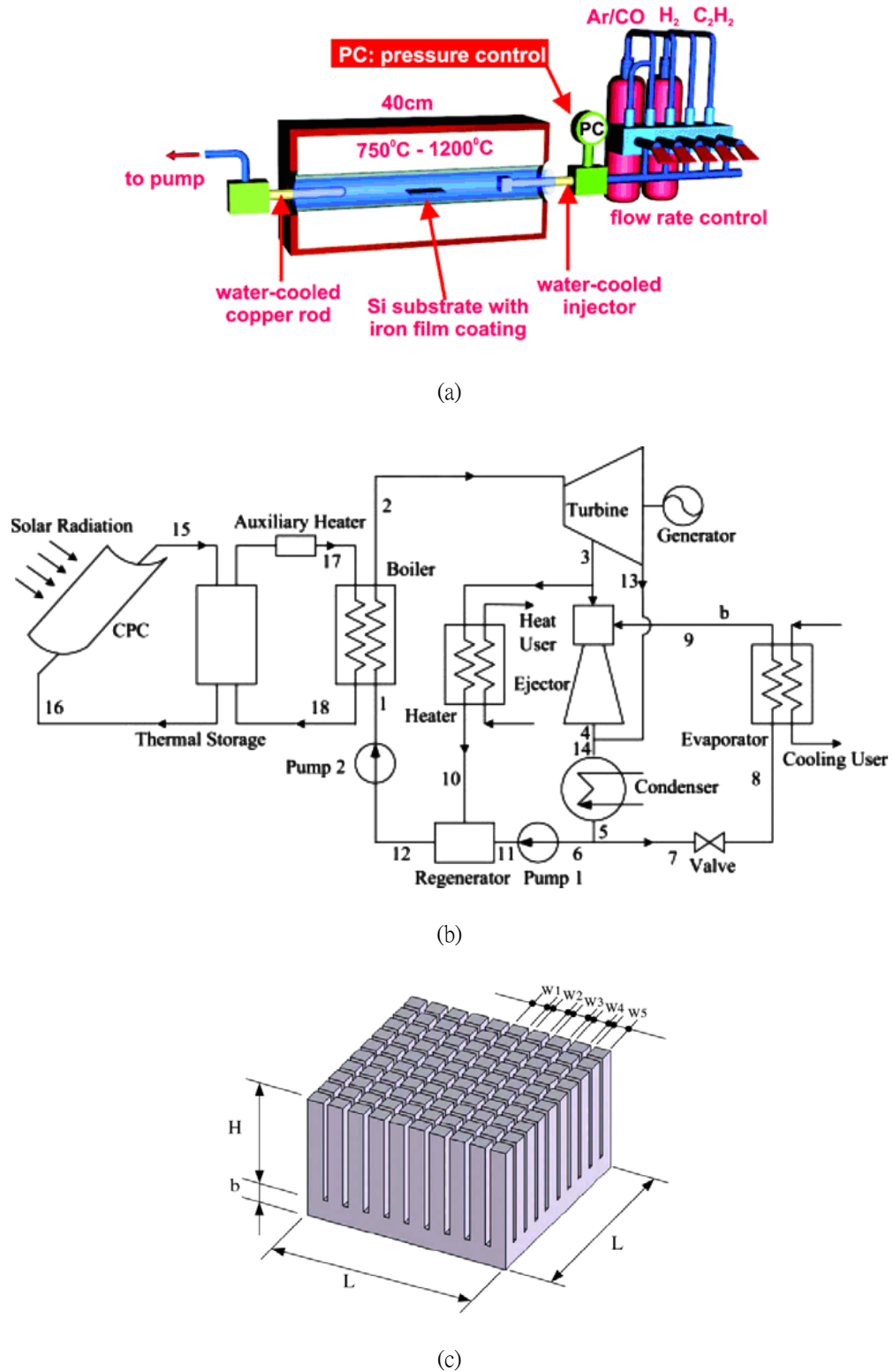
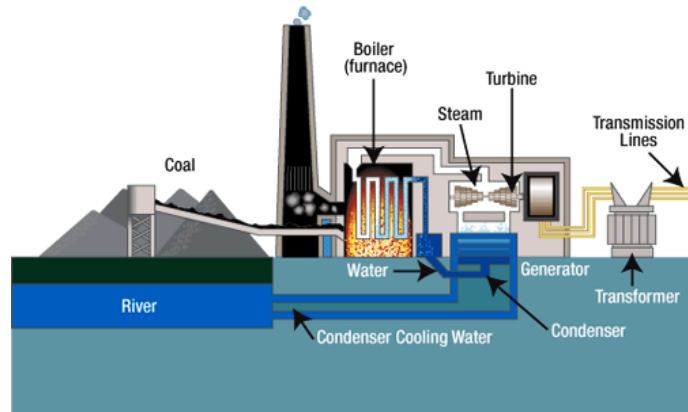


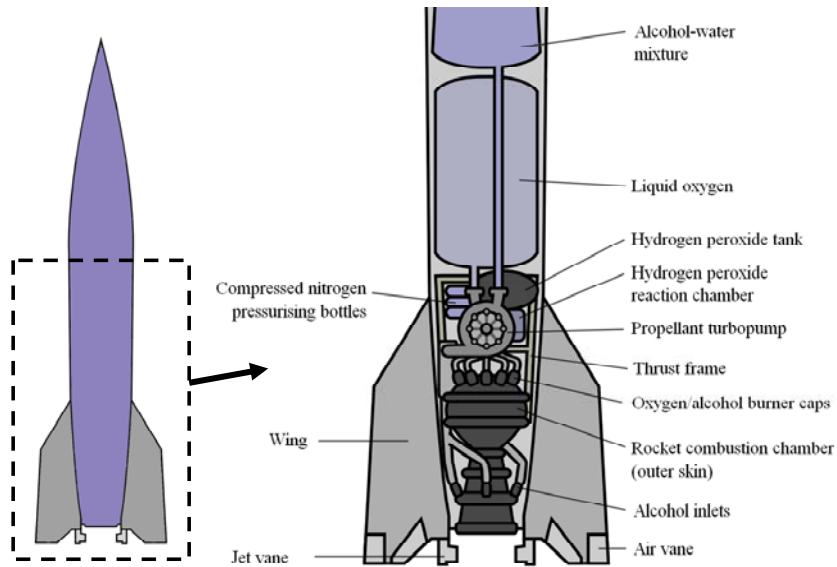
**Figure 1.1. Different Types of Thermal Systems.**

(a) Materials Processing System of Chemical Vapor Deposition [2], (b) Combined Cooling, Heating and Power (CCHP) System by Solar Energy [3], and (c) Heat Sink Design for CPU Cooling [4].

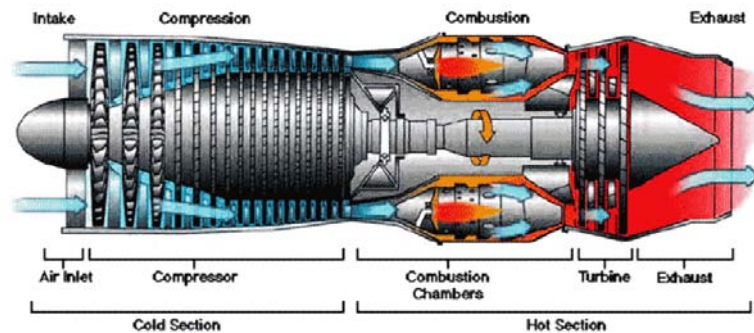




(d)



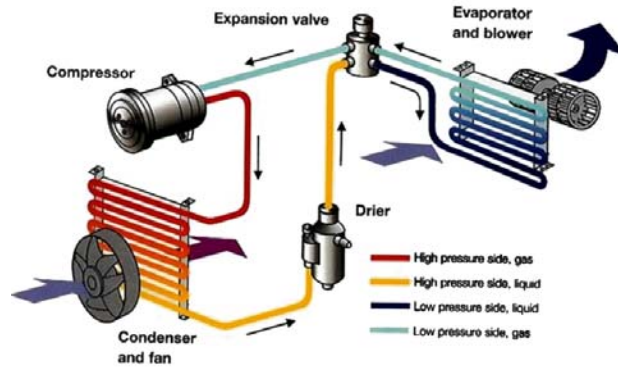
(e)



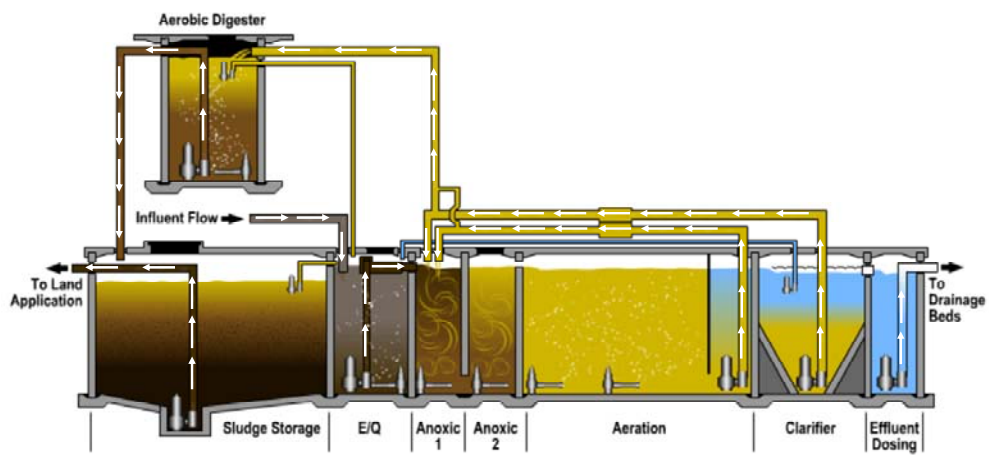
(f)

**Figure 1.1. Different Types of Thermal Systems (Continued).**

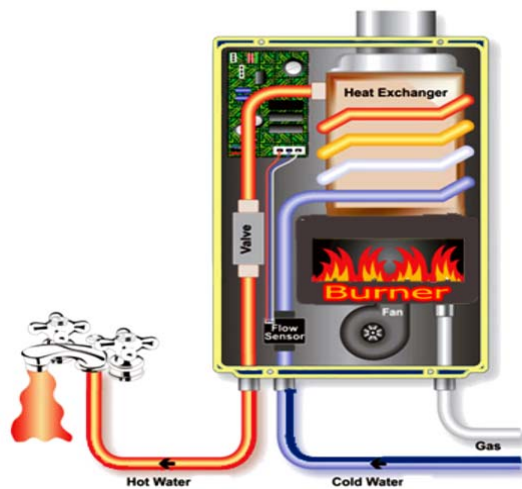
**(d) Heat Rejection System in a Power Plant [5], (e) Aerospace Rocket System (adapted from [6]), and (f) Transportation System of A Turbine Engine [7].**



(g)



(h)



(i)

Figure 1.1. Different Types of Thermal Systems (Continued).

(g) Air Conditioning System [8], (h) Wastewater Treatment System (adapted from[9]), and (i) Heat Exchanger in A Heater [10].

## **Manufacturing and Materials Processing Systems**

Heat transfer plays an important role in the manufacturing and materials processing systems, where the materials often change their mechanical properties due to temperature changes. The controls of the temperature changes determine the productivity and the quality of the processes. Examples include crystal growing, metal casting, metal forming, plastic injection molding, etc. [1] One of those processes, the Chemical Vapor Deposition (CVD) process, will be considered in the later sessions. A systematic strategy to design and optimize the CVD process with design uncertainties will be proposed and it can be applied to the design and the optimization of other thermal systems.

## **Energy Systems**

Energy systems have become one of the most important thermal systems in recent years in which the thermodynamics of the energy conversions are the issues of most concern. Energy systems are often very complicated because they contain several subsystems, such as energy collector, steam generator, turbines, condenser, etc. [11] Numerous design variables should be considered to improve the thermal efficiency of the energy system.

## **Cooling Systems for Electronic Equipment**

Cooling systems are essentially important for electronic equipment where the operating temperatures are constrained within certain allowable temperatures [12]. Other constraints for the cooling systems include the spatial working space, the allowable noise,

etc. The objective of the cooling system design is often minimizing the ratio of used power to reduced temperature, while the design variables are often the geometries of the heat sink which differ the surface area of the heat transfer [4, 13].

### **Environmental and Safety Systems**

Safety is an important factor for systems with extreme environmental conditions, such as high temperature and toxicity. Environmental and safety systems include the applications for heat rejection to air or water, control of the temperature and the pollution of thermal systems, etc. Figure 1.1 (d) demonstrates the heat rejection from a power plant where the heat is dumped to the river as a cooling pond. The operation of the power plant will be under high risks if the safety systems fail. Therefore, the safety system should be taken into careful consideration in the design of the systems with extreme environmental conditions.

### **Aerospace Systems**

Thermal systems are the most important components in aerospace systems, such as rockets, turbines, etc. For the example of a rocket system shown in Figure 1.1 (e), the alcohol/water mixture is pumped into the combustion chamber to heat the fuel and cool the chamber. The balance between the high thrust for launching and the efficient cooling is the focus in the design of the rocket systems.

## **Transportation systems**

Transportation systems cannot operate without the existence of the thermal systems, including diffusion, compression, combustion, turbine, and nozzle systems. Figure 1.1 (f) shows a scheme of the turbine engine where the thrust energy comes from the combustion of the air/fuel mixture. Thermodynamics is significant for the design of the transportation systems [11], while they are often optimized in terms of maximizing the ratio of the generated power to utilized fuel.

## **Air conditioning, Refrigeration, and Heating Systems**

Air conditioning, refrigeration, and heating systems are indispensable to our daily lives. Detailed information about such kind of the thermal systems can be found in Refs. [14-15]. Figure 1.1 (g) shows a scheme of an air conditioning system, where the physical phase, the temperature, and the pressure of the fluid change via the mechanisms of the condenser, the evaporator, and the compressor. The optimization for such thermal systems often focuses on decreasing the power consumption and improving the efficiency of the temperature control.

## **Fluid Flow Systems and Equipment**

Fluid flow systems and equipment include hydraulic components, such as pumps, turbines, compressors, fans, etc. Fluid mechanics is of the major concern in the fluid flow systems and is closely related to the thermal systems with energy transmission, cooling, and mass transfer [16]. Figure 1.1 (h) demonstrates a wastewater treatment

system where the waste water is transferred through several different fluid mechanisms, clarified, and delivered to the drainage system.

### **Heat Transfer Equipment**

Heat transfer systems contain heat exchangers [17], furnaces, heaters, condensers, etc. Figure 1.1 (i) demonstrates an example of the heat exchangers where the heat is transferred to the water and increase its temperature for human usage. The design of the heat exchanging mechanisms considers the transmission of the energy and the control of the heat loss.

There is never a best way to classify all kinds of the thermal system but the most practical ones have been covered and discussed. In the later session, one of the materials processing systems, the CVD process, is taken into consideration. The design and the optimization of the CVD process will be studied and a systematic strategy will be proposed to implement the modeling and the optimization of the CVD process with design uncertainties. The proposed methodology is expected to have the capability of designing and optimizing of the other thermal systems.

#### **1.2.2. Chemical Vapor Deposition Processes**

Chemical Vapor Deposition (CVD) is a process that a solid crystalline or amorphous layer is formed on a heated substrate by chemically reacting premixed gases using the activation energy. Figure 1.2 shows a schematic sequence of the steps of the CVD process. The process involves the transport of reactants to the susceptor, the

chemical reactions and generations of new species, the desorption of the reaction products, and their diffusion back to the main stream [18]. Unlike the cold substrate in the Physical Vapor Deposition (PVD) process [19-20], the one in the CVD process has a higher temperature with a various range from 500 K to 1500 K due to different applications and materials, different types of CVD processes, and different configurations of the CVD reactors. The details about the applications of the CVD processes, different types of the CVD processes, and the configurations of the CVD reactors will be discussed in the following subsession.

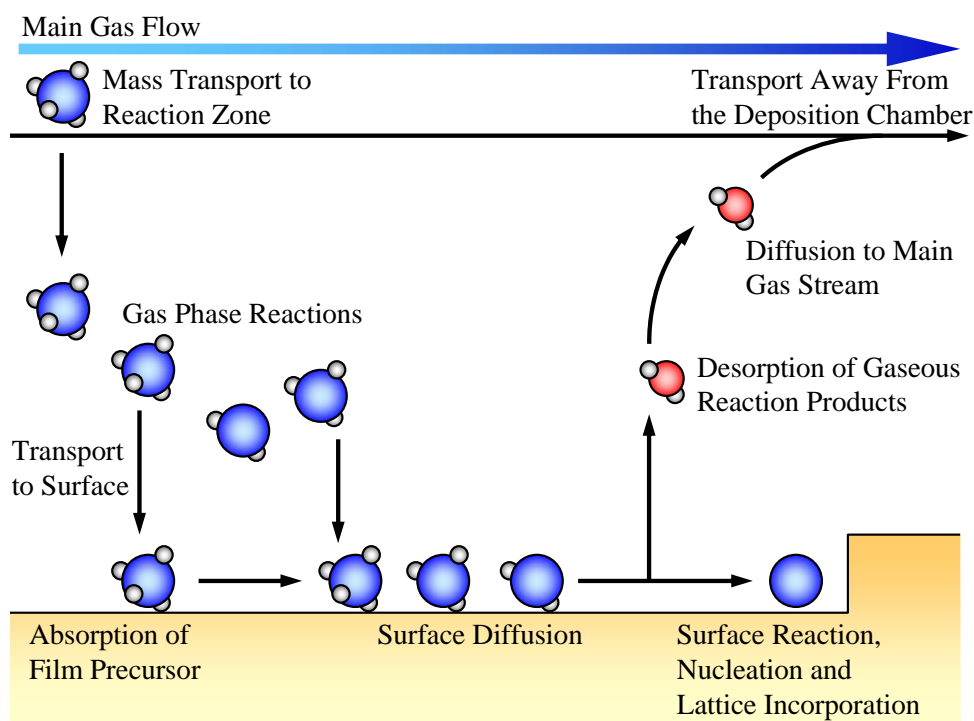
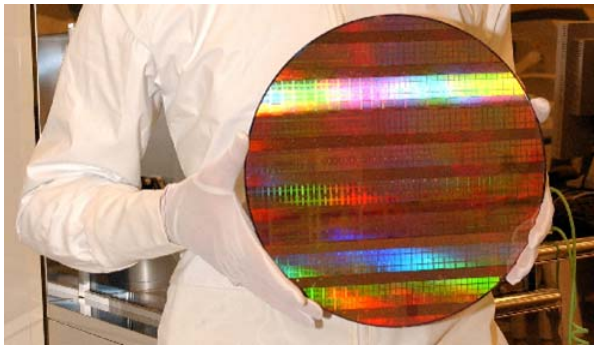


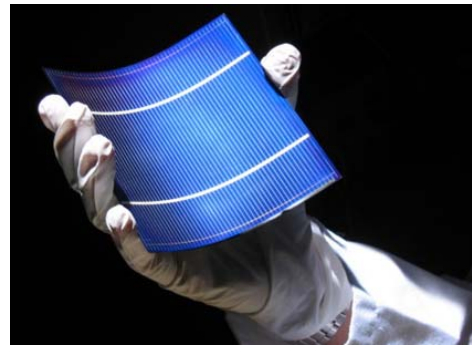
**Figure 1.2. Schematic Sequence of Steps in CVD Process (Adapted from [18]).**

### Different Applications of the CVD Processes

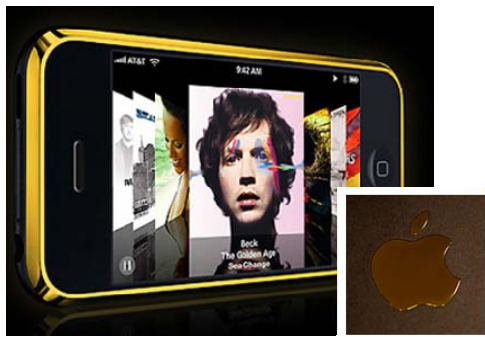
The CVD-based products have become more and more important in our daily lives because of the high quality of the deposited thin layers with various kinds of materials. The CVD process is well utilized to produce highly uniform thin films deposited on different kinds of substrates (typically  $0.01 - 10 \mu\text{m}$ ) [18]. It is used in a wide range of applications where thin coatings of high purity are required. Examples include semi-conductor devices, solar cells, wear resistant coatings, and synthetic growth of crystalline materials, demonstrated in Figure 1.3.



(a)



(b)



(c)



(d)

**Figure 1.3. Different Applications of the CVD process.**

**(a) Integrated Circuits [21], (b) Solar Cells [22], (c) Protective Coatings [23], and (d) Synthetic Diamonds [24].**



The CVD processes can be utilized to produce high-quality microstructures in semiconductors, special materials with dielectric properties as insulators, and metallic conductors with different resistivities. Furthermore, the CVD processes generate high-strength products such as protective coatings, anticorrosive coatings, and ceramic materials. Besides the productions of thin layers, it is possible to generate powers and fibers of different materials by the CVD processes. Other applications such as optical materials and synthetic diamonds have high qualities and purities of different materials. The common materials in different applications of the CVD processes are listed in Table 1.1. Most of the research interests in the later discussions is directed at the CVD of silicon because of its relevance to the semiconductor industry [25-26].

### **Different Types of the CVD Processes**

CVD processes can be classified in terms of their operating conditions or different kinds of instruments. With different operating pressures of the CVD reactors, the CVD processes include three different types:

- Atmospheric Pressure CVD (APCVD).
- Low-Pressure CVD (LPCVD).
- Ultra-High Vacuum CVD (UHVCVD).

The APCVD operates at the pressure of 0.1 – 1 atm while the LPCVD works at a lower pressure of  $10^{-3}$  atm [18]. Other modern CVD processes reach high or ultra-high vacuum (below  $10^{-6}$  Pa) and have high-quality thin-film depositions.

**Table 1.1. Common Materials in Different Applications of the CVD Processes [18, 24-33].**

<b>Different CVD Applications</b>	<b>Common Materials</b>
Semiconductors	Silicon (Si) and gallium arsenide (GaAs)
Dielectrics	Silicon dioxide (SiO <sub>2</sub> ) and silicon nitride (Si <sub>3</sub> N <sub>4</sub> )
Metallic conductors	Tungsten silicide (WSi <sub>2</sub> ), molybdenum silicide (MoSi <sub>2</sub> ), tungsten (W), aluminum (Al), molybdenum (Mo) and polysilicon (Si)
Protective coatings	Titanium nitride (TiN), Tungsten (W), molybdenum (Mo), gold (Au), and platinum (Pt)
Ceramics	Aluminum oxide (Al <sub>2</sub> O <sub>3</sub> ), titanium carbide (TiC), silicon carbide (SiC), boron carbide (B <sub>4</sub> C), and titanium diboride (TiB <sub>2</sub> )
Anticorrosive coatings for turbine blades	Boron nitride (BN), molybdenum disilicide (MoSi <sub>2</sub> ), silicon carbide (SiC), and boron carbide (B <sub>4</sub> C)
Powers for sintering and hot pressing	Silicon nitride (Si <sub>3</sub> N <sub>4</sub> ) and silicon carbide (SiC)
Fibers for composite materials	Boron (B), boron carbide (B <sub>4</sub> C), and silicon carbide (SiC)
High-purity monolithic materials for infrared optics	Zinc selenide (ZnSe), zinc sulfide (ZnS), cadmium sulfide (CdS), and cadmium telluride (CdTe)
Synthetic diamonds	Carbon (C)

Another method to classify the CVD processes considers the operating wall temperature of the CVD chamber. They are:

- Cold-Wall CVD.
- Hot-Wall CVD.

Most of the CVD processes operate with the hot-wall reactors and the gaseous temperature is distributed uniformly inside the reactor. The advantage of the hot-wall

setting is higher deposition rate and better uniformity of the deposition. On the other hand, the cold-wall setting allows higher throughput and easier cleaning but has lower speed of the deposition and poor uniformity of the thin film.

In the consideration of different instruments, a wide variety of CVD processes have been developed, listed in Table 1.2. Plasma-assisted CVD processes operate at low pressure and allow the cold-wall setting because the plasma bombards the gas mixture and decompose into active species for deposition at low temperature. Photo CVD is another instrument that works at low temperature and uses the activation energy from ultraviolet or visible photons to achieve the gaseous decomposition. Laser CVD is a device that provides higher activation energy and, furthermore, very accurate control of the local deposition. Other CVD instruments like Metal-Organic CVD (MOCVD) and Chemical Vapor Infiltration (CVI) have specific applications. The epitaxial growths of III/V materials from MOCVD have become very important in the manufacturing of solar cells and light-emitting diodes (LEDs), and the semiconductors with organo-metallic compounds. CVI is the specific instrument for the growth of ceramic materials in a porous body.

### **Different Configurations of the CVD Reactors**

For different operating conditions and applications, several different configurations of the CVD reactors have been developed. Figure 1.4 illustrates some common CVD reactors. Typically, the reactors in Figure 1.4 (a), (b), and (c) are utilized for cold-wall settings and the ones in Figure 1.4 (d), (e), and (f) have higher wall

temperatures of the CVD chambers. The barrel reactor has been greatly used for the huge-amount production of the silicon epitaxial wafers. The vertical reactor with rotating susceptor is often utilized for single-wafer depositions; on the other hand, the one in Figure 1.4 (e) has higher area of uniform deposition and is used for the depositions of multiple wafers. The tubular reactor is usually used to deposit films with polysilicon and dielectric materials. In the later discussion, the modeling and the optimization of the CVD processes focus on the configuration of the vertical impinging reactor with the stationary susceptor in Figure 1.4 (e).

**Table 1.2. Different Types of the CVD Processes.**

<b>Different Types</b>	<b>Abbreviation</b>	<b>Descriptions</b>
Plasma-Enhanced CVD	PECVD	A CVD instrument with plasma enhancement where higher density of reactant species are produced to the substrate due to the high-energy electron impact. Higher activity of the gaseous species allows deposition at comparatively low temperature (450 – 650K). [18, 27]
Metal-Organic CVD	MOCVD	Also known as Organo-Metallic Vapor Phase Epitaxy (OMVPE). An epitaxial growth of materials from the surface chemical reaction of organic or metal-organic compounds and an important process for the manufacturing of solar cells and LEDs. [34-35]
Laser CVD	LCVD	A laser-assisted instrument that locally heat the substrate to activate the CVD reaction with precise control [36].
Photo CVD	PCVD	A photo-assisted deposition technique where UV or visible photon energies are used for gas decomposition. The deposition at very low temperature (300 – 450K) is allowed but having a low deposition rate and poor uniformity. [18, 37]
Chemical Vapor Infiltration	CVI	A variant CVD device that deposits within a porous body and is widely used for the fabrication of ceramic materials [38].
Hot Wire CVD	HWCVD	A special instrument for producing high-temperature gas decomposition but room-temperature deposition on the substrate [39].
Atomic Layer CVD	ALCVD	A technology to produce ultrathin layers of crystalline materials (typically 1 – 50nm) [40].

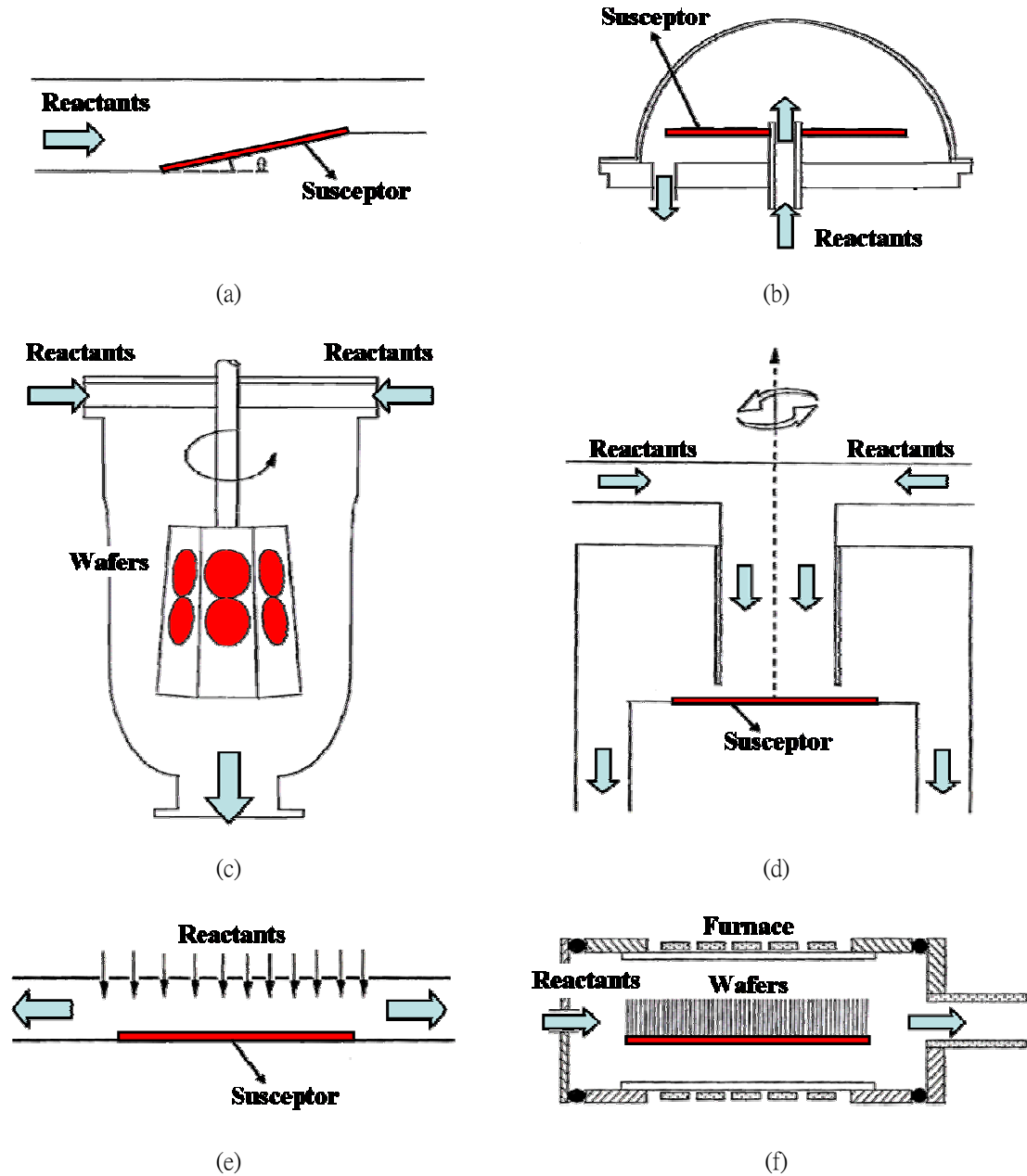


Figure 1.4. Different Configurations of the CVD Reactors (Adapted from [18]).

(a) Horizontal Reactor, (b) Pancake Reactor, (c) Barrel Reactor, (d) Vertical Impinging Reactor with Rotating Susceptor, (e) Vertical Impinging Reactor, and (f) Tubular Reactor.

In the design and optimization of the CVD processes, different design variables should be taken into consideration for different configurations. For example, the horizontal reactor in Figure 1.4 (a) has a tilt angle of the susceptor for uniform deposition

with horizontal gaseous flow of the reactant species. The rotation speeds of the reactors in Figure 1.4 (c) and (d) differ the quality of the deposition. The directions of the reactant flow above the susceptor certainly provide different characteristics of the fluidic mechanics and heat transfer. Among all configurations of the CVD reactors, there are some common variables that dominate the performance of the thin-film deposition, including the concentration of the gaseous reactant in the inlet flow, the velocity of the inlet flow, the temperature of the susceptor, the temperature of the chamber wall, the operating pressure in the CVD chamber, etc. The review about the design of the CVD processes will be given in the next subsection.

### **1.2.3. Design of the CVD Process**

Different designs of the CVD processes have a wide variety of the film thickness, generally ranges from a few nanometers to tens of microns. As described previously, the film formation process is highly dependent on the flow and the heat transfer between the gas and the heated substrate. Therefore, in order to produce thin films with higher deposition rates and quality, the operation conditions must be studied. There are two major aspects to be considered in the design of the CVD processes:

- Experiments or simulations of the CVD processes.
- Modeling of the responses.

Reviews about those aspects are given in the following.

### **Design Variables and Responses of the CVD Processes**

Once the reactant species, the type of the CVD process, and the CVD configuration have been determined for the desired thin-film production on the susceptor, several operating parameters should be chosen to perform the experiments or the simulations of the CVD process. Among those parameters, some of them dominate the control of the deposition performance and are selected to be the design variables. The typical design variables are categorized into two different types, including hardware settings and operating conditions, and listed in Table 1.3. The hardware settings vary the boundary conditions and the mechanical properties of the fluid mechanics and the heat transfer in the CVD processes. On the other hand, the operating conditions are the quantitative variables to control the behavior of the reactant fluid and the performance of the deposition. Besides the hardware and operating design variables, the rest of the parameters remain constant because of either their minor impacts to the deposition or the simplicity of the CVD design. In this research work, the inlet velocity and the susceptor temperature are chosen as the design variables because their quantities can be easily controlled by the designers.

The merit of the deposition performance requires several quantitative responses to judge, where those responses typically have physical meanings and provide numerical measures. Table 1.3 points out several common responses from either the experiments or the simulations of the CVD processes. Among those typical responses, some of them still lack of numerical measures to decisively quantify its degree of intensity. For example, the deposition uniformity itself is a subjective scale of the quality of the CVD production.

*George* [41] utilized a weighted sum of the local slopes of the deposition to quantify its uniformity. *Lin et al.* [42] used some standard statistical measures, including the root mean square and the kurtosis, as the responses of the uniformity factors. More details about the chosen design variables and the significant responses in the proposed research are shown in Chapter 2.

**Table 1.3. Typical Design Variables and Responses in the CVD Designs [18, 28, 43-46].**

Design Variables		Responses
Hardware settings	Susceptor size	Deposition thickness
	Shape of the CVD chamber	Deposition rate
Operating conditions	Angle of the susceptor versus the flow direction	Deposition uniformity
	Orientation of the susceptor versus gravity	Nusselt number
	Buoyancy driven / force driven flow	Temperature distribution of the susceptor
	Diffusivity of susceptor material	Purity of the deposition
	Velocity of the inlet flow	Composition of the deposition
	Susceptor temperature	Adhesion to the substrate
	Operating pressure	Surface morphology
	Rotation speed of the susceptor	Grain structure in the deposition
	Concentration of the reactant species	Distance of flow separation

### Experiments or Simulations of the CVD Processes

The mechanics of the CVD process, in which the flow, the heat transfer, and the chemical reaction are involved, is very complicated. The flow in the CVD process has firstly been visualized by seeding micro-scale titanium dioxide ( $\text{TiO}_2$ ) particles in the reactant gas and illuminating by laser [47-49]. However, the holography observation using the laser provided poor resolution of the lowly concentrated reactants. On the other



hand, numerical simulations provide relatively better understanding of the fluid mechanics and have become very important to study the complex flow in CVD process.

Numerous researchers have been devoted to investigate the flow and heat transfer in CVD reactors [28, 43-46, 50-64]. Some of them focused on the simulations of the horizontal CVD reactors [28, 46, 52, 57, 62], while many other important studies have been conducted to the vertical configurations [43, 51]. Among all the numerical analysis in CVD reactors, three major governing equations are considered – continuity, momentum, and energy conservations governing equations: energy conservation [65]. Generally, parabolic governing equations [52, 55] are utilized to predict the flow pattern in CVD reactors. However, extreme conditions, such as low Reynolds numbers and high density gradients, lead to reverse flow [54] which required elliptic governing equations for better predictions [55, 57].

Simulations of the CVD processes are very complicated because of huge amount of controlling variables [66], complicated analysis of the fluidic dynamics and the kinetics of the chemical reactions, and all the variable properties [44] to be considered. Numerical models with constant properties [50, 67-68] and Boussinesq approximations [67, 69] have been utilized to simplify the complex simulations. *Wang et al.* [64] and *Chiu et al.* [61] demonstrated that the constant-property models are acceptable for most practices but variable-property models give more accurate predictions for extreme operating conditions. The Buoyancy effect has been neglected when the ratio of Grashof number and square of Reynolds number is less than two [70-71]. The geometry of the

reactor is also a factor in the fluid dynamics of the CVD process [43] but it is negligible in a large aspect ratio [61]. The temperature distribution of the susceptor is approximated to be isothermal for some CVD configurations [70].

Thorough comparisons between the experiment and simulation results are provided by *Dimitrios et al.* [43] and *Chiu et al.* [62]. Comprehensive reviews on CVD reactor studies are given by *Mahajan* [18] and *Jensen et al.* [44]. *Kee et al.* [59, 66] demonstrated that model simulations have much greater flexibility and versatility as compared to experimental counterparts. Experimental studies have also been carried out on the flow in channels for CVD applications [44, 46, 62, 72].

### **Optimization of the CVD Processes and Existence of the Design Uncertainties**

Simulation and optimization of CVD systems have been studied by many researchers [41-42, 66, 72-76]. However, design uncertainties can be found everywhere in the CVD process. Even if an optimal design is obtained from the optimization models, the irresistible uncertainties will cause unstable responses of the CVD process. For example, the compositions of the deposition species have errors of 15 % [77]. Several researchers have estimated the randomness of the operating parameters in the CVD process. The rate constant of the chemical reaction may have a wide variance; for example,  $10^{13} - 10^{14} \text{ cm}^3/\text{mol-s}$  [78]. In this research work, the existence of the design uncertainties is considered at the design variables, the inlet velocity and the susceptor temperature of the CVD process.

### **1.3. Research Contributions**

The main contribution of this research includes

- The development of the performance responses in the CVD process.
- The parametric modeling of those responses in terms of the chosen design variables.
- The optimization formulations of the operating operations for the CVD process.
- The realization of the convergence problem in a traditional RBDO algorithm, the TRIA.
- The development of the MRIA to solve optimization problems with normally distributed design uncertainties.
- The development of the MRIA for the non-normally distributed random variables.
- The application of the MRIA on the RBDO problems of the CVD process.

Figure 1.5 schemes the systematic strategy to parametrically model the responses from the experiments or the simulations of the thermal systems and optimize the operating conditions with design uncertainties using the proposed RBDO algorithm.

At the beginning of the productions of any thermal systems, several trials of the experiments or the numerical simulations are necessary to determine the operating conditions and examine the system performances. A RSM model helps the engineers or the designers recognize the behavior of the responses with respect to the design variables. Optimization problems are formulated in terms of the RSM models and are utilized to provide the operating conditions for higher productivity and quality of the productions.

Due to the existence of the design uncertainties, the traditional deterministic optimization formulation is no longer reliable to generate safe designs because it may lead to a design with high risk of system failure. The development of the RBDO algorithm evaluates the probabilities of the system failures and provides a more conservative design which reaches to the optimality as the failure probabilities are subject to some acceptable level. Finally, the productions of the thermal systems are executed based on the optimal design variables. If any design uncertainties are found in the experiments, the simulations, or the mass productions, the information of the uncertainties are fed back to the formulation of the RBDO problems and new optimal conditions can be generated by the proposed strategy.

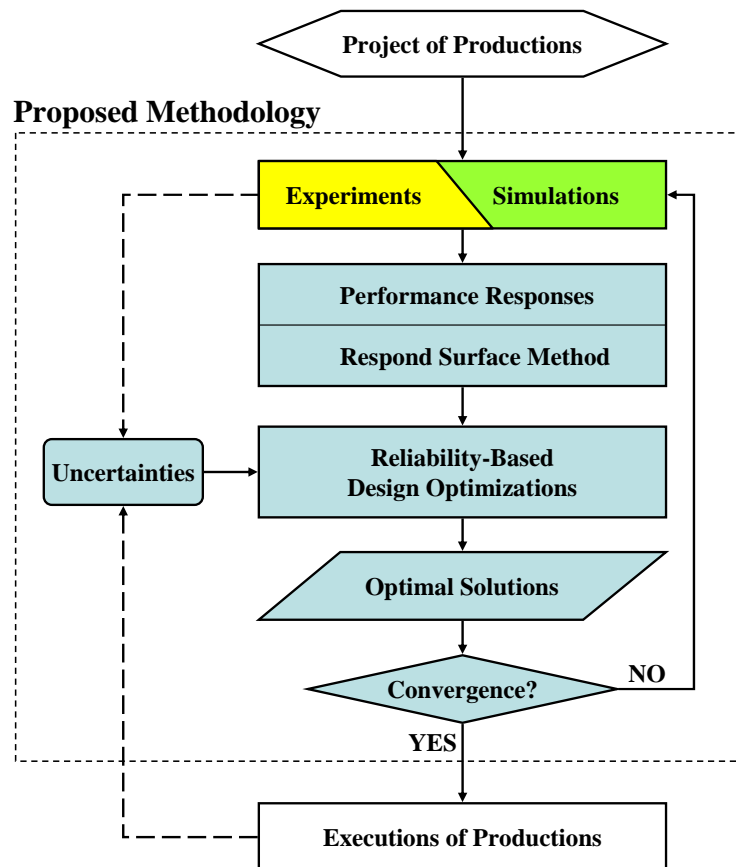


Figure 1.5. Flowchart of the Proposed Research.

### **1.4. Overview of the Dissertation**

In Chapter 2, the description about the simulation of the CVD process is followed by the function formulations of the responses to quantitatively describe the productivity and uniformity of the deposition. A design of the vertical impinging CVD process is defined and simulated by a commercial CFD software, FLUENT. The inlet velocity and the susceptor temperature are chosen to be the design variables. Simulated deposition profiles due to different operating conditions are studied and the four different responses are measured in terms of the design variables, including the Percentage of the Working Area (PWA), the Mean of the Deposition Rate (MDR), the Root Mean Square (RMS), and the Surface Kurtosis (KUR).

In Chapter 3, the responses of the CVD process are parametrically modeled with respect to the design variables. Instead of using the common Response Surface Method (RSM), Polynomial Response Surface (PRS), which has poor approximations on the highly nonlinear responses of the CVD process, the parametric modeling is completed by the Radial Basis Function (RBF). RBF is constructed by nonlinear functions in terms of the distance covariance functions between the sampling data. The approximation using RBF is much accurate and is validated by comparing with large-scale sampling data.

Chapter 4 demonstrates several optimization problems to find better operating conditions for improving the performance of the CVD process. The objective and constraint functions are formulated in terms of the RBF models of the CVD responses. For higher productivities, one of the objective functions is to maximize the PWA while

another one is to maximize the MDR. On the consideration of the uniformity of the deposition, the RMS and the KUR are subject to certain quantitative levels. Both constraints of the deposition uniformity are very significant to the locations of the optimal operating conditions. However, the probabilities of that the optimal solutions violate the performance constraints are very high if the design uncertainties exist.

In Chapter 5, the RBDO technique is introduced to solve the optimization problems with design uncertainties. Replacing the original deterministic constraints, the probabilistic constraints where the probabilities of the system failures are constrained by acceptable levels are formulated. This study focuses on the one of the RBDO algorithms, the RIA. The failure probabilities are evaluated by the Standard Normal Cumulative Distribution Functions in terms of the Hasofer-Lind reliability index. However, the RIA has been reported to have convergence problems. As a result, it may provide incorrect optimal solutions or it may have inefficient optimization processes.

In Chapter 6, the convergence problem in the traditional RIA is revealed and it occurs when the design point is located in the infeasible domain during the iteration process. A modified reliability index is defined to resolve the problem and the evaluations of the failure probabilities using the modified reliability index are correct despite of the locations of the design points. This new method is called the Modified Reliability Index Approach (MRIA). The numerical examples show the MRIA provides the correct optimal solutions with acceptable failure probabilities for the normally distributed random variables. For non-normally distributed random variables, their

standard deviations vary with respect to the design point and an additional updating scheme of the standard deviation is necessary for the MRIA.

In Chapter 7, the proposed RBDO algorithm, the MRIA, is utilized to solve the optimization problems of the CVD process with design uncertainties. The random variables are firstly assumed to be normally distributed and the MRIA provides new optimal solutions to the CVD problems where the failure probabilities are constrained. Secondly, the random variables are considered to be lognormally distributed and their standard deviations are iteratively updated during the optimization process by the MRIA. Numerical examples show the MRIA can find the correct optimal solutions for the RBDO problems of the CVD process for both the normally and non-normally distributed random variables.

In Chapter 8, a conclusion is provided for this study and a future research is proposed for the applications of other thermal systems with various kinds of design uncertainties using the MRIA.

## **Chapter 2.**

### **Simulation and Responses of the CVD Process**

#### ***2.1. Introduction***

This chapter is directed at the simulation of the CVD process and the responses of to represent the productivity and the uniformity of the deposition. The effect of different operating conditions on the deposition rate and the film quality are identified from the numerical simulations performed using a commercial software, FLUENT. Session 2.2 discusses the simulation of the thin-film growth of silicon from the reactant of silane in a vertical impinging CVD reactor. The design operating conditions focus on the velocity of the inlet flow and the temperature of the susceptor. In session 2.3, four responses, including Percentage of the Working Area (PWA), the Mean of the Deposition Rate (MDR), Root Mean Square (RMS), and the Surface Kurtosis (KUR), are defined in terms of the design variables and measured from the simulated deposition profiles. Session 2.5 is the conclusion and the remarks about the simulation and the responses of the CVD process.

#### ***2.2. Simulation of the CVD Process***

The reaction gases are introduced at the top in a vertical impinging reactor. A schematic of the CVD reactor is shown in Figure 2.1. A two dimensional steady laminar flow is assumed. *Chiu* and *Jaluria* [60] described the validity of the two-dimensional steady flow assumptions for a similar system. The flow with a dilute precursor



concentration of silane in hydrogen as the carrier gas deposits silicon onto the susceptor. Silicon deposition follows a one step reaction mechanism, where silane decomposes to silicon and hydrogen. The three species being considered are silane, silicon and hydrogen. Continuity, momentum, energy and species conservation [79] is considered.

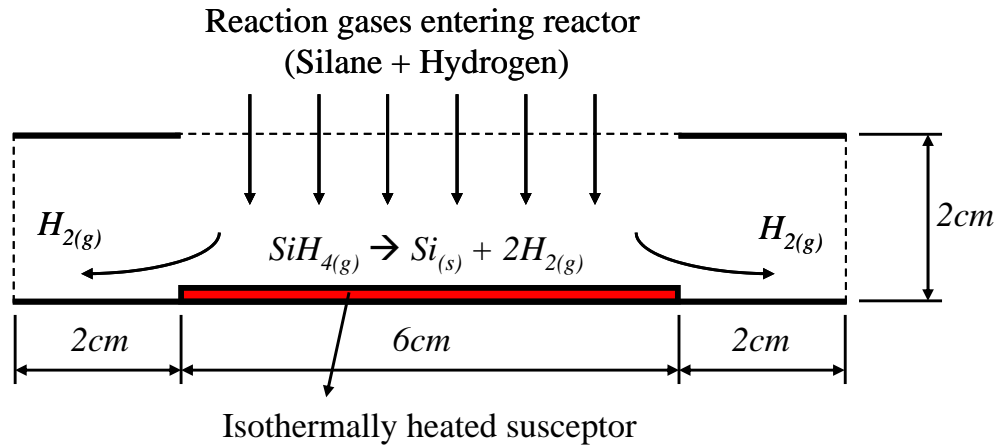


**Figure 2.1. Vertical Impinging CVD Reactor [41].**

Simulations are carried out employing the commercial software FLUENT using the laminar finite-rate model [79]. The laminar finite-rate model computes the chemical source terms using Arrhenius expressions, and ignores the effects of turbulent fluctuations. In Figure 2.1, the dimensions are based on a similar reactor configuration studied by the research group earlier for titanium nitride deposition. Gas phase and wall surface reactions are considered. The surface reaction rate is given by the product of the concentration of the reactant gases at the substrate and the rate constant. An Arrhenius expression is used to calculate the rate constant and is given by  $\kappa = A\tau^\alpha \exp(-E_a/RT)$ , where  $\kappa$  is the rate constant,  $A$  is the pre-exponential factor,  $\tau$  is the temperature,  $E_a$  is

the activation energy,  $\alpha$  is the temperature exponent, and  $R$  is universal gas constant. The values to be used for the quantities are given by the FLUENT database [80], where  $A = 0.334$ ,  $\alpha = 0.5$ , and  $E_a = 1 \times 10^5$ . The material properties can be entered into FLUENT but here they are given by the FLUENT database. FLUENT is used because it can accommodate different geometries and boundary conditions, while there is less flexibility in the validated codes and modifying existing codes is time consuming.

The properties of the materials and the reaction kinetics are loaded from the FLUENT database [80]. The property variations with temperature are taken into account. The power-law discretization scheme [65] is used to solve the equations of the momentum, energy, and species conservations. Coupled algorithm [79] is used to approach the governing equations of continuity, momentum, energy, and species transport simultaneously in the earlier iterations. In the later iterations, the corrections for pressure and velocities are performed by the PISO algorithm [79] in order to achieve more efficient convergence. The boundary conditions are shown in Figure 2.2. Non-slip, impermeable and thermally insulated boundary conditions are applied at the upper and lower surfaces, which are maintained at 300 K, except the susceptor. The isothermally heated susceptor is assumed to be maintained at temperature,  $T$ . The temperature of the reaction gases entering the reactor is 300 K. The ranges of inlet flow velocity,  $V$ , and susceptor temperature,  $T$ , considered are 0.1 m/s – 1 m/s and 400 K – 1500 K [50] respectively. The mass fraction of silane is kept at 0.1 because it ensures sufficient amounts of precursor gas in the mixture [31]. Chiu [75] used a range of susceptor temperature from 900 K – 1323 K but here a larger range is considered. Only half of the

fluid domain is considered in the simulation due to the geometrical symmetry. Quad meshes are utilized in the half domain: 320 nodes in the horizontal direction and 139 nodes in the vertical direction. Node density is chosen such that further increase in node density does not significantly affect the solution. Typical cases require about ten minutes for converging on an Intel® Pentium® M processor 2.0 GHz with 2.0 GHz of RAM.

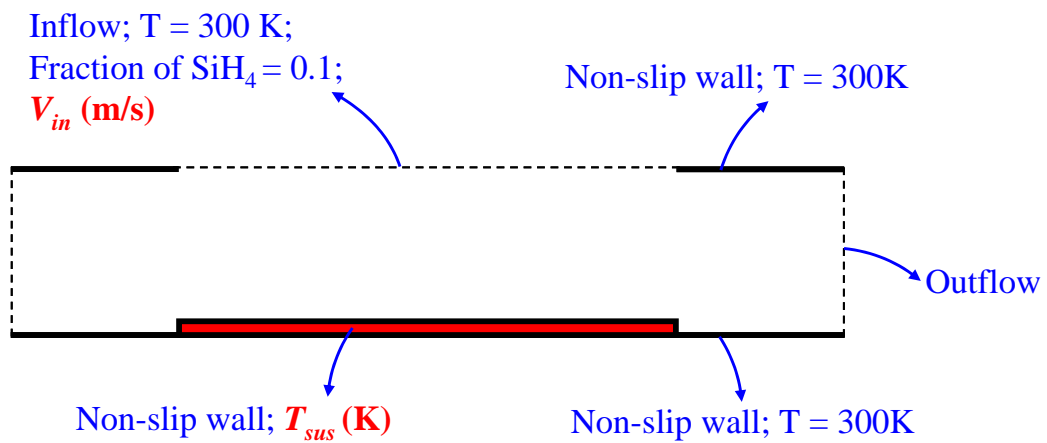


**Figure 2.2. Boundary Conditions of the Simulation for the Vertical CVD Reactor.**

Figure 2.3 illustrates a typical numerical result of the streamlines of the reactant flow in the CVD reactor. The inlet has uniformly distributed velocity,  $V$ , and the stagnation point at the center of the susceptor has zero velocity. Figure 2.4 demonstrates the corresponding temperature distribution of the entire fluid domain where the susceptor is isothermally heated at the temperature of  $T$ . Figure 2.5 shows a scheme of the deposition profile. The red area has poor uniformity of the deposition rate where its local slope of the deposition profile is too oblique; on the other hand, only the green area has acceptable uniformity because its local slope is very close to zero.

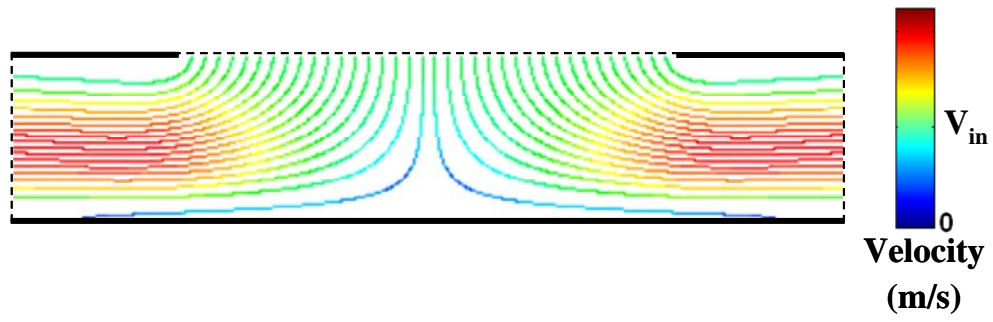


Figure 2.3. A Typical Result of the Streamlines of the Flow.

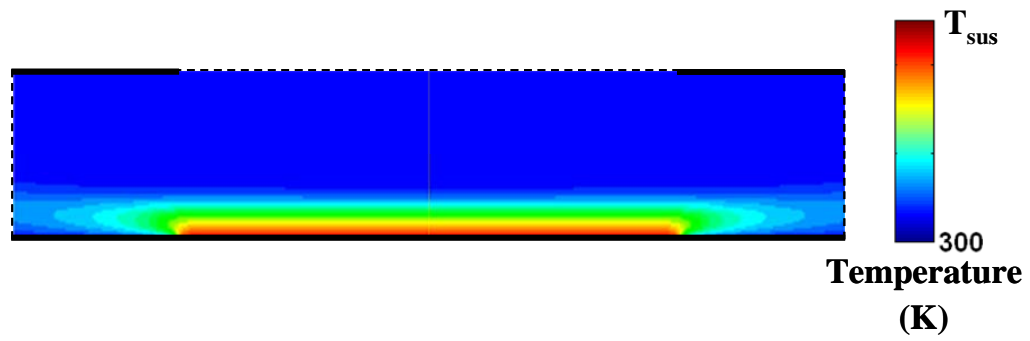


Figure 2.4. A Typical Result of the Temperature Distribution.

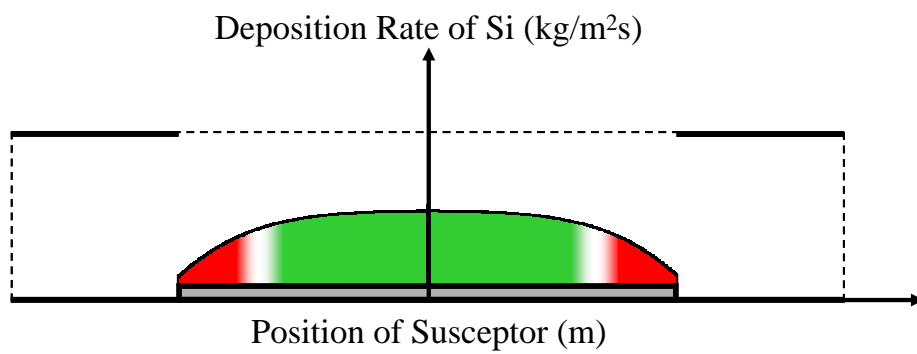


Figure 2.5. Scheme of the Deposition Profile of Silicon.

### 2.3. Simulation Validation

To validate the correctness of the numerical simulations with the developed settings in FLUENT, the deposition rate of the silicon in a horizontal CVD reactor is compared with experimental and numerical results from other researchers [41, 45, 50, 56, 63]. Figure 2.6 illustrates the configuration of the horizontal CVD reactor and its dimensions. The reactant, the silane, is mixed in the hydrogen carrier flow, with the inlet velocity of 0.175 m/s. The partial pressure of the silane is 124.1 Pa under the atmospheric pressure, providing the information of the mass fraction of the silane. The operating temperature is 300 K and the susceptor is isothermally heated at 1323 K. The material properties and the kinetics of the chemical reactions are given from the Ref. [41] otherwise from the FLUENT database. The rest of the settings and the utilized solvers remain the same as the previous discussion.

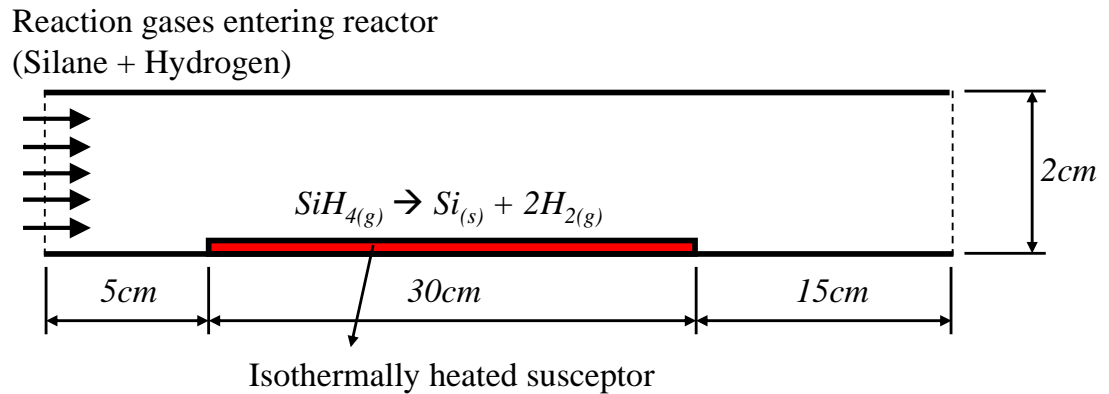
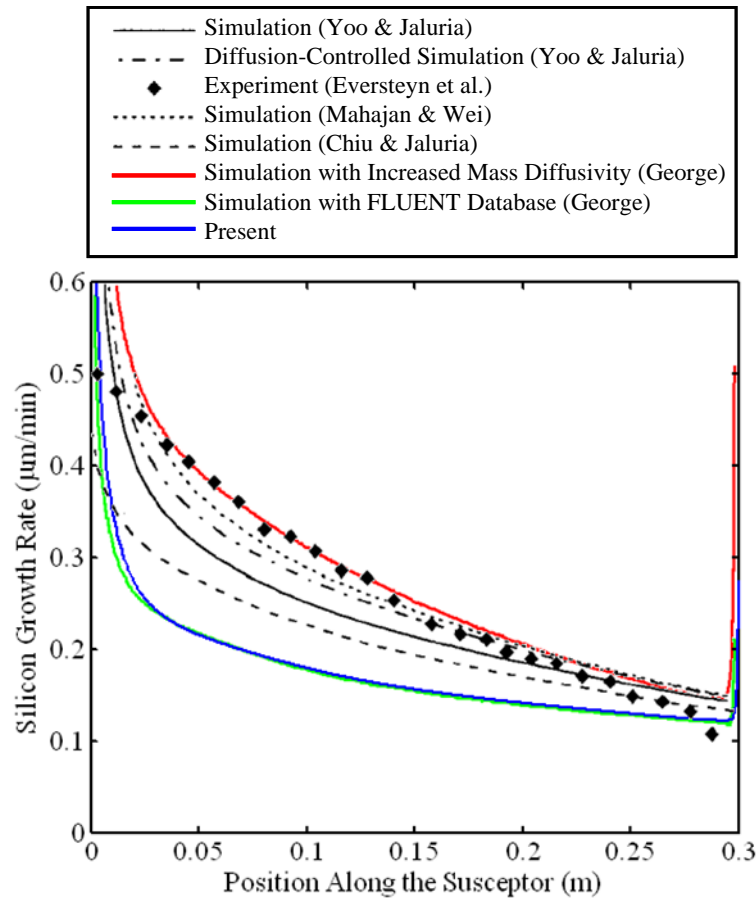


Figure 2.6. Horizontal CVD Reactor [41].

The results from the simulation of a horizontal CVD reactor using FLUENT are compared with the experimental results obtained by Ref. [50] and the numerical results from Refs. [45, 56, 63], shown in Figure 2.7. A detailed comparison between experimental and numerical results has been made and fairly good agreements has been found [75]. The numerical results using the settings described in the previous discussion is almost identical to *George's* simulation results [41] with the mass diffusivity in the FLUENT database, which is given by a polynomial equation of the temperature as follows:

$$D = 7.234 \times 10^{-8} T + 4.569 \times 10^{-10} T^2 - 8.016 \times 10^{-14} T^3 \quad (2.1)$$



**Figure 2.7. Deposition Rate of Silicon in the Horizontal CVD Reactor Compared with Others [41, 45, 50, 56, 63].**

*George* [41] has also shown the numerical results are very close to the experimental results in Ref. [50] if higher mass diffusivity is utilized. *Eversteyn et al.* [50] utilized a power law to describe the mass diffusivity which is given by

$$D = D_0 (T/300)^\gamma \quad (2.2)$$

where  $D_0$  is the pre-exponential factor,  $\gamma$  is the temperature exponent, and the temperature,  $T$ , is normalized by the operating temperature, 300 K. Considering the pre-exponential constant in Ref. [63],  $D_0 = 6.24 \times 10^{-5} \text{ m}^2/\text{s}$ , and varying the temperature exponent from 1.7 to 2.0 as *Eversteyn et al.* [50] suggested, different levels of the mass diffusivity of the silane are obtained and shown in Figure 2.8. With the higher temperature exponent, the corresponding mass diffusivity increases as well as the growth rate of the silicon along susceptor in the horizontal CVD reactor increases, shown in Figure 2.9. In this research work, the mass diffusivity is chosen from the FLUENT database.

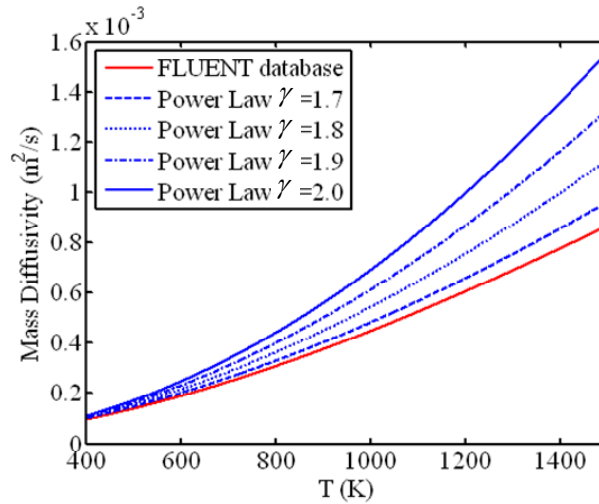


**Figure 2.8. Mass Diffusivity of Silane with Different Temperature Exponent Compared with FLUENT database.**

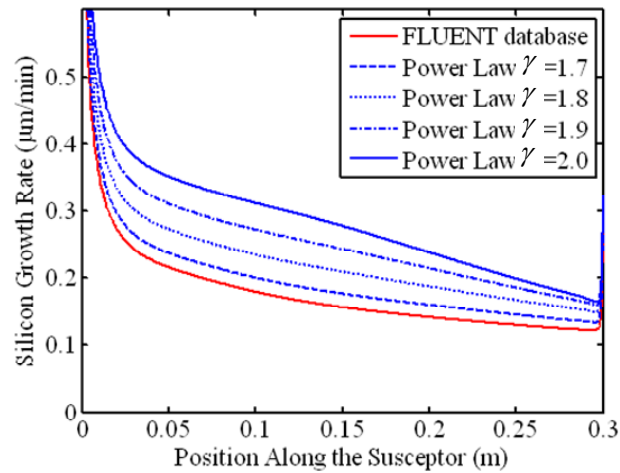


Figure 2.9. Growth Rate of Silicon in the Horizontal CVD Reactor with Different Mass Diffusivity.

## 2.4. Function Formulations of the Responses in CVD Process

To achieve higher deposition rate and better film quality on the susceptor during the CVD process, some quantitative measures are needed to justify the performance of the deposition profile. Three mathematical functions, Mean of Deposition Rate (MDR), Root Mean Square (RMS) and Surface Kurtosis (KUR) are used to measure the deposition rate and film quality. However, because the quality of deposition close to the edge of the susceptor sometimes is not stable due to the significant drop of temperature, one additional function, Percentage of Working Area (PWA), which excludes all unusable areas must be defined first. In this session, the four function formulations will be discussed.

### 2.4.1. Percentage of Working Area (PWA)

To determine the usable region on the susceptor, the Percentage of Working Area (PWA) is defined. First, a set of uniformly distributed sampling nodes across the



deposition profile is selected and the absolute value of the local slope between two consecutive nodes is set as  $|S|$ . If  $|S| \cong 0$ , the deposition profile between these two nodes is considered as uniform. According to a specific application, process engineer can choose an upper bound,  $S_U$ , so that a region with the slope of any two consecutive nodes satisfying  $|S| \leq S_U$  is considered as uniform. The quantity of  $S_U$  is selected as the criterion of local uniformity based on different applications. In the current study,  $S_U = 0.00055$  is chosen. Normally, regions with higher slopes occur around the edges of the susceptor where the deposition rate decreases dramatically due to temperature drop.

However, there are some cases that the areas with higher slopes are not connected. For example, the deposition profile (1) in Figure 2.10 has local non-uniformity at the edge from 0.028 m to 0.03 m and the area from 0.021 m to 0.024 m, highlighted by red curves. Even if the in-between area from 0.024 m to 0.028 m has acceptable slopes, shown by green curves, it is isolated and cannot be utilized to produce micro-structures. When the isolation of working area occurs, the small pieces of isolated working areas must be excluded. Hence, the Percentage of Working Area (PWA) is defined as:

$$\text{PWA} = \frac{\text{EWA}}{\text{Total Area}} \times 100\% \quad (2.3)$$

where EWA denotes the Effective Working Area. The deposition profile (1) has the PWA of 70.59 % while the profile (2) has 87.25 %. More details about the two deposition profiles in Figure 2.10 are shown in the later discussions.

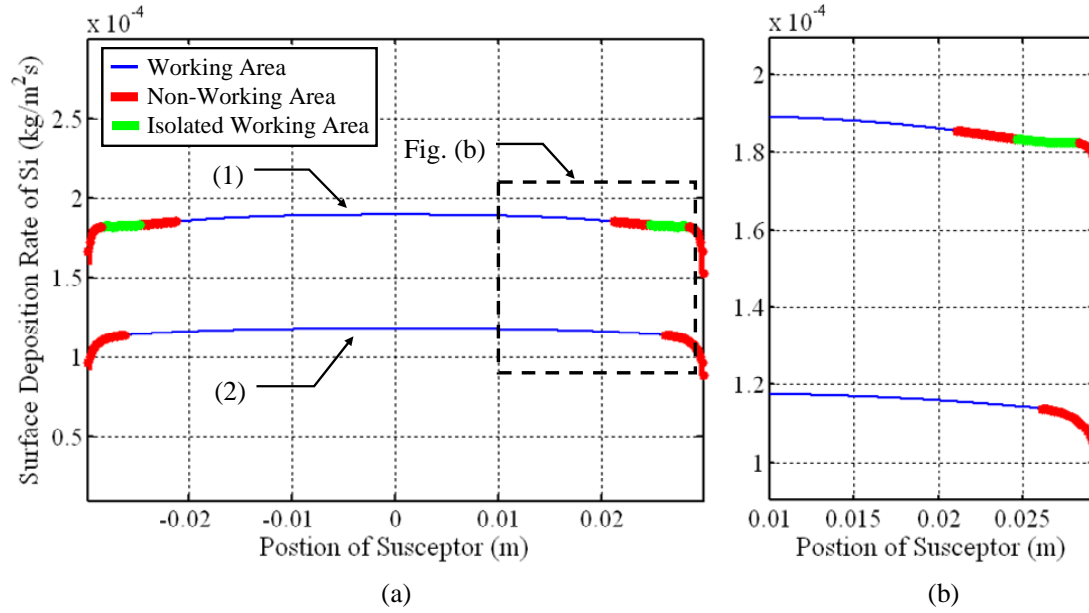


**Figure 2.10. Deposition Profiles with Different PWA.**

**(a) Deposition Profiles of Samples (1) and (2), and (b) Details at the Edges.**

Two remarks should be noticed for the PWA. Firstly, larger PWA represents the thin-film deposition has better uniformity; therefore, one of the possible optimization formulations is to maximize the PWA to increase the quality of the deposition. Secondly, the rest of the responses should be measured within the EWA instead of the entire area of the susceptor because the non-working area will be dumped and only the deposition performance in the working area is of concern.

#### 2.4.2. Mean of Deposition Rate (MDR)

Rate of thin film deposition is one of the key criteria to measure the performance of CVD process. To provide an overall measure of the deposition rate, an averaged local deposition rate is defined as the Mean of Deposition Rate (MDR). However, instead of

studying the deposition rate of the entire susceptor, only the areas within the EWA is considered. The definition of the MDR is very straight forward as:

$$\text{MDR} = \frac{1}{Q} \sum_{i=1}^Q D_i \quad (2.4)$$

where  $Q$  is the number of uniformly distributed sampling nodes within the EWA, and  $D_i$  is the deposition rate at the sampling node. The higher MDR represents better CVD productivity. It is obvious that a larger PWA along with high MDR is very desirable in CVD. However, these two objectives sometimes conflict with each other. In Figure 2.10, the profile (2) has higher PWA than the profile (1); however, the profile (1) has a higher MDR of  $1.884 \times 10^{-4} \text{ kg/m}^2\text{s}$  than the one of  $1.168 \times 10^{-4} \text{ kg/m}^2\text{s}$  in the profile (2). In Chapter 4, these two optimization formulations will be studied and discussed.

### 2.4.3. Root Mean Square (RMS)

Because the PWA only provides a local measure for uniformity, it is essential to determine the global uniformity mathematically which represents the global physical behaviors of the deposition profile within the EWA. Two statistical measures, the Root Mean Square (RMS) and the Surface Kurtosis (KUR), are utilized to quantify the global uniformity.

The Root Mean Square (RMS) is used to measure the magnitude of the varying deposition rate. The definition of RMS of the silicon deposition rate is given by:

$$\text{RMS} = \sqrt{\frac{1}{Q} \sum_{i=1}^Q (D_i - \text{MDR})^2} \quad (2.5)$$

which is the standard derivation of the deposition rate of all sampling nodes within the EWA. A deposition profile with large RMS represents un-even uniformity of the thin-film formation even all regions are considered as workable from the PWA point of view. Therefore, the RMS is an important global indicator for the film quality, which is complementary to the local indicator, PWA. Figure 2.11 demonstrates two different deposition profiles under different operating conditions. They have close PWA at around 93 % and similar KUR at around 1.8; however, the RMS of the profile (3),  $1.713 \times 10^{-6} \text{ kg/m}^2\text{s}$ , is more than double of the one of  $7.810 \times 10^{-7} \text{ kg/m}^2\text{s}$  in the profile (4). Thus, the profile (3) is considered less uniform than the profile (4).

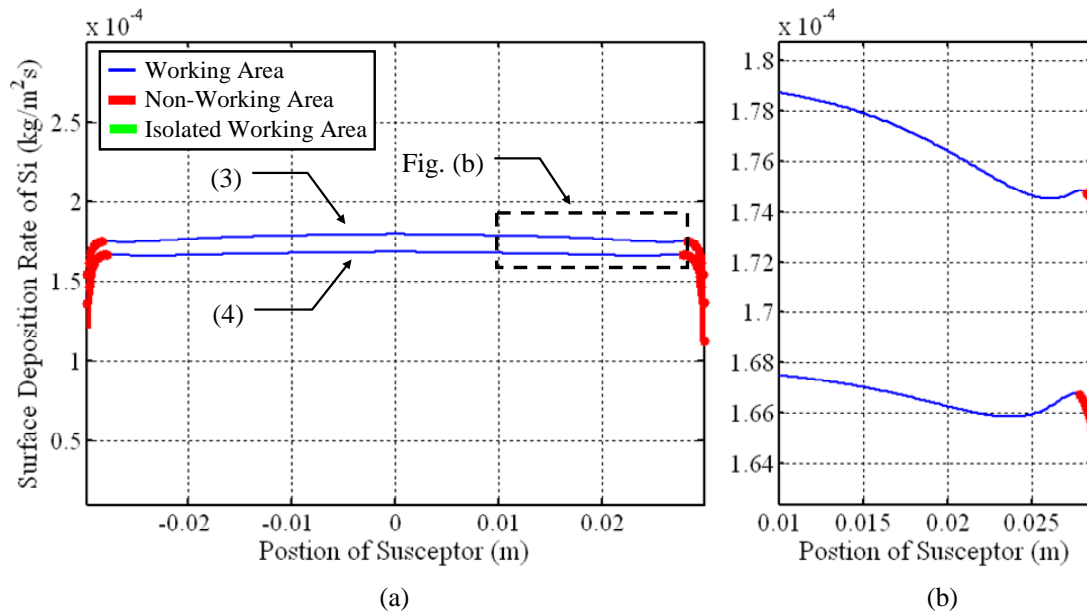


**Figure 2.11. Deposition Profiles with Different RMS.**

**(a) Deposition Profiles of Samples (3) and (4), and (b) Details at the Edges.**

#### 2.4.4. Surface Kurtosis (KUR)

The Surface Kurtosis (KUR) is a statistical quantitative measurement that implies the existences of the sharper peaks in the deposition profile which cannot be recognized by the RMS. The measure of KUR of silicon deposition rate is given by

$$KUR = \frac{1}{Q(RMS)^4} \sum_{i=1}^Q (D_i - MDR)^4 \quad (2.6)$$

where the terms of MDR and the RMS are defined in the Eqs. (2.4) and (2.5) respectively. The KUR represents the “peakedness” of the deposition profile, or the variance due to infrequent extreme deviations [81]. A larger KUR represents peakier profile of the silicon deposition and this acute shape of the profile leads to non-uniformity within the EWA. Figure 2.12 illustrates the profile (5) is lessly peakier than the profile (6); furthermore, the profile (5) has a lower KUR, 1.686, than the one of the profile (6), 4.550.

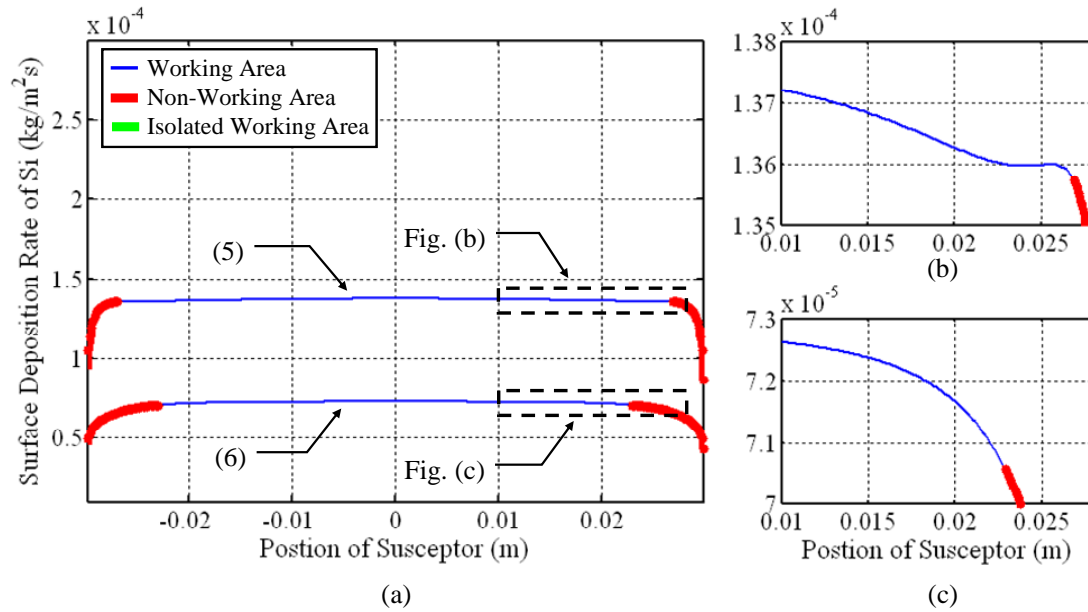


**Figure 2.12. Deposition Profiles with Different KUR.**

(a) Deposition Profiles of Samples (5) and (6), (b) Details at the Edge of Sample (5), and (c) Details at the Edge of Sample (6).

The detailed information about the six examples of the deposition profiles are listed in Table 2.1. Comparing the samples (1) and (2), the PWA is found sensitive to the inlet velocity and has higher working area at lower velocity at 0.25 m/s. However, in the contrast of samples (4) and (5), higher velocity, 0.95 m/s, has larger working area. This implies the responses are highly nonlinear with respect to the design variables,  $V$  and  $T$ . A nonlinear modeling tool is needed.

**Table 2.1. Conditions and Uniformity Factors of Samples (1) to (6).**

Sample #	V (m/s)	T (K)	PWA (%)	MDR (kg/m <sup>2</sup> s)	RMS (kg/m <sup>2</sup> s)	KUR	Figure
1	0.7	650	70.59	1.884E-4	1.229E-6	2.687	Figure2.10
2	0.25	650	87.25	1.168E-4	1.201E-6	2.653	Figure2.10
3	0.75	850	94.12	1.775E-4	1.713E-6	1.812	Figure2.11
4	0.95	1500	92.65	1.671E-4	7.810E-7	1.786	Figure2.11
5	0.6	1500	89.71	1.369E-4	6.214E-7	1.686	Figure2.12
6	0.1	1000	76.47	7.234E-5	5.395E-7	4.550	Figure2.12

## **2.5. Conclusion and Remarks**

The percentage of the EWA in the susceptor has been defined to quantify the production yield of the CVD process. The MDR is measured within the EWA to represent the productivity, while the RMS and the KUR are utilized as the indicators of the uniformity inside the EWA. Several samples of the CVD simulations under different operating conditions have been utilized to show the importance of four responses in the quantifications of the productivity and the uniformity of the CVD process.

Both RMS and KUR are global measures for the quality of deposition uniformity whereas the PWA and MDR are direct local measures. These four functions are greatly influenced by the inlet velocity and the susceptor temperature. However, the true forms of these functions are not available. Therefore, we will establish response surface models of these functions with respect to the design variables in Chapter 3. Once the models are established and validated, we will use the PWA and the MDR as the objective functions and the RMS and the KUR as constraints to study the optimal operation conditions in Chapter 4.

Besides the application of the silicon deposition, the proposed responses are also very useful in other thermal systems regarding the thin-film growth with desired uniformity. Firstly, the range of the working area should be considered carefully based on the allowable local slope otherwise the specific needs in different designs of the thermal systems. The statistical moments and the quantitative performance measures should be studied within the working area because the productions outside the EWA have been excluded from the consideration. Other useful statistical measures include the surface skewness and other higher-order statistical moments. The skewness is not considered in the current research work because the configuration of the vertical CVD reactor is symmetric about the centerline of the inlet flow and the skewness is always zero.

## **Chapter 3.**

### **Parametric Modeling of the CVD Process**

#### ***3.1. Introduction***

The best way to represent the behavior of the responses in the CVD processes and model them in terms of numerical functions with respect to the design variables is to use the technique of curve fitting, also known as metamodeling or Response Surface Method (RSM). RSM provides a parametric equation in terms of the design variables and some coefficients to be determined by substituting the experiment / simulation data into the parametric model. Instead of using the common RSM tool, Polynomial Response Surface (PRS), the Radial Basis Function (RBF) is used to model the deposition rate and the uniformity of the deposition profile. These obtained parametric models of the four responses will be validated before being utilized to formulate the optimization problems of CVD process.

#### ***3.2. Review of Parametric Modeling Techniques***

The RSM can be divided into two different types [1]:

- Exact fitting.
- Best fitting.



The exact fitting is the technique that generates a smooth curve that passes through all the data points. It typically is a function with  $M$  parameters to be determined by the known information from  $M$  data points. Therefore, it is very accurate and useful for small amount of data. On the other hand, the best fitting does not necessarily pass through any of the data points but provides a best prediction of the behavior of the responses. It is very useful when the amount of data points is very large (i.e. There are only  $K$  parameters to be determined for  $M$  sampling points while  $K < M$  .) or the obtained responses are not accurate enough. Several methods have been developed to achieve either exact or best fitting with single variable, two variables, or multiple variables. Table 3.1 lists different kinds the RSM methods and their characteristics.

**Table 3.1. Different RSM Methods [1, 82-84].**

Methods	Available Dimension	Exact Fitting	Best Fitting
Polynomial fitting	1D, 2D, and multiple variables	○	○
Kriging	1D, 2D, and multiple variables	○	○
Radial basis function	1D, 2D, and multiple variables	○	○
Thin plate spline	1D, 2D, and multiple variables	○	○
Hermite curve / surface	Curve for 1D; surface for 2D	○	×
Bezier curve / surface	Curve for 1D; surface for 2D	×	○
B-spline curve / surface	Curve for 1D; surface for 2D	×	○

### 3.2.1. Polynomial Response Surface (PRS)

The polynomial fitting, often called Polynomial Response Surface (PRS), is the most common and simple technique to interpolate or extrapolate the obtained responses with  $M$  sampling points. For small-scale models, a regression formulation is given as follows:

$$F(\mathbf{x}) \cong \mathbf{w} \cdot \mathbf{B}(\mathbf{x}) \quad (3.1)$$

where  $\mathbf{w}$  is a vector of the  $K$  regression coefficients to be determined and it can be written in Einstein's notation:  $\mathbf{w} = w_t \mathbf{e}_t = [w_1 \quad w_2 \quad \cdots \quad w_K]^T$  and  $t = 1, 2, \dots, K$ . Another vector,  $\mathbf{B}(\mathbf{x})$ , is a linear combination of the modeling monomials. The Eq. (3.1) is used for exact fitting when the number of the parameters,  $K$ , equal to the number of the sampling points,  $M$ ; otherwise, it provides predictions with best fitting as  $K < M$ . Table 3.2 demonstrates several typical design of  $\mathbf{B}(\mathbf{x})$  for different  $K$ .

**Table 3.2. Typical Coefficients for Polynomial Response Surface.**

Different PRS	$K$	$\mathbf{B}(\mathbf{x})$
Linear regression	2	$[1 \quad x_1]^T$
Planar regression	3	$[1 \quad x_1 \quad x_2]^T$
Coupling 2-D fitting	4	$[1 \quad x_1 \quad x_2 \quad x_1 x_2]^T$
Independent 2-D quadratic fitting	5	$[1 \quad x_1 \quad x_2 \quad x_1^2 \quad x_2^2]^T$
Coupling 2-D quadratic fitting	6	$[1 \quad x_1 \quad x_2 \quad x_1^2 \quad x_2^2 \quad x_1 x_2]^T$

For exact fitting, the coefficients,  $\mathbf{w}$ , can be obtained by the following equation:

$$\mathbf{w} = \mathbf{A}^{-1}(\mathbf{x}^S) \cdot \mathbf{F}^S(\mathbf{x}^S) \quad (3.2)$$

where  $\mathbf{F}^S(\mathbf{x}^S)$  is a  $K \times 1$  vector of the responses in terms of the  $K$  sampling points and  $\mathbf{A}(\mathbf{x}^S)$  is a  $K \times K$  matrix whose  $s^{th}$  row is  $\mathbf{B}^T(\mathbf{x}_s^S)$ . For example, when  $K = M = 6$ , the coefficients of  $\mathbf{w}$  can be obtained by the following equation in terms of six distinct 2-D sampling points:

$$\mathbf{w} = \begin{bmatrix} 1 & x_{1,1}^S & x_{2,1}^S & (x_{1,1}^S)^2 & (x_{2,1}^S)^2 & x_{1,1}^S x_{2,1}^S \\ 1 & x_{1,2}^S & x_{2,2}^S & (x_{1,2}^S)^2 & (x_{2,2}^S)^2 & x_{1,2}^S x_{2,2}^S \\ & & & \vdots & & \\ 1 & x_{1,6}^S & x_{2,6}^S & (x_{1,6}^S)^2 & (x_{2,6}^S)^2 & x_{1,6}^S x_{2,6}^S \end{bmatrix}^{-1} \cdot \begin{bmatrix} F_1^S(\mathbf{x}_1^S) \\ F_2^S(\mathbf{x}_2^S) \\ \vdots \\ F_6^S(\mathbf{x}_6^S) \end{bmatrix} \quad (3.3)$$

For best fitting,  $\mathbf{F}^S(\mathbf{x}^S)$  is a  $M \times 1$  vector and  $\mathbf{A}(\mathbf{x}^S)$  is a  $M \times K$  matrix as  $K < M$ ; therefore, Eq. (3.2) is no longer valid because  $\mathbf{A}^{-1}(\mathbf{x}^S)$  only exists for  $K = M$ . In this case, the coefficients of  $\mathbf{w}$  need to be obtained by Least Square Approximation [85], which is given by:

$$\mathbf{w} = [\mathbf{A}^T(\mathbf{x}^S) \cdot \mathbf{A}(\mathbf{x}^S)]^{-1} \cdot \mathbf{A}^T(\mathbf{x}^S) \cdot \mathbf{F}^S(\mathbf{x}^S) \quad (3.4)$$

### 3.2.2. Kriging

Kriging is a general method to predict the responses from the experiment or simulation data with minimum error variance estimation [86]. It is constructed by an inner product of a vector of coefficients,  $\mathbf{w}$ , and a covariance vector,  $\mathbf{C}_x(\mathbf{x}, \mathbf{x}^S)$ , shown as follows:

$$F(\mathbf{x}) \cong \mathbf{w} \cdot \mathbf{C}_x(\mathbf{x}, \mathbf{x}^S) \quad (3.5)$$

where the covariance vector contains  $M \times 1$  components of the covariance functions and is given by

$$\mathbf{C}_x(\mathbf{x}, \mathbf{x}^S) = \sum_{s=1}^M C_{x,s}(\mathbf{x}, \mathbf{x}_s^S) \mathbf{e}_s = \sum_{s=1}^M \text{Cov}(\mathbf{x}, \mathbf{x}_s^S) \mathbf{e}_s \quad (3.6)$$

and  $\mathbf{e}_s$  is the  $s^{\text{th}}$  normal basis. Since the responses from the  $M$  sampling points provide the following equation:

$$\begin{aligned} \mathbf{F}^S(\mathbf{x}^S) &= \begin{bmatrix} F_1^S(\mathbf{x}_1^S) & F_2^S(\mathbf{x}_2^S) & \cdots & F_M^S(\mathbf{x}_M^S) \end{bmatrix}^T \\ &= \begin{bmatrix} \mathbf{C}_x^T(\mathbf{x}_1^S, \mathbf{x}^S) & \mathbf{C}_x^T(\mathbf{x}_2^S, \mathbf{x}^S) & \cdots & \mathbf{C}_x^T(\mathbf{x}_M^S, \mathbf{x}^S) \end{bmatrix}^T \cdot \mathbf{w} \\ &= \begin{bmatrix} \text{Cov}(\mathbf{x}_1^S, \mathbf{x}_1^S) & \text{Cov}(\mathbf{x}_1^S, \mathbf{x}_2^S) & \cdots & \text{Cov}(\mathbf{x}_1^S, \mathbf{x}_M^S) \\ \text{Cov}(\mathbf{x}_2^S, \mathbf{x}_1^S) & \text{Cov}(\mathbf{x}_2^S, \mathbf{x}_2^S) & \cdots & \text{Cov}(\mathbf{x}_2^S, \mathbf{x}_M^S) \\ \vdots & \vdots & \ddots & \vdots \\ \text{Cov}(\mathbf{x}_M^S, \mathbf{x}_1^S) & \text{Cov}(\mathbf{x}_M^S, \mathbf{x}_2^S) & \cdots & \text{Cov}(\mathbf{x}_M^S, \mathbf{x}_M^S) \end{bmatrix} \cdot \mathbf{w} \\ &= \sum_{r=1}^M \sum_{s=1}^M \text{Cov}(\mathbf{x}_r^S, \mathbf{x}_s^S) \mathbf{e}_r \mathbf{e}_s \cdot \mathbf{w} = \mathbf{C}(\mathbf{x}^S) \cdot \mathbf{w} \end{aligned} \quad (3.7)$$

the coefficients of  $\mathbf{w}$  can be obtained by

$$\mathbf{w} = \mathbf{C}^{-1}(\mathbf{x}^S) \cdot \mathbf{F}^S(\mathbf{x}^S) \quad (3.8)$$

where  $\mathbf{C}(\mathbf{x}^S)$  is a  $M \times M$  symmetric matrix with zero diagonal terms and non-zero off-diagonal terms of covariance functions,  $\text{Cov}(\mathbf{x}_r^S, \mathbf{x}_s^S)$ . This kind of Kriging technique is utilized for exact fitting. On the other hand, a linear combination of the polynomial fitting function in Eq. (3.1) and the Kriging function in Eq. (3.5) makes best fitting possible for Kriging [87]. The polynomial term provides the global shape of the response surface, while the Kriging term provides local predictions of the responses.

Sequentially, the Radial Basis Function (RBF) [88] is a special kind of Kriging, where the covariance function, also known as the basis function, is evaluated by the Euclidean distance between two corresponding vectors; namely,

$$Cov(\mathbf{x}_r^S, \mathbf{x}_s^S) = \|\mathbf{x}_r^S, \mathbf{x}_s^S\| \quad (3.9)$$

Many other kinds of covariance functions have been utilized for the predictions of the response surfaces and they are listed in Table 3.3. Besides those common covariance functions utilized for different applications by different researchers, other available covariance functions are constructed in a class of polynomial functions in terms of the basis function,  $\|\mathbf{x}_r^S, \mathbf{x}_s^S\|$ , shown in Ref. [89]

### 3.2.3. Geometric Modeling Curves and Surfaces

There are several famous geometric modeling methods that can be utilized for the purpose of RSM. Those include Hermite, Bezier, and B-Spline curves for single-variable RSM and Hermite, Bezier, and B-Spline surfaces for two-variable RSM [84]. A Hermite cubic curve contain multiple continuously connected cubic curves which are parameterized by polynomial functions in terms of four sampling points. The parametric equation is a single-variable polynomial fitting function in Eq. (3.1) with  $\mathbf{B}(\mathbf{x}) = [1 \quad x_1 \quad x_1^2 \quad x_1^3]^T$ . The advantage of using a known parametric function like Hermite curve is that the coefficients,  $\mathbf{w}$ , are given already and no further calculation is needed for the determination of  $\mathbf{w}$ . However, it is generally used for exact fitting. Bezier and B-spline curves are utilized for best fitting of the responses with different set of coefficients,  $\mathbf{w}$ . More details are included in Ref. [84].

**Table 3.3. Common Covariance Functions for Different Kriging Techniques.**

Different Kriging Techniques	$Cov(\mathbf{x}_r^S, \mathbf{x}_s^S)$	References
Gaussian covariance function	$(\sigma^S)^2 \sum_h \exp\left[-\theta_h \ \mathbf{x}_{h,r}^S, \mathbf{x}_{h,s}^S\ ^2\right]^*$	[83, 87]
Exponential covariance function	$(\sigma^S)^2 \sum_h \exp\left[-\theta_h \ \mathbf{x}_{h,r}^S, \mathbf{x}_{h,s}^S\ \right]$	[83]
Product-form covariance function	$(\sigma^S)^2 \prod_h \exp\left[-\theta_h \ \mathbf{x}_{h,r}^S, \mathbf{x}_{h,s}^S\ \right]^\dagger$	[83, 90]
Radial basis function	$\ \mathbf{x}_r^S, \mathbf{x}_s^S\ $	[88]
Pseudo-cubic spline	$\ \mathbf{x}_r^S, \mathbf{x}_s^S\ ^3$	[91]
Weighted distance function	$\sum_h \theta_h \ \mathbf{x}_{h,r}^S, \mathbf{x}_{h,s}^S\ ^{\gamma_h}^\ddagger$	[82, 92]
Thin plate spline	$\ \mathbf{x}_r^S, \mathbf{x}_s^S\ ^2 \log \ \mathbf{x}_r^S, \mathbf{x}_s^S\ $	[86]

In the later discussion, the parametric modeling of the responses in the CVD processes focuses on the exact fitting technique using the Radial Basis Function using the Eq. (3.5) with the covariance function in Eq. (3.9). Those parametric models will be used to formulate optimization problems for improving the performance of the CVD processes.

---

\*  $\sigma^S$  stands for the known standard deviation of the responses and  $\theta_h$  is the unknown correlation parameter to be determined by maximizing the likelihood estimates.

†  $h$  denotes the index for the important sampling points and there exists more than one important sampling points.

‡  $\gamma_h$  controls the smoothness of the distance function.

### 3.3. Radial Basis Function (RBF)

The simplest approach to creating a RSM model is to apply PRS. However, the approximation of PRS may not be very accurate if the response is highly nonlinear. Therefore, the RBF is used to construct the response surface models of the four functions described in the previous section. The resulting models are validated with a 437-point uniformly distributed sampling model over the design domain. For comparison purpose, models from the simple PRS are also listed.

#### 3.3.1. Formulation of the RBF

Using Eq. (3.5) with the covariance function in Eq. (3.9), the RBF approximates any function,  $F$ , as a weighted summation of covariance functions:

$$F \cong \sum_{s=1}^M w_s \text{Cov}(\mathbf{x}, \mathbf{x}_s^s) \quad (3.10)$$

where  $w_s$  is the weighting factor to be determined. Two CVD operation parameters are studied, inlet velocity,  $V$  and susceptor temperature,  $T$ . Therefore, any of the four functions described in the previous section can be approximated using the RBF in the design domain which contains  $M$  sampling points,  $\mathbf{x}_s^s = [V_s^s \quad T_s^s]^T$  for  $s = 1, 2, \dots, M$ . The utilized covariance function is the Euclidean distance between some point,  $\mathbf{x} = [V \quad T]^T$ , and the  $s^{th}$  sampling point,  $\mathbf{x}_s^s$ , and can be expressed as:

$$\text{Cov}(\mathbf{x}, \mathbf{x}_s^s) = \sqrt{\left(\frac{V - V_s^s}{V_m}\right)^2 + \left(\frac{T - T_s^s}{T_m}\right)^2} \quad (3.11)$$

where  $V$  varies from 0.1 to 1 m/s and  $T$  varies from 400 to 1500 K. The velocity difference,  $(V - V_s^s)$ , is normalized by the maximum  $V$ ,  $V_m = 1.0$  m/s; similarly,  $T_m = 1500$  K. Since the responses at all  $\mathbf{x}_s^s$  satisfy the Eq. (3.10), the values of  $\mathbf{w} = [w_1 \ w_2 \ \cdots \ w_M]^T$  can be obtained by the Eq. (3.8) where  $\mathbf{F}^s(\mathbf{x}^s) = [F(V_1^s, T_1^s) \ F(V_2^s, T_2^s) \ \cdots \ F(V_M^s, T_M^s)]^T$  includes the function values at the sampling points, and

$$\mathbf{C}(\mathbf{x}^s) = \begin{bmatrix} 0 & \text{Cov}(\mathbf{x}_1^s, \mathbf{x}_2^s) & \cdots & \text{Cov}(\mathbf{x}_1^s, \mathbf{x}_M^s) \\ \text{Cov}(\mathbf{x}_2^s, \mathbf{x}_1^s) & 0 & \cdots & \text{Cov}(\mathbf{x}_2^s, \mathbf{x}_M^s) \\ \vdots & \vdots & \ddots & \vdots \\ \text{Cov}(\mathbf{x}_M^s, \mathbf{x}_1^s) & \text{Cov}(\mathbf{x}_M^s, \mathbf{x}_2^s) & \cdots & 0 \end{bmatrix}$$

is a  $M \times M$  symmetric matrix containing the values of Euclidean distances between given sampling points. The RBF has no approximation error at all sampling points and is expected to provide better approximations of the responses with non-linear behaviors than the simple PRS. In the next section, functions modeled by the RBF will be validated by a 437-point sampling model and compared with the simple PRS approximation.

### 3.3.2. Model Validation

In this session, the responses at different sampling data sets are compared and validated. Three different sample sets are used: 9-point design, 13-point design, and 25-point design, as shown in Table 3.4. Figure 3.1 illustrates the difference between these three different kinds of sampling designs. In order to validate and compare the quality of the approximated models, the resulting models using the RBF of four functions



discussed in the previous section are compared with the responses generated from 437 samplings and the responses from 25 point PRS. The PRS utilized is given by

$$F(V, T) = w_1 + w_2V + w_3T + w_4V^2 + w_5VT + w_6T^2 \quad (3.12)$$

where the coefficients of  $w$  are determined by Least Square Approximation from the 25 samplings, using the Eq. (3.4).

**Table 3.4. Sampling Data Sets: 9 Points, 13 Points, and 25 Points.**

Point	V (m/s)	T (m/s)	Point	V (m/s)	T (m/s)
1	0.1	400	14	0.1	650
2	0.1	950	15	0.1	1250
3	0.1	1500	16	0.3	400
4	0.55	400	17	0.3	950
5	0.55	950	18	0.3	1500
6	0.55	1500	19	0.55	650
7	1.0	400	20	0.55	1250
8	1.0	950	21	0.8	400
9	1.0	1500	22	0.8	950
10	0.3	650	23	0.8	1500
11	0.3	1250	24	1.0	650
12	0.8	650	25	1.0	1250
13	0.8	1250			

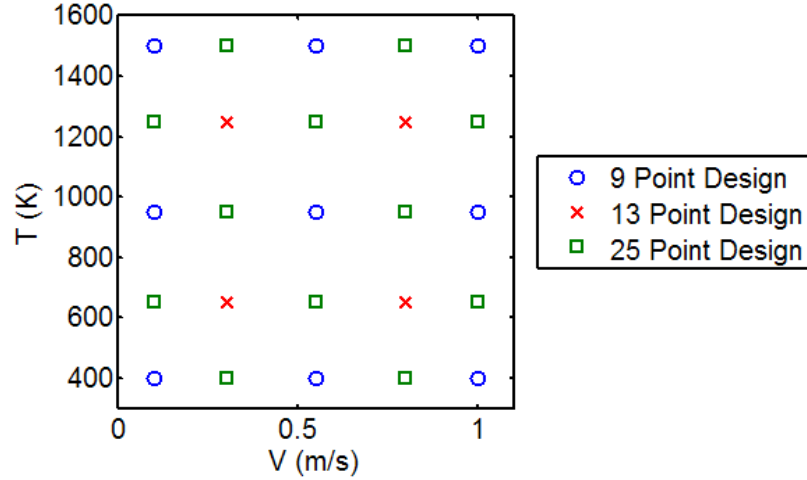


**Figure 3.1. Sampling Data Sets.**

The responses of the PWA are shown in Figure 3.2. Three responses from RBF with 9-point samplings, 13-point samplings and 25-point sampling are listed in the sub-figures (a), (b) and (c), respectively. A 437-point sampling is shown in sub-figure (d) as the baseline for comparison. The comparison is performed in terms of an error function,  $err$ , which is defined as

$$err = \sqrt{\frac{1}{437} \sum_{\eta=1}^{437} (F_{\eta} - G_{\eta})^2} \quad (3.13)$$

where  $F_{\eta}$  and  $G_{\eta}$  denote the  $\eta^{th}$  function values of the response surface model and the simulation respectively. The function values of  $err$  of the 9-point RBF, the 13-point RBF and the 25-point RBF are 7.303 %, 5.486 % and 3.794 %, which implies more sampling points provide better accuracy with RBF. For simplicity, the following sessions will use the 25-point RBF. Due to the occurrence of the isolated working areas at high inlet velocity and low susceptor temperature, a sudden drop of PWA is found around that region. This sudden decrease of the PWA causes non-smooth behaviors during the transition. Beyond the region with isolated working areas, the highest PWA is illustrated

by the dark red region at high inlet velocity and intermediate susceptor temperature in the sub-figure (d). The non-smooth behavior and the quantitative distribution can be captured using the RBF whereas the response from a 25-point PRS, as shown sub-figure (e), fails to recognize it. The error measurement of a 25-point PRS is 5.259 %, which is apparently higher than that of the RBF.

The approximated models of MDR from the RBF, a 437-point response, and PRS are shown in Figure 3.3. Unlike the models of PWA, the MDR behavior is very smooth. The error measurements of the RBF and the PRS are both small  $-2.046 \times 10^{-6}$  kg/m<sup>2</sup>s and  $3.479 \times 10^{-6}$  kg/m<sup>2</sup>s respectively. This is because the MDR is an averaged value in the EWA. Any non-linear behavior is blended into the entire function. The maximum MDR are all located at the same region as shown in the sub-figures (a), (b), and (c). All models of MDR are in very good agreement. Although PRS can model well-behaved function, it lacks the capability of approximating non-smooth behaviors, such as the PWA. Therefore, only the 25-point RBF will be used in the following discussion.

The 25-point parametric model and the 437-point sampling of the responses of RMS are shown in Figure 3.4. Some non-linear behaviors are found at the region of high velocity and low temperature due to the occurrence of the isolated working areas. The infrequent topological change of the RMS, shown in the sub-figure (b), can hardly be handled when making the response surface approximations. Similar to the comparison of the 25-point RBF and 25-point PRS in the Figure 3.2 (c) and (e), the RBF with 25-point

samplings can capture this non-smoothness but not from the PRS with the same 25-point samplings.

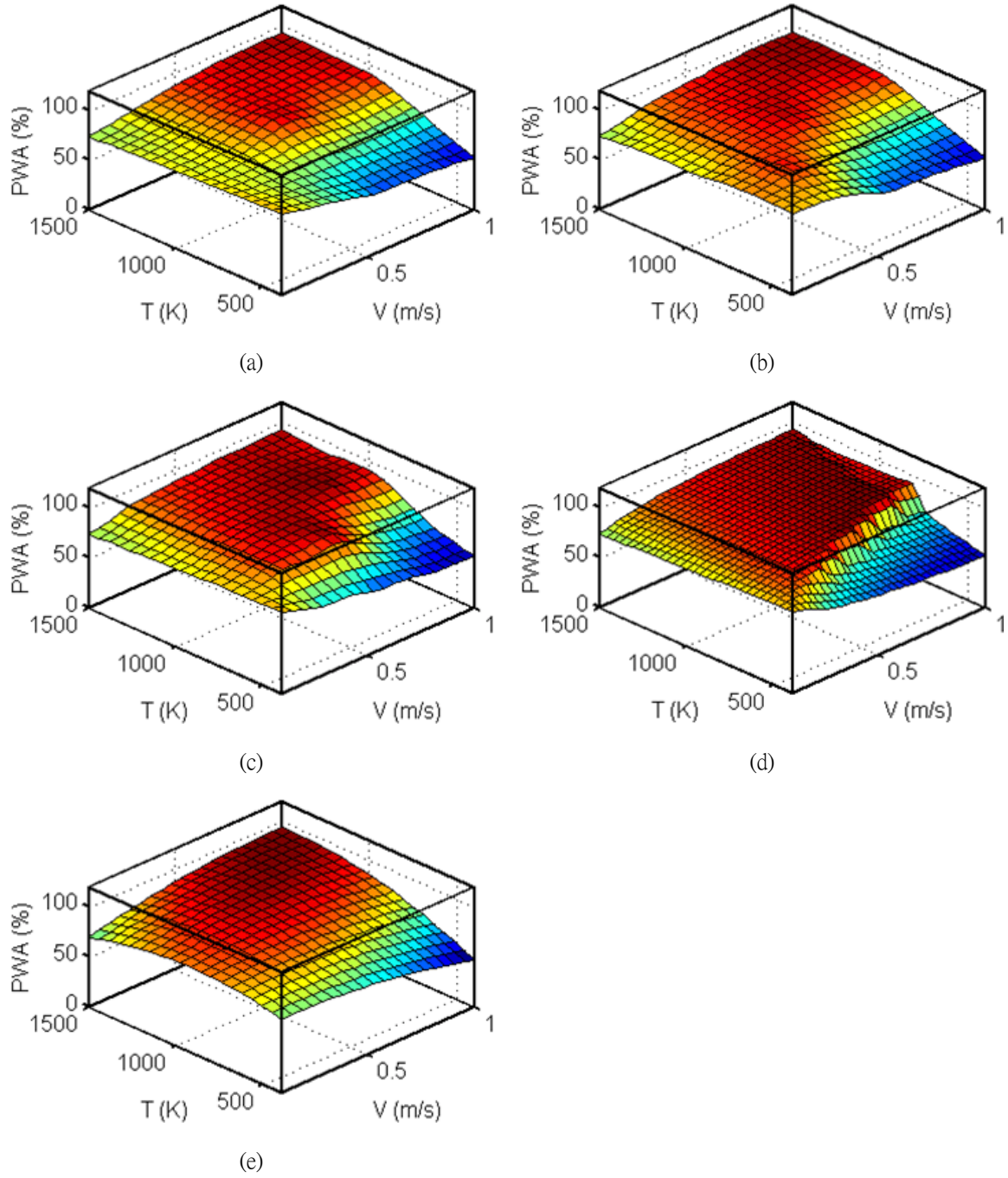


**Figure 3.2. Response Surfaces of the PWA.**

(a) 9-Point RBF, (b) 13-Point RBF, (c) 25-Point RBF, (d) 437-Point Sampling, and (e) 25-Point PRS.

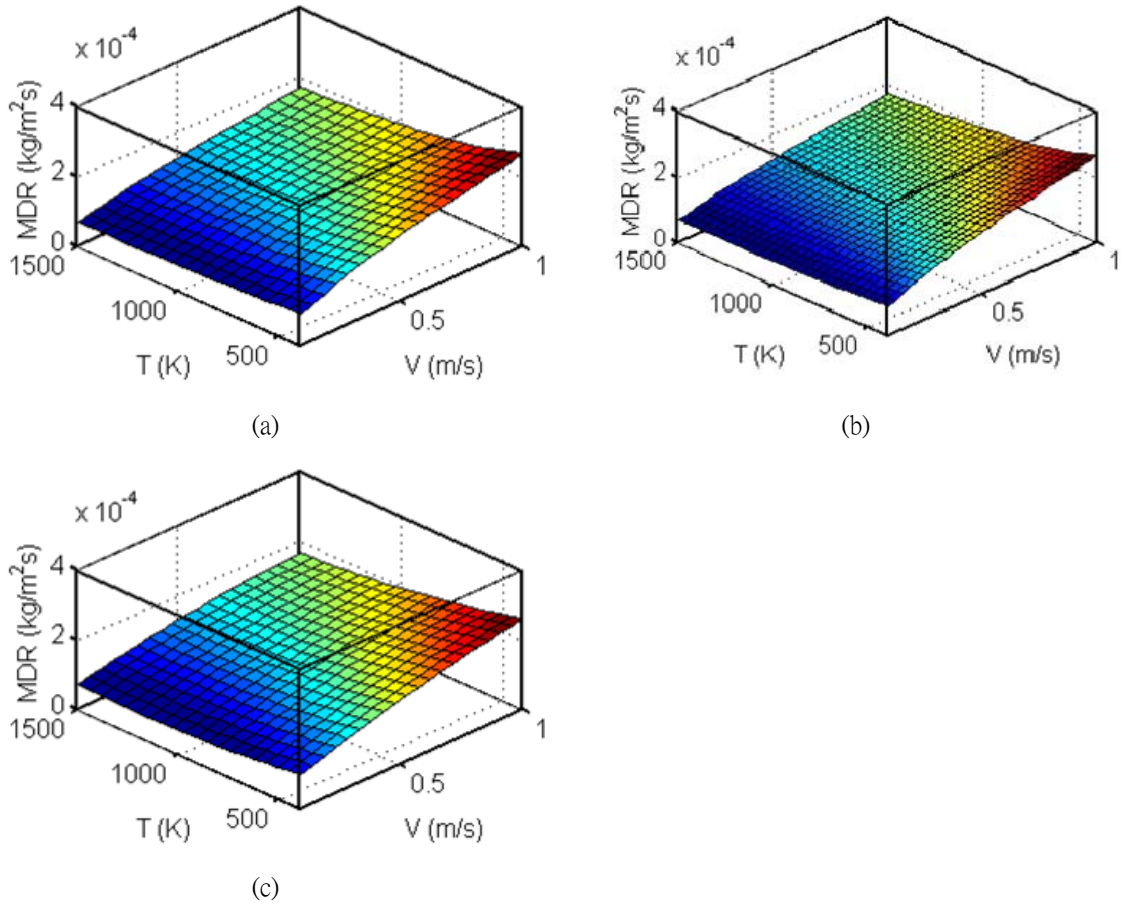


**Figure 3.3. Response Surfaces of the MDR.**

(a) 25-Point RBF, (b) 437-Point Sampling, and (c) 25-Point PRS.

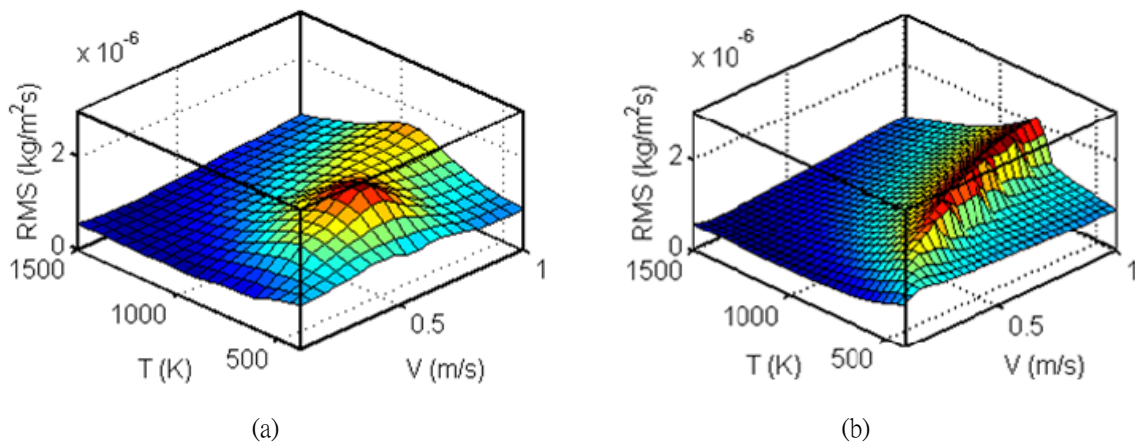


**Figure 3.4. Response Surfaces of the RMS.**

(a) 25-Point RBF and (b) 437-Point Sampling.

The 25-point RBF and the 437-point sampling of the KUR are shown in Figure 3.5. Several minor non-linear behaviors are found at the low velocity and the low temperature regions. The 25-point RBF has accurate approximations because it has good agreement with the 437-point sampling.

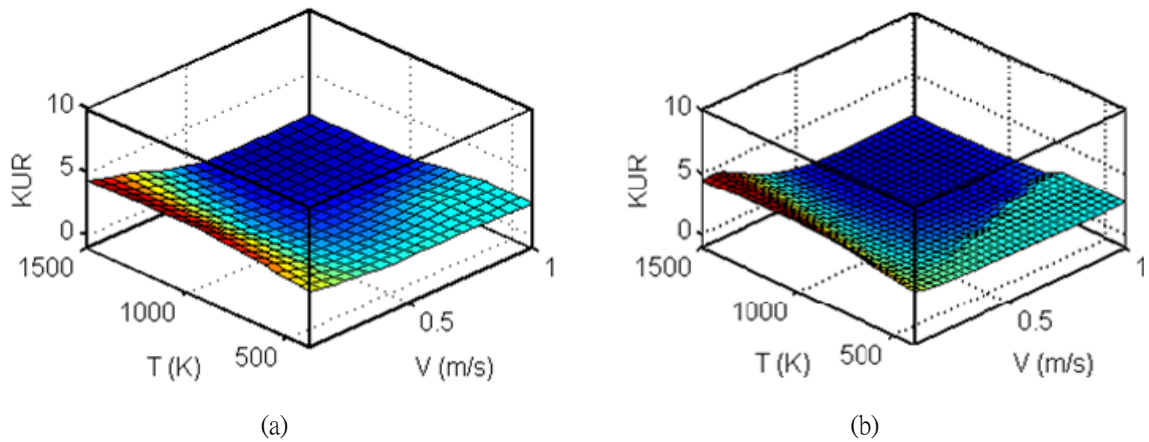


**Figure 3.5. Response Surfaces of the KUR.**  
**(a) 25-Point RBF and (b) 437-Point Sampling.**

### **3.4. Conclusion and Remarks**

The response surface models using PRS have less accuracy than the ones by the RBF because PRS has poor approximations when the responses are highly nonlinear. Three different amounts of sampling points have been utilized for RBF models, including 9-point, 13-point, and 25-point designs. Those models are firstly compared with the PRS models confirming that PRS is not suitable for the parametric modeling of the nonlinear responses in the CVD process. Those RBF models have also been validated with a 437-point sampling model and the 25-point designs have been found to have acceptable accuracy. The detailed information about the 437-point simulations is shown in the

Appendix I. Those responses then can be utilized to optimize the CVD process. In the next chapter, several different optimization formulations will be used to modify existing systems and design new ones to produce better film characteristics and deposition rates in the thin films of CVD process.

The proposed RBF can be utilized to parametrically model the responses in any other thermal systems. It is especially useful when the responses are highly nonlinear. The complexity of the RBF increases with the increasing number of the design variables as well as the sampling points. To simplify the RBF, the designer can efficiently define the locations of the sampling points instead of using the uniformly distributed ones. One possible method is the Latin Hypercube Sampling [93]. For the moderate-scale responses,  $5^N$ -uniformly distributed sampling has been found to be a good choice.

## **Chapter 4.**

### **Optimization of the CVD Process**

#### ***4.1. Introduction***

The response surface models are used to formulate the optimization problems of the CVD process in this chapter. Better operating conditions are expected to be found to improve the performance of the CVD process. The objective and constraint functions are formulated by the RBF models of the CVD responses. For higher productivities, one of the objective functions is to maximize the PWA while another one is to maximize the MDR. On the consideration of the uniformity of the deposition, the RMS and the KUR are subject to certain quantitative levels. Both constraints of the deposition uniformity are very significant to the locations of the optimal operating conditions.

#### ***4.2. Problem Formulations***

In a general CVD process, the PWA and the MDR should be maximized in order to obtain the highest productivity, and two global uniformity factors, the RMS and the KUR are required to satisfy some desirable guidelines. Therefore, three optimization formulations are proposed. The first one is to maximize the PWA with constraints on the RMS and the KUR. The second one is to maximize the MDR with the same constraints on the RMS and the KUR. They will be discussed in this section. There are three different ways to formulate optimization problems which deal with the both disciplines, the PWA and the MDR. Both of the PWA and the MDR are to be maximized in terms of



a penalty function subject to the same constraints of the uniformities. Besides the multi-objective formulation, the PWA is to be maximized subject to a desired level of the MDR. On the contrary, the MDR is lastly maximized subject to the constraint of the PWA. The detailed information about the optimal solutions is given in the later subsessions.

#### 4.2.1. Example 1: Maximizing the PWA

The first formulation is to maximize the PWA while satisfying the constraints of the RMS and the KUR. The maximization of the PWA is essential to practical needs in terms of yielding higher productivities of micro-devices and greater capacities of potential fabrication sources. It can be formulated as follows:

$$\begin{aligned}
 & \underset{V,T}{Max} && PWA \\
 & s.t. && RMS \leq RMS_U \\
 & && KUR \leq KUR_U \\
 & && V_L \leq V \leq V_U \\
 & && T_L \leq T \leq T_U
 \end{aligned} \tag{4.1}$$

The bounds of the design variables are slightly smaller than the sampling domain of the responses surface modeling because the interior of the responses surface model has better approximation than its edges. The chosen bounds are  $V_L = 0.2$  m/s,  $V_U = 0.9$  m/s,  $T_L = 400$  K, and  $T_U = 1400$  K. The upper bounds of the RMS and the KUR are defined as  $RMS_U = 1.35 \times 10^{-6}$  and  $KUR_U = 2.62$  respectively. All functions are approximated using the 25-point RBF and the optimization problem is solved by the optimization toolbox in MATLAB®.

Figure 4.1 marks the location of the optimal design by a black dot. The dash contour lines represent the objective function, PWA. The boundaries of the uniformity constraints are plotted by the solid curves and the infeasible regions are hatched with colors. Because the feasible region is not a convex region, many local optimal solutions exist. To overcome this problem, multiple starting points are used to find the optimal solution. The optimal solution is  $(V^*, T^*) = (0.75, 1009)$  and its feasibility is verified by FLUENT simulation. Furthermore, the best feasible setting in the 437 samplings,  $(V^*, T^*) = (0.75, 1000)$ , verifies the obtained optimal result. The optimal solution also shows good agreement with Figure 3.2 (d). The temperature of the susceptor is a significant factor in the control of the working area and the uniformity. If the inlet velocity is fixed at the optimal, the working area decreases dramatically as well as the uniformity constraints are mostly violated when temperature drops from 1000 to 500 K.

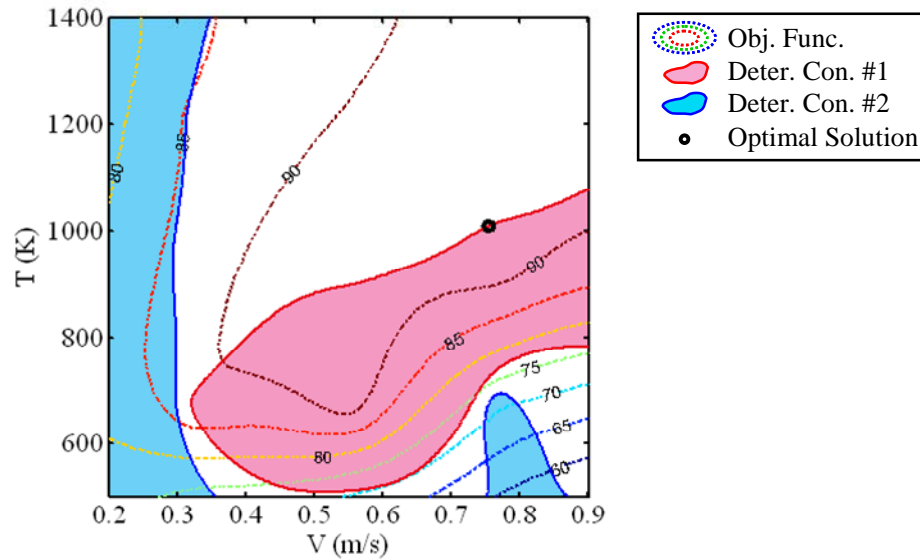


**Figure 4.1. Optimal Solution of Maximizing the PWA.**

### 4.2.2. Example 2: Maximizing the MDR

The second formulation is to maximize thin-film deposition rate while controlling global uniformity factor within certain bounds. The mathematical form is expressed as:

$$\begin{aligned}
 & \underset{V,T}{Max} && \text{MDR} \\
 & s.t. && \text{RMS} \leq \text{RMS}_U \\
 & && \text{KUR} \leq \text{KUR}_U \\
 & && V_L \leq V \leq V_U \\
 & && T_L \leq T \leq T_U
 \end{aligned} \tag{4.2}$$

Same constraints of surface uniformities as first formulation are considered within the same design domain. The feasible regions and the optimal solution are shown in Figure 4.2. Similarly, multiple starting points are used to find the global optimal solution because the feasible region is not convex. The optimal solution of 25-point RBF model is  $(V^*, T^*) = (0.9, 500)$ , and its feasibility is also verified by FLUENT simulation. The solution is verified while exactly same optimal solution is found in the 437 point sampling and the previous observations in Figure 3.3. Both the inlet velocity and the susceptor temperature are important to the quantity of the deposition rate and the conditions of the uniformity constraints. High velocity and low temperature provide highest deposition rate in the Eq. (4.2); however, they lead to smallest working area in the Eq. (4.1). A multi-objective formulation will be considered to compensate the decision of design variables.

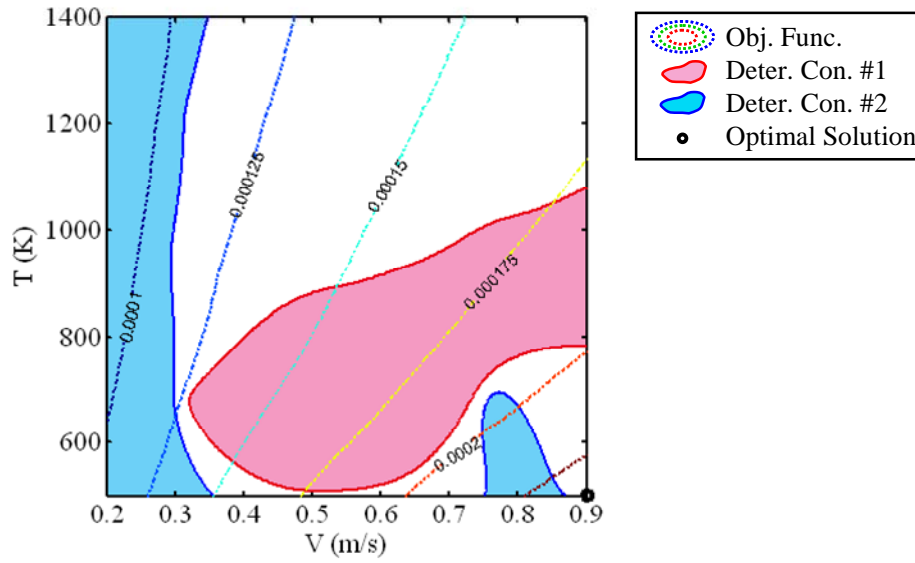


Figure 4.2. Optimal Solution of Maximizing the MDR.

#### 4.2.3. Example 3: A Multi-Objective Formulation

The third formulation is to maximize the PWA and the MDR simultaneously with the same constraints of the RMS and the KUR described previously. Instead of optimizing the PWA and MDR individually, it would be more practical to form a multi-objective optimization problem. Using a simple normalized sum of these two functions, an optimization problem is listed as:

$$\begin{aligned}
 & \underset{V, T}{Max} \quad \frac{PWA}{PWA_m} + \frac{MDR}{MDR_m} \\
 & s.t. \quad RMS \leq RMS_U \\
 & \quad \quad KUR \leq KUR_U \\
 & \quad \quad V_L \leq V \leq V_U \\
 & \quad \quad T_L \leq T \leq T_U
 \end{aligned} \tag{4.3}$$

where the PWA and the MDR are normalized by their maximum quantities within the 25 samplings,  $PWA_m = 93.63$  and  $MDR_m = 2.664 \times 10^{-4}$ . Same constraints for the film

uniformity are utilized. The feasibility and the optimality are shown in Figure 4.3, where the global optimal solution is obtained from multiple starting points. The optimal solution is  $V^* = 0.9$  m/s and  $T^* = 1079$  K, which is verified in 437 samplings,  $V^* = 0.9$  m/s and  $T^* = 1100$  K. The FLUENT simulation also confirms the feasibility of the optimal operation setting. Since a multi-objective formulation is used, the optimal solution is a compromised solution between the PWA and the MDR. High inlet velocity is found to be the optimal simply because it leads to high MDR and large PWA. However, the decision of the susceptor temperature is crucial. Although low temperature provides high MDR, the PWA decreases massively. As shown in Figure 4.3, a feasible and moderate setting of the susceptor temperature is found to compensate for the unacceptable PWA and satisfy the desired uniformity control.

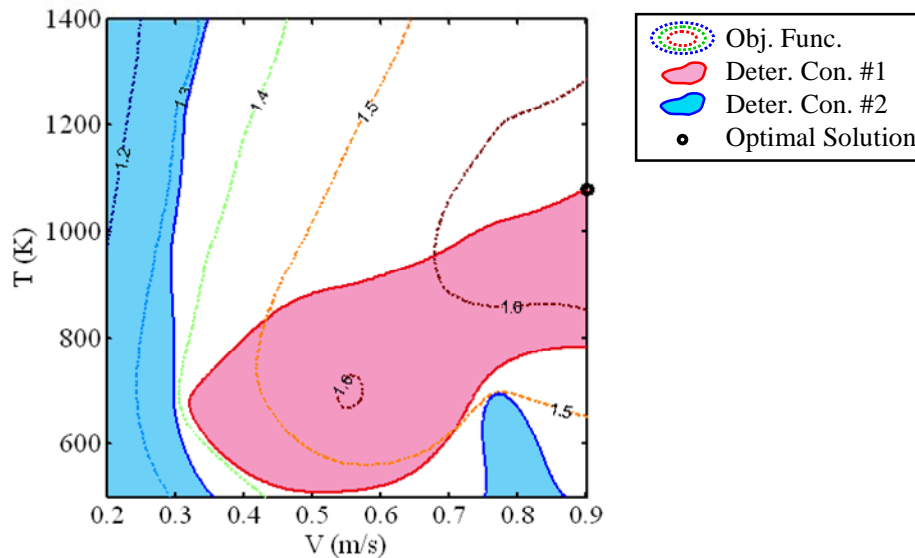


**Figure 4.3. Optimal Solution of the Multi-Objective Formulation.**

#### 4.2.4. Example 4: Maximizing the PWA Subject to Constraint of Deposition Rate

The forth formulation is to maximize the working area on the susceptor subject to the same desired constraints of the global uniformity factors described previously and an additional constraint on the deposition rate. It is expressed as follows:

$$\begin{aligned}
 & \underset{V,T}{Max} \quad PWA \\
 & s.t. \quad RMS \leq RMS_U \\
 & \quad \quad KUR \leq KUR_U \\
 & \quad \quad MDR_L \leq MDR \\
 & \quad \quad V_L \leq V \leq V_U \\
 & \quad \quad T_L \leq T \leq T_U
 \end{aligned} \tag{4.4}$$

where the lower bound of the MDR constraint is considered as  $MDR_L = 1.5 \times 10^{-4} \text{ kg/m}^2\text{s}$ . Figure 4.4 shows the feasible regions in white background color and the infeasible ones in three different colors, where red color is used for the first constraint, purple area indicates the infeasible domain of the second constraint, and the blue one is for the third MDR constraint. Similar to the previous examples, a strategy of using multiple starting points is used to resolve the convergence problem due to the disjoint feasible region. The optimal solution is found the same as the Example 1 because the constraint of the MDR is not active. The FLUENT simulation verifies the result and the 437-point samplings show good agreement with it.

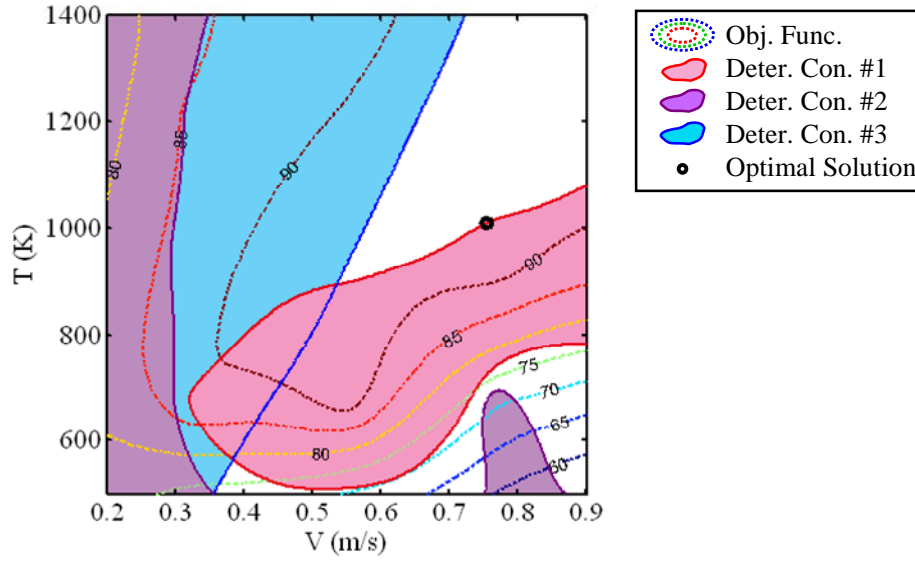


Figure 4.4. Optimal Solution of Maximizing the PWA Subject to the MDR Constraint.

#### 4.2.5. Example 5: Maximizing the MDR Subject to Constraint of Working Area

The last example is to maximize the MDR subject to the constraints of the uniformity factors and an additional constraint of the PWA, which is written as follows:

$$\begin{aligned}
 & \underset{V, T}{Max} && \text{MDR} \\
 & s.t. && \text{RMS} \leq \text{RMS}_U \\
 & && \text{KUR} \leq \text{KUR}_U \\
 & && \text{PWA}_L \leq \text{PWA} \\
 & && V_L \leq V \leq V_U \\
 & && T_L \leq T \leq T_U
 \end{aligned} \tag{4.5}$$

where the PWA is desired to exceed the lower bound of  $\text{PWA}_L = 85\%$ . The feasible region is narrower than the Example 2 due to the additional constraint, shown in Figure 4.5, and the optimal design in the Example 2 is no longer feasible in the Eq. (4.5).

Multiple starting points show the optimal solution is located at  $V^* = 0.9$  m/s and  $T^* = 1079$  K, which is verified by the FLUENT simulation and the 437 point samplings.

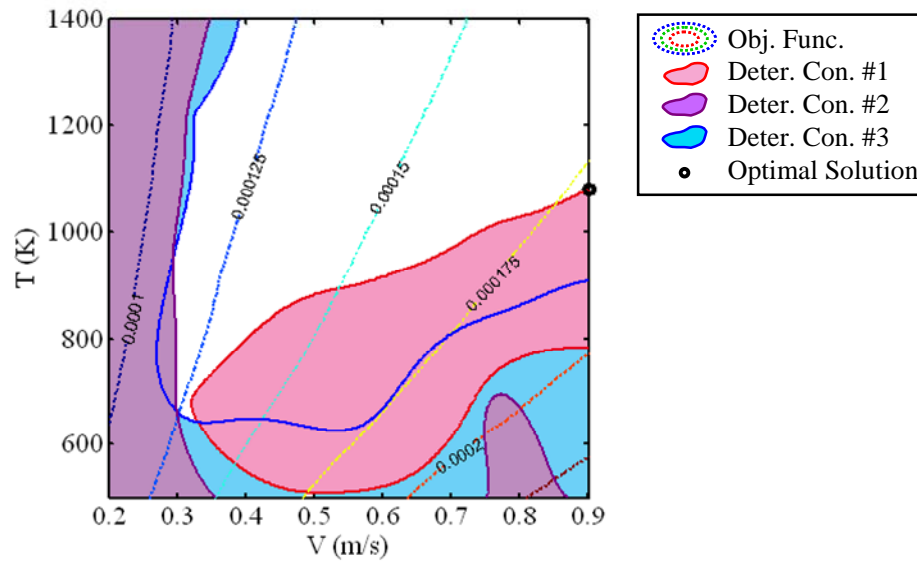


**Figure 4.5. Optimal Solution of Maximizing the MDR Subject to the PWA Constraint.**

#### 4.2.6. Results

The deposition process of silicon from silane in a vertical impinging CVD reactor has been modeled and studied. Two quality factors, the Percentage of Working Area and the Mean of Deposition Rate were defined and two global uniformity factors, the Root Mean Square and the Surface Kurtosis, were modeled. The responses were approximated using the Radial Basis Function with respect to the two operation parameters – the inlet velocity and the susceptor temperature. The approximating models were compared with models from a Polynomial Response Surface and validated against a 437-point sampling surface. Using the RBF models, five optimization formulations were proposed to



maximize the productivity while maintaining a specific minimum level of the global uniformity factors. The obtained optimal solutions of the design variables have been verified by the simulations at the optimal points, and the solutions were found to be all feasible. The detailed information about the optimal solutions of the 25-point models and the 437-sampling models is shown in Table 4.1. Good agreements have been found between the optimization with 25-point models and 437-samplings. Therefore, not only the 25-point RBF models have fairly good approximations of the responses of the CVD process, but they are capable of providing correct optimal solutions. It is expected that the same methodology can be used in the deposition of many other materials such as titanium nitride (TiN), gallium nitride (GaN), silicon carbide (SiC), etc.

**Table 4.1. Optimal Solutions and the Corresponding Responses for Examples 1 to 5 with the 25-Point RBF Models and the 437-Sampling Simulations.**

Example #	Models	Optimal Solution	PWA (%)	MDR (kg/m <sup>2</sup> s)	RMS (kg/m <sup>2</sup> s)	KUR
1	25-point	(0.75, 1009)	93.78	1.682E-4	1.345E-6	1.690
	437-point	(0.8, 1000)	93.63	1.741E-4	1.369E-6	1.707
2	25-point	(0.9, 500)	56.13	2.354E-4	9.825E-7	2.611
	437-point	(0.9, 500)	57.35	2.332E-4	9.751E-7	2.628
3	25-point	(0.9, 1079)	91.07	1.779E-4	1.351E-6	1.726
	437-point	(0.9, 1100)	93.63	1.785E-4	1.255E-6	1.692
4	25-point	(0.75, 1009)	93.78	1.682E-4	1.345E-6	1.690
	437-point	(0.8, 1000)	93.63	1.741E-4	1.369E-6	1.707
5	25-point	(0.9, 1079)	91.07	1.779E-4	1.351E-6	1.726
	437-point	(0.9, 1100)	93.63	1.785E-4	1.255E-6	1.692

### ***4.3. Optimization with Design Uncertainties***

If the design variables have some design uncertainties, they can be mathematically described by some statistical distributions. Due to the randomness of the design variables, the constraint values are no longer constant and have some probability distributions with respect to the random variables. Theoretically, the probabilities of the violations of the performance constraints are non-zero; therefore, an optimal solution with zero failure probabilities does not exist. A lower bound is needed for these probabilistic constraints where the failure probabilities are subject to some allowable level. For most engineering practices, the allowable failure probability is less than 1 %.

Suppose that the inlet velocity and the susceptor temperature are normally distributed random variables with the standard deviations of 0.02 m/s and 20 K respectively. The mean of the distributions are located at the optimal solutions obtained from the previous optimization problems. For examples 1 to 5, Monte Carlo Simulations are utilized to evaluate the failure probabilities of the constraints with the given uncertainties, listed in Table 4.2. The active constraints in terms of the RMS function have the failure probabilities of 43.03 %, 50.23 %, 42.90 %, and 50.10 % for examples 1, 3, 4, and 5 respectively at their optimal solutions. Example 2 has a high failure probability of the KUR constraint, 12.73 %, at its optimal solution. Without the considerations of the design uncertainties, the thermal systems have high risks of the constraint violations resulting in massive defective productions. Additionally, the MCS results of the failure probabilities with lognormally distributed operating conditions are

shown in Table 4.2. Unacceptable results are also found as some of the constraints have failure probabilities far larger than 1 %.

**Table 4.2. Monte Carlo Simulations at the Optimal Solutions with Design Uncertainties,  $\sigma_v = 0.02$  and  $\sigma_T = 20$ , for Examples 1 to 5.**

Example #	Optimal Solution	Distribution of Uncertainty	MCS of Con. #1	MCS of Con. #2	MCS of Con. #3
1	(0.75, 1009)	Normal	43.03 %	0 %	—
		Lognormal	43.13 %	0 %	—
2	(0.9, 500)	Normal	0 %	12.73 %	—
		Lognormal	0 %	12.66 %	—
3	(0.9, 1079)	Normal	50.23 %	0 %	—
		Lognormal	50.35 %	0 %	—
4	(0.75, 1009)	Normal	42.90 %	0 %	0 %
		Lognormal	43.02 %	0 %	0 %
5	(0.9, 1079)	Normal	50.10 %	0 %	0 %
		Lognormal	50.33 %	0 %	0 %

#### **4.4. Conclusion and Remarks**

The response surface models of the productivity and the uniformity of the CVD process have been utilized to formulate several different optimization problems. The maximization of the MDR and the PWA is the objective, while the uniformity factors, the RMS and the KUR, are subject to certain acceptable limit. With different definitions of the objective and constraint functions, different optimal operating conditions have been found and validated by comparing with the numerical simulations. The proposed strategy

up to this point, which includes the definitions of the performance responses, the parametric modeling using the RBF, and the optimization in terms of those response surface models, can be applied to any other kinds of thermal systems than the CVD process to modify existing systems and design new ones with better operating conditions.

However, the optimal design of the thermal system becomes unstable if the uncertainties exist in the design. As the traditional deterministic optimization algorithm pushes the design variables to the optimality, they are often on the limit state of the performance constraints or very close to them. The existence of the design uncertainties gives high probabilities of that the constraint limits are violated at the optimal solutions. Thus, an improved strategy is highly necessary to optimize the thermal system with design uncertainties. In the next chapter, the Reliability-Based Design Optimization is discussed and utilized to solve the optimization problems with random design variables.

## Chapter 5.

### Reliability-Based Design Optimization (RBDO)

#### 5.1. Introduction

Optimization techniques have been well developed and widely utilized to seek for better engineering designs in terms of reducing the system cost and enhancing the performance or the quality. Traditionally, engineering design problems are formulated as a deterministic optimization problem while neglecting the uncertainties of design variables. Under the deterministic optimization formulation, the optimal designs are selected based on the feasibility and optimality. However, the existence of uncertainties on the design variables will lead to the violations of constraints and destroy the optimality. To this end, Reliability-Based Design Optimization (RBDO) has been developed to provide a much better design of which the probability of system failures is reduced to an acceptable level.

#### General RBDO Formulation

Consider the random design variables,  $\mathbf{X}$ , where the  $j^{th}$  random design variable,  $X_j$ , has an expected value of  $d_j$  and a standard deviation of  $\sigma_j$ . Instead of using the original deterministic optimization formulation as follows:

$$\begin{aligned} \underset{\mathbf{d}}{Min} \quad & z(\mathbf{d}) \\ \text{s.t.} \quad & g_i(\mathbf{d}) \leq 0 \quad i = 1 \dots n \end{aligned} \tag{5.1}$$

a probabilistic design optimization is formulated as follows:

$$\begin{aligned}
& \underset{d}{Min} \quad z(\mathbf{d}) \\
& s.t. \quad P[g_i(\mathbf{X}) > 0] \leq P_{f,i} \quad i = 1 \dots n
\end{aligned} \tag{5.2}$$

where  $P_{f,i}$  is the  $i^{th}$  allowable probability of the system failure. Mathematically, probabilities of the system failure,  $P[g_i(\mathbf{X}) > 0]$ , can be calculated by an integral of its Joint Probability Density Function (JPDF),  $f_i(\mathbf{x})$ , within the infeasible domain, shown as follows:

$$P[g_i(\mathbf{X}) > 0] = \int_{g_i(\mathbf{X}) > 0} \dots \int f_i(\mathbf{x}) dx_1 \dots dx_N \tag{5.3}$$

However, it is very computationally expensive to evaluate the JPDF and the failure probability in Eq. (5.3).

## 5.2. Early Definitions of Reliability Indices

Instead of computing the integral in Eq. (5.3), several researchers have defined quantitative measures in the field of reliability analysis to evaluate the probabilities of system failures. Those are called reliability indices. The early definitions of those reliability indices are introduced in this subsection.

### 5.2.1. Cornell Reliability Index

*Cornell* [94] provided another approach to evaluate the failure probability by

$$P[g_i(\mathbf{X}) > 0] \cong \Phi(-\beta_{C,i}) \tag{5.4}$$

where  $\Phi$  is the Standard Normal Cumulative Distribution Function and  $\beta_{C,i}$  is the Cornell reliability index for the  $i^{th}$  constraint, which is given by

$$\beta_{C,i} = \frac{-E[g_i(\mathbf{X})]}{\sqrt{\text{Var}[g_i(\mathbf{X})]}} \quad (5.5)$$

In Eq. (5.5),  $E[g_i(\mathbf{X})]$  is the expected value of the  $i^{\text{th}}$  constraint corresponding to the random variable,  $\mathbf{X}$ , and  $\text{Var}[g_i(\mathbf{X})]$  is the coefficient of variance of the constraint. These two statistical quantities can be obtained by Monte Carlo Simulations (MCS) but MCS is still pretty costly.

*Madsen* [95] introduced the First-Order Second-Moment (FOSM) method to express the Cornell reliability index. First, a linear Taylor expansion of the nonlinear constraint at some design variable,  $\mathbf{x}_T$ , is given as follows

$$g_i(\mathbf{X}) \cong g_i(\mathbf{x}_T) + (\mathbf{X} - \mathbf{x}_T) \cdot \nabla_{\mathbf{x}} g_i(\mathbf{x}_T) \quad (5.6)$$

The FOSM Cornell reliability index can then be expressed by

$$\begin{aligned} \beta_{C,i}^{\text{FOSM}} &= \frac{-\{g_i(\mathbf{x}_T) + (E[\mathbf{X}] - \mathbf{x}_T) \cdot \nabla_{\mathbf{x}} g_i(\mathbf{x}_T)\}}{\sqrt{\text{Var}[\mathbf{X} \cdot \nabla_{\mathbf{x}} g_i(\mathbf{x}_T)]}} \\ &= \frac{-\{g_i(\mathbf{x}_T) + (\mathbf{d} - \mathbf{x}_T) \cdot \nabla_{\mathbf{x}} g_i(\mathbf{x}_T)\}}{\sqrt{\text{Var}[\mathbf{X} \cdot \nabla_{\mathbf{x}} g_i(\mathbf{x}_T)]}} \end{aligned} \quad (5.7)$$

Since

$$\begin{aligned} \text{Var}\left[\sum_{k=1}^N X_k \nabla_{x_k} g_i(\mathbf{x}_T)\right] &= \sum_{k=1}^N \sum_{m=1}^N \text{Cov}[X_k \nabla_{x_k} g_i(\mathbf{x}_T), X_m \nabla_{x_m} g_i(\mathbf{x}_T)] \\ &= \sum_{k=1}^N \sum_{m=1}^N \nabla_{x_k} g_i(\mathbf{x}_T) \nabla_{x_m} g_i(\mathbf{x}_T) \text{Cov}[X_k, X_m] \\ &= \nabla_{\mathbf{x}} g_i(\mathbf{x}_T) \cdot \mathbf{\Sigma} \cdot \nabla_{\mathbf{x}} g_i(\mathbf{x}_T) \end{aligned} \quad (5.8)$$

where  $\mathbf{\Sigma} \equiv \sum_{k=1}^N \sum_{m=1}^N \text{Cov}[X_k, X_m] \mathbf{e}_k \mathbf{e}_m^T$  is the covariance matrix, the  $\beta_{C,i}^{\text{FOSM}}$  becomes

$$\beta_{C,i}^{FOSM} = \frac{-\{g_i(\mathbf{x}_T) + (\mathbf{d} - \mathbf{x}_T) \cdot \nabla_{\mathbf{x}} g_i(\mathbf{x}_T)\}}{\sqrt{\nabla_{\mathbf{x}} g_i(\mathbf{x}_T) \cdot \boldsymbol{\Sigma} \cdot \nabla_{\mathbf{x}} g_i(\mathbf{x}_T)}} \quad (5.9)$$

For the special case of mutually independent random variable, i.e.  $Cov[X_k, X_m] = 0$  for  $k \neq m$  otherwise  $Cov[X_k, X_k] = Var[X_k] = \sigma_k^2$ , the  $\beta_{C,i}^{FOSM}$  reduces to a simpler form as follows

$$\beta_{C,i}^{FOSM} = \frac{-\{g_i(\mathbf{x}_T) + (\mathbf{d} - \mathbf{x}_T) \cdot \nabla_{\mathbf{x}} g_i(\mathbf{x}_T)\}}{\|\boldsymbol{\sigma} \cdot \nabla_{\mathbf{x}} g_i(\mathbf{x}_T)\|} \quad (5.10)$$

where  $\boldsymbol{\sigma} = \sum_{j=1}^N \sigma_j \mathbf{e}_j \mathbf{e}_j$  is the standard deviation matrix. If the Taylor expansion in Eq. (5.6)

is evaluated at the mean value  $\mathbf{d}$ , i.e.  $\mathbf{x}_T = \mathbf{d}$ , the method is called Mean-Value First-Order Second-Moment (MVFOSM) [95]. From Eq. (5.10), the MVFOSM Cornell reliability index is given by

$$\beta_{C,i}^{MVFOSM} = \frac{-g_i(\mathbf{d})}{\|\boldsymbol{\sigma} \cdot \nabla_{\mathbf{x}} g_i(\mathbf{d})\|} \quad (5.11)$$

The evaluation of the failure probability using  $\beta_{C,i}^{MVFOSM}$  only requires  $N + 1$  function calls (FCs), which is less costly than the integral method in Eq. (5.3) and the original Cornell reliability index in Eq. (5.5).

### 5.2.2. Chance Constrained Programming (CCP)

The Chance Constrained Programming (CCP) method [96-101] has been introduced to convert the probabilistic constraints in RBDO problems to solvable



deterministic constraints using the definition of  $\beta_{C,i}^{MVFOSM}$ . Considering the  $i^{th}$  original probabilistic constraint as follows

$$P[g_i(\mathbf{X}) > 0] \leq P_{f,i} \quad (5.12)$$

the failure probability,  $P[g_i(\mathbf{X}) > 0]$ , is approximated as follows [100]:

$$P[g_i(\mathbf{X}) > 0] \cong \Phi(-\beta_{C,i}^{MVFOSM}) \quad (5.13)$$

Defining an allowable reliability index as

$$\Phi(-\beta_{f,i}) \equiv P_{f,i} \quad (5.14)$$

and applying an inverse operator of the Standard Normal CDF,  $\Phi^{-1}(\bullet)$ , to Eq. (5.12), a deterministic constraint is then obtained:

$$-\beta_{C,i}^{MVFOSM}(\mathbf{d}) \leq -\beta_{f,i} \quad (5.15)$$

As a result, the following optimization formulation is considered instead of Eq. (5.2):

$$\begin{aligned} \underset{\mathbf{d}}{\text{Min}} \quad & z(\mathbf{d}) \\ \text{s.t.} \quad & -\beta_{C,i}^{MVFOSM}(\mathbf{d}) \leq -\beta_{f,i} \quad i = 1 \dots n \end{aligned} \quad (5.16)$$

Substituting Eq. (5.11) into Eq. (5.16), it can be rewritten as:

$$\begin{aligned} \underset{\mathbf{d}}{\text{Min}} \quad & z(\mathbf{d}) \\ \text{s.t.} \quad & \frac{g_i(\mathbf{d})}{\|\boldsymbol{\sigma} \cdot \nabla_x g_i(\mathbf{d})\|} \leq -\beta_{f,i} \quad i = 1 \dots n \end{aligned} \quad (5.17)$$

which is similar to the Approximate Moment Approach (AMA) at present times [102].

The CCP method using  $\beta_{C,i}^{MVFOSM}$  has one major problem [100]: The approximation of Eq. (5.5) leads to an inaccurate evaluation of the failure probability

when the constraint is nonlinear. Other researchers have defined different reliability indices to resolve this problem.

### 5.2.3. Veneziano Reliability Index

In order to have better approximation of the nonlinear constraint, *Veneziano* [103] introduced a new definition of the reliability index which utilized the information at the “tail” of the distribution instead of the expansion point at the mean value,  $\mathbf{d}$ , in Eq. (5.11). The concept aimed at the point where the constraint is active, namely  $\mathbf{x}_a \in \{\mathbf{x} | g_i(\mathbf{x}) = 0\}$ . Following the idea that the Cornell reliability index is geometrically the distance from the origin to the linearized constraint in the  $\mathbf{u}$ -space [95], *Veneziano* mapped the active point to the  $\mathbf{u}$ -space and measured the reliability index as the distance from the origin to the corresponding active point:

$$\beta_{V,i} = \|\mathbf{u}_{a,i}\| \quad (5.18)$$

where  $\mathbf{u}_{a,i} = \boldsymbol{\sigma}^{-1} \cdot (\mathbf{x}_a - \mathbf{d})$  and  $\mathbf{u}_{a,i} \in \{\mathbf{u} | g_i(\mathbf{u}) = 0\}$ . However,  $\beta_{V,i}$  varies with the decision of  $\mathbf{u}_{a,i}$  leading to an unstable determination of the reliability index.

### 5.3. Reliability Index Approach (RIA)

Since the failure probability can be evaluated by the standard normal CDF in terms of a reliability index instead of a costly integral of the PDF in the failure region, several different kinds of the reliability indices have been studied. The Cornell Reliability Index is a function in terms of expected value and the variance of the

constraint. The MVFOSM method linearly expands the constraint at the mean of the design variable; however, it lacks accurate approximation at the tale of the probability distribution. The Veneziano Reliability Index is often chosen from a set of reliability indices evaluated on the limit state of the performance constraint. It is still not the best way to evaluate the failure probability because the decision of the Veneziano Reliability Index is not unique and it lacks a systematic searching approach. In this session, a well utilized reliability index, Hasofer-Lind (H-L) Reliability Index, is introduced and implementation of the H-L Reliability Index to solve the RBDO problems is discussed.

### 5.3.1. Hasofer-Lind Reliability Index

To overcome the indeterminable problem in the definition of  $\beta_{v,i}$ , *Hasofer* and *Lind* [104] defined the reliability index as the shortest distance from the origin to the constraint in  $\mathbf{u}$ -space yielding a point-searching sub-problem:

$$\begin{aligned} \text{Min} \quad & \|\mathbf{u}_i\| \\ \text{s.t.} \quad & g_i(\mathbf{u}_i) = 0 \end{aligned} \quad (5.19)$$

The optimal solution of the Eq. (5.19) is called the Most Probable Point (MPP),  $\mathbf{u}_i^*$ , for the  $i^{th}$  constraint. The H-L reliability index then is given by

$$\beta_{HL,i} = \|\mathbf{u}_i^*\| \quad (5.20)$$

The evaluation of the failure probability using the  $\beta_{HL,i}$  is more accurate than  $\beta_{C,i}^{MVFOSM}$  because  $\mathbf{u}_i^*$  provides the information at the tail of the distribution. Another advantage is

that the determination of the  $\beta_{HL,i}$  is unique, unlike the various choices of the  $\beta_{V,i}$ , because only one  $\mathbf{u}_i^*$  is obtained from the MPP problem in Eq. (5.19).

Figure 5.1 illustrates the difference between  $\beta_{C,i}^{MVFOSM}$ ,  $\beta_{V,i}$ , and  $\beta_{HL,i}$ . Not only the  $\beta_{C,i}^{MVFOSM}$  can be evaluated by the Eq. (5.11), it also can be measured by the distance from the origin to the root of the perpendicular of the linearized constraint which is expanded at the origin in the standard normal space. The  $\beta_{V,i}$  is the distance from the origin to some active point on the constraint. The  $\beta_{HL,i}$  is measured by the distance from the origin to the MPP,  $\mathbf{u}_i^*$ , and can be obtained by iteratively solving the Eq. (5.19). The iteration process involves linearizations of the constraints at the perpendicular points,  $\mathbf{u}_i^{(m)}$ . More details about the MPP searching algorithms are discussed later.

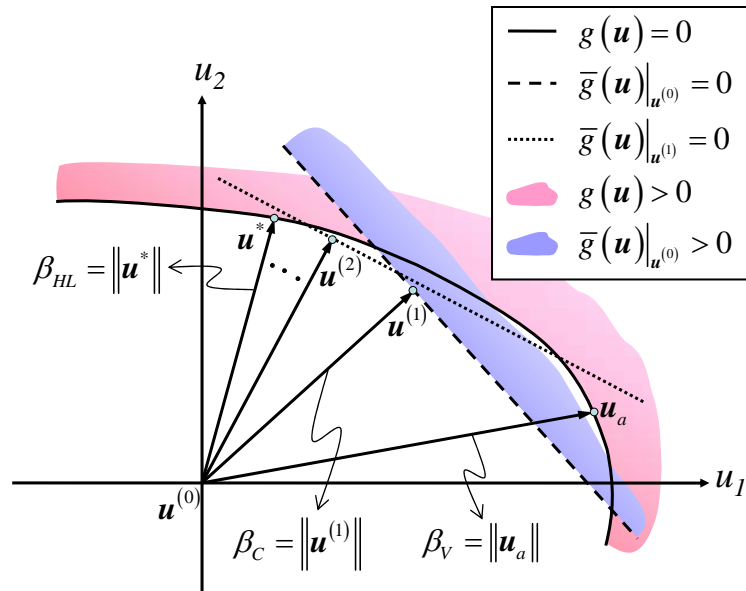


**Figure 5.1. Scheme of Three Different Kinds of the Reliability Indices: Cornell, Veneziano, and Hasofer-Lind Reliability Indices.**

Finally, the failure probability can be evaluated by

$$P[g_i(\mathbf{X}) > 0] \cong \Phi_{0,1}(-\beta_{HL,i}) \quad (5.21)$$

and the probabilistic constraint in Eq. (5.12) is converted to the deterministic formulation as follows:

$$-\beta_{HL,i}(\mathbf{d}) \leq -\beta_{f,i} \quad (5.22)$$

If the MPP can be obtained efficiently, the Eq. (5.22) will become a very useful formulation which includes the accurate information of the failure probability and can be solved with less computational efforts. It has become an important research to solve the MPP-searching problem in Eq. (5.19) and understand how it can be used to solve RBDO problems.

### 5.3.2. Most Probable Point (MPP)-Searching Algorithms

Many researchers then focused on how the MPP-problem is solved [104-106]. *Hasofer* and *Lind* [104] firstly suggested an iterative method, as known as the HL algorithm, to find the MPP at the foot of the perpendicular from the origin to the linear approximation at the tail of the variable distribution in  $\mathbf{u}$ -space, as known as the Normal Tail Approximation [95]. *Rackwitz* and *Fiessler* [105] developed a systematic procedure to complete the iterative method that *Hasofer* and *Lind* suggested. This method is called the HL-RF algorithm, also known as the Advanced First-Order Second-Moment (AFOSM) method, or the First-Order Reliability Method (FORM) at the present time. *Ayyub* and *Haldar* [106] have utilized a similar iterative scheme to find the MPP by FORM. With more function calls, higher order of the reliability analysis has been

utilized to provide better approximations of the performance constraints and have more accurate MPP, such as Second-Order Reliability Method (SORM) [95]. Beyond those iterative methods, the HL-RF algorithm is the most common one and will be discussed in detail in the following paragraph.

### HL-RF Iterative Algorithm

In the  $m^{th}$  iteration of the MPP searching process, the standard normal design variable for the  $i^{th}$  constraint,  $\mathbf{u}_i^{(m)}$ , in the MPP-problem in Eq. (5.19) is utilized as the expansion point of the first-order Taylor approximation of the constraint, which is given by

$$g_i(\mathbf{u}_i) \cong g_i(\mathbf{u}_i^{(m)}) + (\mathbf{u}_i - \mathbf{u}_i^{(m)}) \cdot \nabla_{\mathbf{u}} g_i(\mathbf{u}_i^{(m)}) \quad (5.23)$$

The foot of the perpendicular from the origin to the linearized constraint in Eq. (5.23),  ${}^{\perp}\mathbf{u}_i^{(m)}$ , is given by

$${}^{\perp}\mathbf{u}_i^{(m)} = (\mathbf{u}_i^{(m)} \cdot \boldsymbol{\mu}_i^{(m)}) \boldsymbol{\mu}_i^{(m)} \quad (5.24)$$

where  $\boldsymbol{\mu}_i^{(m)} \equiv \nabla_{\mathbf{u}} g_i(\mathbf{u}_i^{(m)}) / \|\nabla_{\mathbf{u}} g_i(\mathbf{u}_i^{(m)})\|$  is the unit vector of the linearized constraint. The

$\mathbf{u}_i^{(m+1)}$  is updated along the direction of  ${}^{\perp}\mathbf{u}_i^{(m)}$  can is defined as

$$\mathbf{u}_i^{(m+1)} = {}^{\perp}\mathbf{u}_i^{(m)} + \nu_i^{(m)} \boldsymbol{\mu}_i^{(m)} \quad (5.25)$$

where  $\nu_i^{(m)}$  is the coefficient for the update scheme. The Eq. (5.25) must satisfies

$$g_i(\mathbf{u}_i^{(m+1)}) = 0 \text{ so}$$

$$g_i(\mathbf{u}_i^{(m)}) + \left[ (\mathbf{u}_i^{(m)} \cdot \boldsymbol{\mu}_i^{(m)}) \boldsymbol{\mu}_i^{(m)} + \nu_i^{(m)} \boldsymbol{\mu}_i^{(m)} - \mathbf{u}_i^{(m)} \right] \cdot \nabla_{\mathbf{u}} g_i(\mathbf{u}_i^{(m)}) = 0 \quad (5.26)$$

or

$$\mathbf{v}_i^{(m)} = -g_i(\mathbf{u}_i^{(m)}) \left\| \nabla_u g_i(\mathbf{u}_i^{(m)}) \right\|^{-1} \quad (5.27)$$

Therefore, the iterative equation of the FORM is given as

$$\begin{aligned} \mathbf{u}_i^{(m+1)} &= \left[ \left( \mathbf{u}_i^{(m)} \cdot \boldsymbol{\mu}_i^{(m)} \right) - g_i(\mathbf{u}_i^{(m)}) \left\| \nabla_u g_i(\mathbf{u}_i^{(m)}) \right\|^{-1} \right] \boldsymbol{\mu}_i^{(m)} \\ &= \left[ \frac{\mathbf{u}_i^{(m)} \cdot \nabla_u g_i(\mathbf{u}_i^{(m)}) - g_i(\mathbf{u}_i^{(m)})}{\left\| \nabla_u g_i(\mathbf{u}_i^{(m)}) \right\|} \right] \frac{\nabla_u g_i(\mathbf{u}_i^{(m)})}{\left\| \nabla_u g_i(\mathbf{u}_i^{(m)}) \right\|} \end{aligned} \quad (5.28)$$

The iteration continues until convergence and the reliability index can be evaluated by substituting the  $\mathbf{u}_i^*$  to Eq. (5.20). The obtained reliability index by the HL-RF algorithm is then denoted as  $\beta_{HL,i}^{FORM}$ . The procedure of converting the probabilistic constraints to deterministic constraints with the  $\beta_{HL,i}^{FORM}$  is called the Safety Index Approach [100], or the Reliability Index Approach (RIA) at present time.

The technique of FORM has been introduced to find the MPP which has the shortest distance from the origin to the constraint in the standard normal space. However, the FORM does not guarantee the convergence of the MPP searching if the constraint is concave [107]. Wu [108] has introduced a procedure which utilized the linear approximation at the mean value to improve the efficiency of MPP searching with the FORM. This method is called the Advanced Mean Value First Order (AMVFO) method or the Advanced Mean Value (AMV) method at present time. In this research work, the MPP-searching problem is solved by a general Sequential Quadratic Programming (SQP)-based optimization toolbox, `fmincon`, in MATLAB®.

### **5.4. Other RBDO Algorithms**

Besides the RIA, several other algorithms have been introduced to solve the RBDO problems. Those include Performance Measure Approach (PMA) and Sequential Optimization and Reliability Assessment (SORA). The PMA [109] considers an inverse reliability analysis and converts the probabilistic constraints into deterministic formulations in terms of the performance measures. This approach also requires a sub-optimization problem which finds the Inverse Most Probable Points to evaluate the performance measures with the target reliabilities [104]. The sub-problem has been solved by several different kinds of iterative approaches, including the Advanced Mean Value [110-111], the Conjugate Mean Value (CMV) [112], and the Hybrid Mean Value (HMV) [112] methods. The SORA [113] considers the RBDO problems with a single-loop strategy where the optimization and the reliability assessment are employed. The constraints are shifted toward the feasible domain with certain level considering the uncertainties of the design variables. Afterward, the optimization problem is solved with those shifted constraints.

The PMA and the SORA have been well utilized to solve the RBDO problems because the RIA is reported to have some convergence problems [109] and is less efficient than the prior two methods [113]. In this research work, we focus on the RIA. We want to revisit the definition of the RIA and reveal the true reason for the convergence problem and the inefficiency of the RIA. A modified method is then proposed to resolve the convergence problem and solve the RBDO problems more efficiently.



## 5.5. Convergence Problem of Traditional Reliability Index

### ***Approach (TRIA)***

Since H-L Reliability Index has been defined by a measure of the shortest distance from the origin to the failure region in the standardly normalized variable space and utilized to quantify the failure probability, many RBDO methods utilizing the concept of reliability index have been introduced as the Reliability Index Approach (RIA) [100, 114-120]. In the RIA, a reliability analysis problem is formulated to find the reliability index for each performance constraint and the solutions are used to evaluate the failure probability. *Tu et al.* [109] pointed out a convergence problem associated with the numerical singularities in the TRIA and developed the Performance Measure Approach (PMA) to study the inverse reliability analysis instead of the reliability index. Since the numerical singularity only exists in some numerical extreme cases such as the standard deviation is very close to zero, it is not a major issue in engineering practices. Other than the numerical singularity associated with the tight standard deviations, the TRIA still often mysteriously fails to converge under the general setting. This convergence problem of the TRIA prompts many researchers select the PMA as a more efficient and robust choice for general nonlinear performance functions [112, 121]. The definition of the reliability index is revisited in the following.

A simple RBDO example shown in Figure 5.2 is used to illustrate this concept and the following relation holds:

$$P[g(X) > 0] = \int_{g>0} f(x) dx \quad (5.29)$$

where  $f(x)$  is the PDF of  $X$ . Using a mapping factor of  $x = d + \sigma u$  and assuming the random variables are normally distributed and uncorrelated [104], the corresponding standard normal CDF is illustrated in Figure 5.3, where  $u^*$  is the Most Probable Point (MPP) and has the shortest distance from the constraint to the origin. The H-L Reliability Index,  $\beta_{HL}$ , has been defined in Eq. (5.20). The MPP obtained from Eq. (5.19),  $u^*$ , has the shortest distance from the equality constraint to the origin. The failure probability is then evaluated by the Eq. (5.21).

Replacing the quantity of  $P_f$  by an equivalent standard normal CDF of the allowable reliability index,  $\beta_{HL,f}$ :

$$P_f \equiv \Phi(-\beta_{HL,f}) \quad (5.30)$$

and applying an inverse standard normal CDF operator,  $\Phi^{-1}$ , the original probabilistic optimization problem in Eq. (5.2) now becomes

$$\begin{aligned} \underset{d}{Min} \quad & z(d) \\ \text{s.t.} \quad & -\beta_{HL}(d) \leq -\beta_{HL,f} \end{aligned} \quad (5.31)$$

where  $\beta_{HL}$  is a function of  $d$  because  $u^*$  varies with respect to  $d$ . The original probabilistic constraint in Eq. (5.2) now is converted to the solvable deterministic formulation in Eq. (5.31).

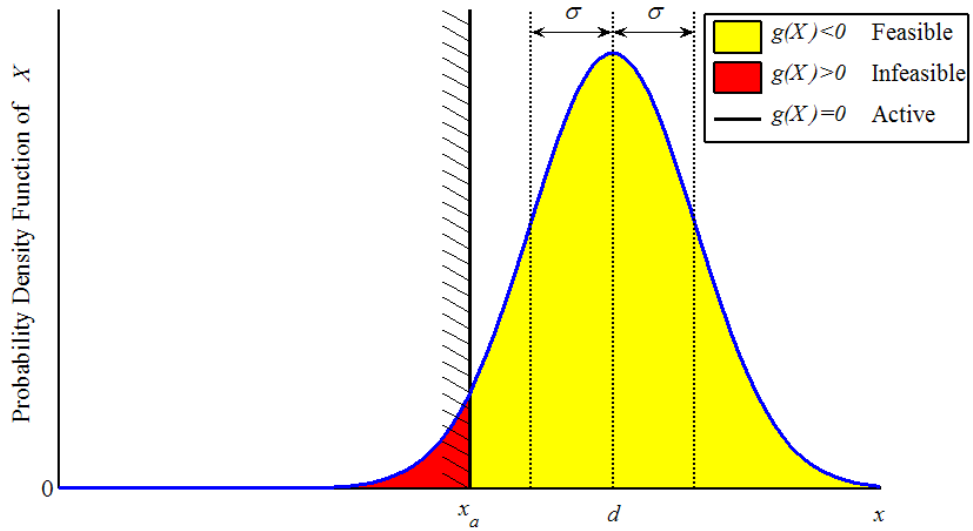


Figure 5.2. PDF of the Normally Distributed Random Variable,  $X$ .

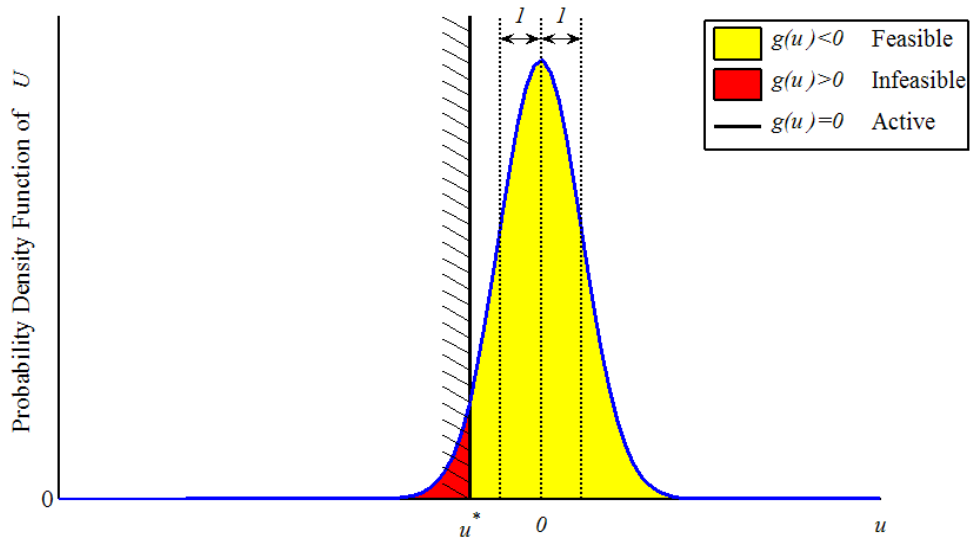


Figure 5.3. PDF of the Standard-Normally Distributed Random Variable,  $U$ .

As discussed in *Tu et al.* [109], the TRIA has a convergence problem during the MPP-searching process because it may not have any solution as the standard deviation is very small and  $\beta_{HL}$  becomes infinity. Fortunately, the numerical singularity originated

from very small standard deviations in an RBDO problem is not a critical issue in most practical engineering problems because variables with very small standard deviations can be treated as deterministic variables and the singularity can be removed. However, numerical results showed that the TRIA sometimes still fails to converge even with not so small standard deviations [121].

The real problem that leads to the convergence problems of the TRIA resides on the definition of the reliability index. The original reliability index is defined as the shortest distance from the origin to the failure region. If the origin is within the failure region, the current definition becomes invalid. However, the MPP sub-optimization problem of the RIA will still return a MPP “solution”. As shown in Figure 5.3 and Figure 5.4, both  $\boldsymbol{u}^*$  are considered as the MPP solutions even the  $\boldsymbol{u}^*$  is negative in Figure 5.3 but positive in Figure 5.4. Therefore, the optimization iteration of the TRIA may arrive at erratic solutions and cause convergence problems. One possible solution to avoid the convergence problem is to evaluate the failure probability of the design in each iteration. If the failure probability is larger than 50 %, the current design is considered as a failed design and the reliability index can be assigned as a negative value. However, the evaluation of the failure probability is not computationally efficient. To this end, a more efficient and robust solution is presented in the next session.

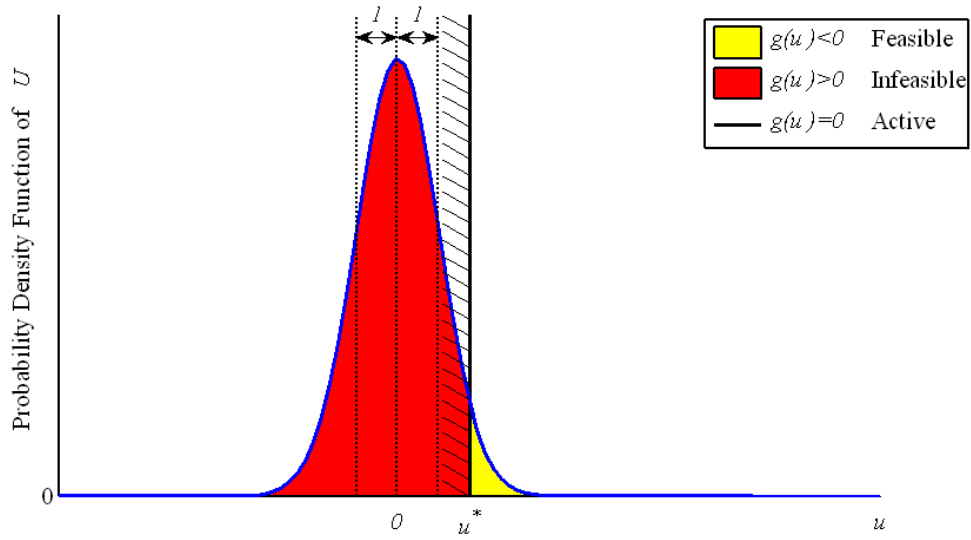


Figure 5.4. PDF of the Standard-Normally Distributed Random Variable,  $U$ .

## 5.6. Conclusion and Remarks

In the design optimization of the thermal systems, the existence of the design uncertainties cannot be easily ignored. In the chapter, we have found the optimal designs without the considerations of the design uncertainties have very high probabilities of the system failures. The failures of the thermal systems may cause huge loss in the productions and even result in dangerous situations for human lives. The strategies to consider the design uncertainties in the optimization process become very important in the study of the thermal systems.

The RBDO algorithms have been introduced to solve the optimization problems of the CVD process with design uncertainties. The TRIA utilizes the Hasofer-Lind Reliability Index in terms of the Most Probable Point in the standard normal space to evaluate the failure probabilities. Approximate constraints are then generated in terms of

the reliability index to replace the original probabilistic constraints. However, the TRIA suffers from the convergence problem when the design point is located in the infeasible domain during the optimization process. This problem may lead to incorrect optimal solutions which have unacceptable failure probabilities. Moreover, it may cause inefficient optimization process.

The main problem of the TRIA comes from the definition of the reliability index, which provides incorrect evaluations of the failure probabilities when the design point is located in the infeasible domain. A modified reliability index is proposed to provide correct evaluations of the failure probabilities despite of the position of the design points. The Modified Reliability Index Approach is then introduced to solve the RBDO problems of the CVD process with design uncertainties. In Chapter 6, the MRIA is firstly examined by several mathematical problems and verified by the Monte Carlo Simulations. In Chapter 7, the MRIA is applied to the five optimization problems in Chapter 4 with the considerations of the design uncertainties.

## Chapter 6.

### Modified Reliability Index Approach (MRIA) for RBDO

In this chapter, a new definition of the reliability index is proposed to correct this problem and a Modified Reliability Index Approach based on this definition is developed. The strategies to solve RBDO problems with non-normally distributed design variables by the MRIA are also investigated. Numerical examples using both the TRIA and the MRIA are compared and discussed.

#### 6.1. A New Reliability Index

As described in the previous session, the root of the convergence problems in the TRIA comes from the definition of the reliability index. The current definition of the reliability index fails to find the true MPP if the origin is within the failure region. To overcome this problem, a new reliability index is proposed in this section.

##### 6.1.1. Definition of the Modified Reliability Index

A new reliability index,  $\beta_M$ , is defined as follows:

$$\beta_M = \mathbf{u}^* \cdot \frac{\nabla_{\mathbf{u}} g(\mathbf{u}^*)}{\|\nabla_{\mathbf{u}} g(\mathbf{u}^*)\|} \quad (6.1)$$

This definition makes use of the gradient of the constraint at the MPP to differentiate whether the current design is safe or failed, i.e. the origin is within the failure region or

not. To this end, we will examine the MPP sub-problem in Eq. (4) to understand the relationship between  $\mathbf{u}^*$  and  $\nabla_{\mathbf{u}}g(\mathbf{u}^*)$ .

Using the method of Lagrangian Multiplier to solve the MPP sub-problem in Eq. (5.19), an auxiliary function is introduced as follows:

$$L(\mathbf{u}, \lambda) = (u_p u_r)^{\frac{1}{2}} + \lambda g(\mathbf{u}) \quad (6.2)$$

where  $\lambda$  is the Lagrangian multiplier. The optimal solution is given by solving  $\nabla L(\mathbf{u}, \lambda) = 0$ , which gives

$$\mathbf{e}_q \frac{\partial}{\partial u_q} \left[ (u_p u_r)^{\frac{1}{2}} + \lambda g(\mathbf{u}) \right] = 0 \quad (6.3)$$

and  $g(\mathbf{u}) = 0$  as  $\mathbf{e}_q$  stands for the  $q^{th}$  normal basis of  $\mathbf{u}$ . The Eq. (6.3) can be rewritten as:

$$\mathbf{e}_q \left[ \delta_{pq} u_p (u_r u_r)^{-\frac{1}{2}} + \lambda \frac{\partial g(\mathbf{u})}{\partial u_q} \right] = 0 \quad (6.4)$$

where  $\delta_{pq}$  is the Kronecker delta. From Eq. (6.4), the MPP is given by

$$\mathbf{u}^* = -\lambda \|\mathbf{u}^*\|^{-1} \nabla_{\mathbf{u}}g(\mathbf{u}^*) \quad (6.5)$$

The relation indicates that  $\nabla_{\mathbf{u}}g(\mathbf{u}^*)$  has whether the same direction or the opposite one with the direction of  $\mathbf{u}^*$ . Therefore, we can take advantages of this collinear relationship between  $\mathbf{u}^*$  and  $\nabla_{\mathbf{u}}g(\mathbf{u}^*)$  to modify the original definition of the reliability index as the new definition of  $\beta_M$  in Eq. (6.1). The new definition,  $\beta_M$ , is



identical to the original  $\beta_{HL}$  in Eq. (5.20) when the origin is outside the failure region and  $\beta_M$  becomes a negative quantity when the current design leads to system failure, i.e. the origin is within the failure region. In this way, the new reliability index can provide the correct solution.

### A Simple Illustrative Example

To illustrate the definition of the new reliability index, a simple linear probabilistic constraint is used here. Consider the failure probability of a linear constraint is given by

$$P[g(X) = -X + 10 > 0] \leq 0.13\% \quad (6.6)$$

where  $X \sim N(d, 1)$  and  $\nabla_u g(\mathbf{u})$  equals to a negative unit vector. Two different values of the design variable are selected for comparison,  $d = 13$  and 7. The MPPs are found to be  $u^* = -3$  for the first case and  $u^* = 3$  for the second one. However, the traditional reliability index,  $\beta_{HL}$ , gives the same values as 3. Then, the probability of failure in Eq. (5.21) results in the same answer as  $\Phi(-3) = 0.13\%$  that implies satisfactory for both cases that is obviously a wrong answer for the second case. Using the new definition of reliability index,  $\beta_M$ ,  $\mathbf{u}^* \cdot \nabla_u g(\mathbf{u}^*)$  becomes 3 and -3 for the first and second cases respectively. Therefore, the probabilities of failures correctly are evaluated correctly as  $\Phi(-3) = 0.13\%$  for the first case and  $\Phi(3) = 99.87\%$  for the second case.

Using the new definition of  $\beta_M$  in Eq. (6.1), the Eq. (5.21) now is rewritten as:

$$P[g(X) > 0] = \Phi(-\beta_M) \quad (6.7)$$

and the allowable failure probability,  $\beta_{M,f}$ , can be converted as:

$$P_f \equiv \Phi(-\beta_{M,f}) \quad (6.8)$$

In this way, the original probabilistic formulation becomes the deterministic formulation:

$$\begin{aligned} \underset{\mathbf{d}}{\text{Min}} \quad & z(\mathbf{d}) \\ \text{s.t.} \quad & -\beta_M(\mathbf{d}) \leq -\beta_{M,f} \end{aligned} \quad (6.9)$$

where  $\beta_M(\mathbf{d})$  varies with respect to  $\mathbf{d}$  because Eq. (6.1) is a function of  $\mathbf{u}^*$  and  $\mathbf{u}^*$  alters with  $\mathbf{d}$ .

### 6.1.2. Implementation of MRIA

After the original probabilistic optimization formulation in the Eq. (5.2) is transformed into the deterministic formulation in Eq. (6.9) using the new reliability index, we can apply the MRIA to solve RBDO problems.

In the MRIA, we first express  $\beta_M(\mathbf{d})$  in terms of  $\mathbf{d}$  using the first-order Taylor's expansion at the current design,  $\mathbf{d}^{(k)}$ . At the  $k^{th}$  iteration,  $\beta_M(\mathbf{d})$  can be written as the following:

$$\beta_M(\mathbf{d}) \cong \beta_M(\mathbf{d}^{(k)}) + (\mathbf{d} - \mathbf{d}^{(k)}) \cdot \nabla_{\mathbf{d}} \beta_M(\mathbf{d}^{(k)}) \quad (6.10)$$

Eq. (6.9) now becomes a deterministic optimization problem with linear constraints as follows:

$$\begin{aligned}
& \underset{d}{Min} \quad z(d) \\
& s.t. \quad -\beta_M(d^{(k)}) - (d - d^{(k)}) \cdot \nabla_d \beta_M(d^{(k)}) \leq -\beta_{M,f}
\end{aligned} \tag{6.11}$$

where  $\beta_M(d^{(k)})$  can be evaluated by solving the MPP sub-problem and applying the obtained  $u^*(d^{(k)})$  to Eq. (6.1). By taking the first derivative of  $\beta_d(d^{(k)})$  with respect to  $d$ ,  $\nabla_d \beta_M(d^{(k)})$  is obtained as:

$$\begin{aligned}
\nabla_d \beta_M(d^{(k)}) &= \frac{\partial [u^* \cdot \nabla_u g(u^*)]}{\partial d} \left\| \nabla_u g(u^*) \right\|^{-1} \\
&= \nabla_d u^* \cdot \nabla_u g(u^*) \left\| \nabla_u g(u^*) \right\|^{-1}
\end{aligned} \tag{6.12}$$

Given the fact from the transformation between the normally distributed and the standard-normally distributed design space, we have:

$$\nabla_d g(u^*, d) \cong \nabla_d u^* \cdot \nabla_u g(u^{(m)}, d^{(k)}) + \nabla_d g(u^{(m)}, d^{(k)}) \tag{6.13}$$

The feasibility of the MPP problem requires  $\nabla_d g(u^*, d) = 0$ ; therefore, at the optimal solution of the MPP problem, the Eq. (6.13) becomes:

$$\nabla_d u^* \cdot \nabla_u g(u^*) = -\nabla_d g(u^*) \tag{6.14}$$

Eq. (6.12) then becomes

$$\nabla_d \beta_M(d^{(k)}) = -\nabla_d g(u^*) \left\| \nabla_u g(u^*) \right\|^{-1} \tag{6.15}$$

and the final deterministic optimization formulation of Eq. (6.11), using the Eqs. (6.1) and (6.15), is obtained as follows:

$$\begin{aligned}
& \underset{d}{Min} \quad z(d) \\
& s.t. \quad -u^* \cdot \nabla_u g(u^*) \left\| \nabla_u g(u^*) \right\|^{-1} \\
& \quad + (d - d^{(k)}) \cdot \nabla_d g(u^*) \left\| \nabla_u g(u^*) \right\|^{-1} \leq -\beta_{M,f}
\end{aligned} \tag{6.16}$$

The main difference between the MRIA and the TRIA is in the first constant term of the constraint equation. In the MRIA, the constant term is obtained from the new definition of reliability index,  $\beta_M$ , while the TRIA uses the  $\beta_{HL}$ . The flowchart of MRIA is shown in Figure 6.1. Initially, the design variables,  $\mathbf{d}^{(0)}$  and  $\mathbf{u}^{(0)}$ , are given. For the  $k^{th}$  iteration, the MPP sub-problem is solved first. The Eq. (6.11) is updated from the solution of the MPP and solved until solution convergence. The typical convergence criterion can be the quantitative evaluation of the absolute difference,  $|\mathbf{d}^{(k)} - \mathbf{d}^{(k+1)}|$ , or a weighted sum of  $|\mathbf{d}^{(k)} - \mathbf{d}^{(k+1)}|$  and  $|z(\mathbf{d}^{(k)}) - z(\mathbf{d}^{(k+1)})|$ . The iteration stops when the differential measure is less than a reasonably small value; or, it terminates when  $k$  is larger than the allowable iteration number.

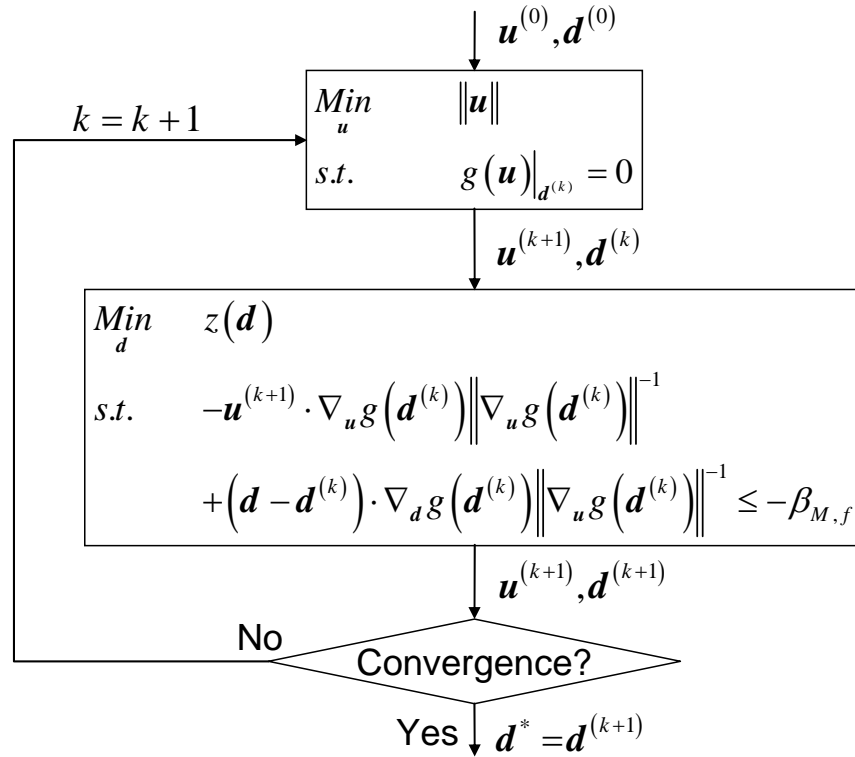


Figure 6.1. Flowchart of the MRIA.

## 6.2. Numerical Examples

Two different mathematical examples are utilized to exam the functionality of the proposed MRJA, including a simple linear problem and a famous benchmarking nonlinear problem. The comparisons between the TRIA and the MRJA with different starting points are studied in this session.

### 6.2.1. Example 6: Linear Mathematical Problem

A simple linear mathematical RBDO problem is solved in the first example. The problem has been studied and found unstable if the TRIA is used in [109]. The math problem is shown as follows

$$\begin{aligned}
 \text{Min}_{\mathbf{d}} \quad & z(\mathbf{d}) = d_1 + d_2 \\
 \text{s.t.} \quad & P_i[g_i(\mathbf{X}) > 0] \leq P_{f,i} \quad i = 1, 2 \\
 & 1 \leq d_j \leq 10 \quad j = 1, 2
 \end{aligned} \tag{6.17}$$

where

$$\begin{aligned}
 g_1(\mathbf{X}) &= -X_1 - 2X_2 + 10 \\
 g_2(\mathbf{X}) &= -2X_1 - X_2 + 10
 \end{aligned} \tag{6.18}$$

The allowable failure probabilities are defined as follows

$$\begin{aligned}
 P_{f,1} &= \Phi(-\beta_{f,1}) = \Phi(-2.054) = 2\% \\
 P_{f,2} &= \Phi(-\beta_{f,2}) = \Phi(-1.881) = 3\%
 \end{aligned} \tag{6.19}$$

The standard deviations of  $\mathbf{X}$  are both  $1/\sqrt{3}$ . If a feasible solution,  $[d_1^{(0)}, d_2^{(0)}] = [5, 5]$ , is used as the starting point, both the TRIA and MRJA arrive at the exactly same solution

as shown in Figure 6.2. This is because the definition of  $\beta_{HL}$  in Eq. (5.20) gives the same evaluation of Eq. (6.1) for a feasible solution.

However, if an infeasible solution,  $[d_1^{(0)}, d_2^{(0)}] = [2.5, 2.5]$ , is chosen as the starting point, the TRIA will use Eq. (5.20) to formulate an incorrect sub-problem and have difficulty to find the solution while the MRIA can reach the converged solution quickly. Fortunately, in this example, the TRIA can return to the feasible region gradually and eventually reaches the correct optimal solution. Figure 6.3 shows the iteration process of another different starting point,  $[2, 2]$ , using the TRIA. The iteration process converges at a wrong design of  $[1, 1]$ . The same starting point is used in the MRIA and the optimal solution is obtained in 2 iterations, shown in Figure 6.4.

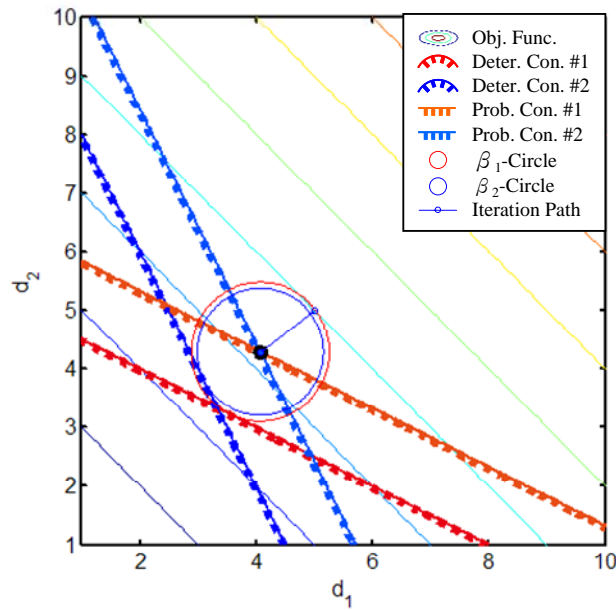


**Figure 6.2. Iteration Process of Example 6 Using MRIA with an Initial Design (5, 5).**

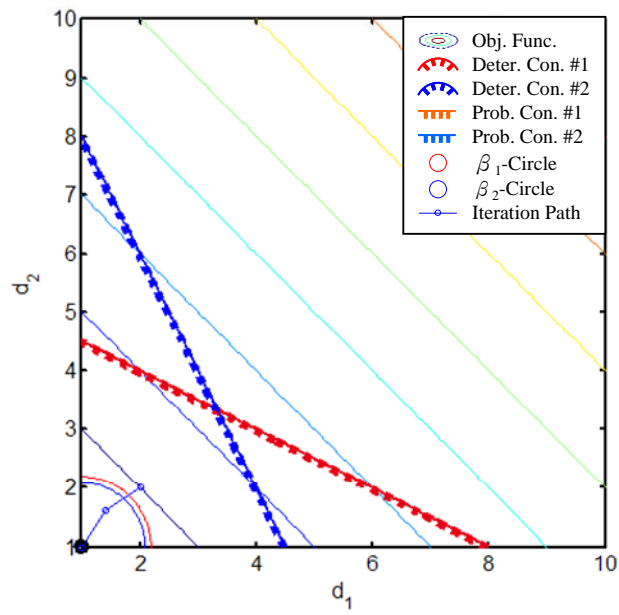


Figure 6.3. Iteration Process of Example 6 Using TRIA with an Initial Design (2, 2).

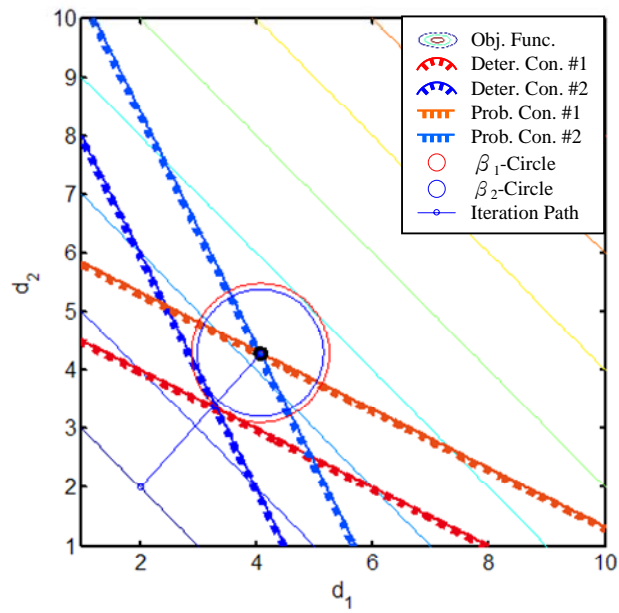


Figure 6.4. Iteration Process of Example 6 Using MRJA with an Initial Design (2, 2).

**Table 6.1. Comparison of TRIA and MRIA in Example 6.**

Initial Design	TRIA		MRIA	
	Converged	Efficient	Converged	Efficient
(5, 5)	Yes	Yes	Yes	Yes
(2.5, 2.5)	Yes	No*	Yes	Yes
(2, 2)	No	—	Yes	Yes

**Table 6.2. Comparison of TRIA and MRIA in Example 6.**

	Initial Design	Cost	Optimal Design	FC <sub>1</sub> <sup>†</sup>	FC <sub>2</sub> <sup>‡</sup>	FC <sub>T</sub> <sup>§</sup>	Iter. #	MCS of Con. #1	MCS of Con. #2
TRIA	(5, 5)	8.36	(4.0683, 4.2917)	61	63	124	2	1.995 %	3.001 %
MRIA	(5, 5)	8.36	(4.0683, 4.2917)	61	63	124	2	1.996 %	3.003 %
TRIA	(2.5, 2.5)	8.36	(4.0683, 4.2917)	285	441	726	12	2.006 %	3.006 %
MRIA	(2.5, 2.5)	8.36	(4.0683, 4.2917)	60	63	123	2	2.001 %	3.006 %
TRIA	(2, 2)	2	(1,1)	98	72	170	2	100 %	100 %
MRIA	(2, 2)	8.36	(4.0683, 4.2917)	74	63	137	2	1.993 %	2.995 %

The first example with three different starting points shows the TRIA suffers from inefficiency and convergence problems while the MRIA with the new reliability index,  $\beta_M$ , can arrive at the optimal solution quickly without any problem. Table 6.1 lists the resultant comparisons of the TRIA and the MRIA with different initial design points,

---

\* 10 more iterations than MRIA.

<sup>†</sup> FC<sub>1</sub> stands for the function calls of the MPP-searching sub-problems.

<sup>‡</sup> FC<sub>2</sub> stands for the function calls of the global loops.

<sup>§</sup> FC<sub>T</sub> stands for the sum of FC<sub>1</sub> and FC<sub>2</sub>.



which indicates that the TRIA may provide wrong optimal solutions or have inefficient optimization process when the infeasible starting points are used. The detailed optimization information with the three different starting points is listed in Table 6.2.

### 6.2.2. Example 7: Nonlinear Mathematical Problem

The second example is also a very well-known benchmark mathematical example that has been solved by many RBDO methods [102, 109, 122-126]. The problem has three probabilistic constraints as follows:

$$\begin{aligned} \underset{\mathbf{d}}{\text{Min}} \quad & z(\mathbf{d}) = d_1 + d_2 \\ \text{s.t.} \quad & P_i[g_i(\mathbf{X}) > 0] \leq P_f \quad i = 1 \dots 3 \\ & 0.1 \leq d_j \leq 10 \quad j = 1, 2 \end{aligned} \quad (6.20)$$

where

$$\begin{aligned} g_1(\mathbf{X}) &= 1 - \frac{X_1^2 X_2}{20} \\ g_2(\mathbf{X}) &= 1 - \frac{(X_1 + X_2 - 5)^2}{30} - \frac{(X_1 - X_2 - 12)^2}{120} \\ g_3(\mathbf{X}) &= 1 - \frac{80}{X_1^2 + 8X_2 + 5} \end{aligned} \quad (6.21)$$

The allowable failure probability is  $P_f = \Phi(-\beta_f) = \Phi(-3) = 0.13\%$ . The initial design  $[d_1^{(0)}, d_2^{(0)}] = [5, 5]$  and the standard deviations of  $\mathbf{X}$  are  $[\sigma_1, \sigma_2] = [0.3, 0.3]$ . The termination criteria in [122] are used where both the maximum iteration numbers of the MPP sub-problem and the global iteration loop cannot exceed 5. The optimization process stops when the relative difference of the objective function is less than 0.001.

This problem is firstly solved by both TRIA and MRIA, both method generated the same solution and have identical iteration history as shown in Figure 6.5. Totally 212 function calls (FCs) are needed for the MPP searching and the 216 FCs for the global optimization loop. Both methods reach the optimal solution in 4 iterations. The Monte Carlo Simulations (MCS) confirm the failure probabilities of all constraints are satisfactory.

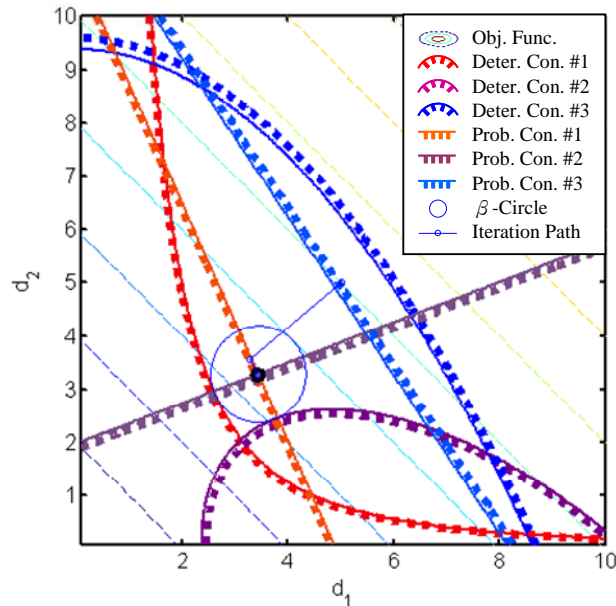


**Figure 6.5.** Iteration Process of Example 7 with an Initial Design (5, 5).

Then, a different starting point,  $[d_1^{(0)}, d_2^{(0)}] = [1.5, 3.5]$ , is used. This starting point is an infeasible solution and other conditions are kept as the same. As a result, the TRIA stops at the fifth iteration due to the termination criterion in [122] with 528 FCs. The final solution is located at  $[1.8832, 1.9397]$  and the cost function equals to 3.8229. The

MCS shows the failure probability for the first constraint almost equal to 99.989 %, which is totally not acceptable. The MRJA under the same settings achieves the convergence with only 427 FCs and 4 iterations. The optimal solution is  $[3.439, 3.2866]$ , which is the same as that from the previous initial design indicating the proposed algorithm provides the same optimal results despite the choice of initial design variables. The results using both methods are listed in Table 6.3 for comparison.

**Table 6.3. Results of Example 7.**

	<b>Initial Design</b>	<b>Cost</b>	<b>Optimal Design</b>	<b>FC<sub>1</sub><sup>*</sup></b>	<b>FC<sub>2</sub><sup>†</sup></b>	<b>FC<sub>T</sub><sup>‡</sup></b>	<b>Iter. #</b>	<b>M<sub>1</sub><sup>§</sup></b>	<b>M<sub>2</sub><sup>**</sup></b>	<b>M<sub>3</sub><sup>††</sup></b>
TRIA	(5,5)	6.7256	(3.439,3.2866)	212	216	428	4	0.145%	0.118%	0%
MRJA	(5,5)	6.7256	(3.439,3.3866)	212	216	428	4	0.148%	0.107%	0%
TRIA	(1.5,3.5)	3.8229	(1.8832,1.9397)	249	279	528	5	99.99%	0.113%	0%
MRJA	(1.5,3.5)	6.7256	(3.439,3.2866)	214	213	427	4	0.151%	0.109%	0%
TRIA	(1,4)	0.2	(0.1,0.1)	248	267	515	4	100%	0%	0.711%
MRJA	(1,4)	6.7256	(3.439,3.2866)	218	258	476	4	0.143%	0.113%	0%

Finally, the same problem with an infeasible starting point  $[d_1^{(0)}, d_2^{(0)}] = [1, 4]$  is solved by the traditional and the modified RIAs. The TRIA leads the design points to their lower bounds and the failure probability of the first constraint is found 100 %, as the

<sup>\*</sup> FC<sub>1</sub> stands for the function calls of the MPP-searching sub-problems.

<sup>†</sup> FC<sub>2</sub> stands for the function calls of the global loops.

<sup>‡</sup> FC<sub>T</sub> stands for the sum of FC<sub>1</sub> and FC<sub>2</sub>.

<sup>§</sup> M<sub>1</sub> stands for the MCS of the constraint #1.

<sup>\*\*</sup> M<sub>2</sub> stands for the MCS of the constraint #2.

<sup>††</sup> M<sub>3</sub> stands for the MCS of the constraint #3.

MRIA is capable of finding the correct optimal solution. Comparing all the optimal solutions with different initial design points in Table 6.4, the TRIA fails to provide a desired optimal solution when the infeasible starting points are utilized but the MRIA does not have such limitations and is able to find correct solutions despite the locations of the starting points.

**Table 6.4. Comparison of TRIA and MRIA in Example 7.**

Initial Design	TRIA		MRIA	
	Converged	Efficient	Converged	Efficient
(5, 5)	Yes	Yes	Yes	Yes
(1.5, 3.5)	No	—	Yes	Yes
(1, 4)	No	—	Yes	Yes

### **6.3. MRIA with Non-Normally Distributed Random Variables**

Not only can the MRIA be utilized to solve the typical RBDO problems with normally distributed random variables, but the methods to solve the ones with non-normally distributed random variables are investigated in this session. Famous non-normal distributions include lognormal, Weibull, Gumbel, and uniform distributions [121]. For simplicity, the random variable,  $\mathbf{X}$ , is now considered to be independent and lognormally distributed and its  $j^{th}$  component follows  $X_j \sim \text{LogN}(d_j, \sigma_j)$ . Using the transformation of  $\mathbf{X} = \exp \mathbf{Y}$ , an independent and normally distributed random variable,

$\mathbf{Y}$ , is obtained where its  $j^{th}$  component follows  $Y_j \sim N(d_{Y,j}, \sigma_{Y,j})$  and these two equations:

$$\sigma_{Y,j} = \sqrt{\ln \left( 1 + \frac{\sigma_j^2}{d_j^2} \right)} \quad (6.22)$$

$$d_{Y,j} = \ln d_j - \frac{1}{2} \sigma_{Y,j}^2 \quad (6.23)$$

Using  $\mathbf{Y} = \mathbf{d}_Y + \boldsymbol{\sigma}_Y \cdot \mathbf{U}$ , the transformation from the lognormal space to the standard normal space is established as  $\mathbf{X} = \exp(\mathbf{d}_Y + \boldsymbol{\sigma}_Y \cdot \mathbf{U})$ . The sub-problem in Eq. (5.19) is then solved to obtain the MPP and the modified reliability index is given by the Eq. (6.1). Using the Eqs. (6.7) and (6.8), the original probabilistic optimization problem with lognormally distributed random variables now becomes a solvable deterministic optimization problem as follows:

$$\begin{aligned} \underset{\mathbf{d}_Y}{Min} \quad & z(\mathbf{d}_Y) \\ \text{s.t.} \quad & -\beta_M(\mathbf{d}_Y) \leq -\beta_{M,f} \end{aligned} \quad (6.24)$$

Notice that the nonlinear conversion from the lognormal design space to the standard normal space includes design-dependent parameters in Eqs. (6.22) and (6.23). These two parameters should be updated prior to the MPP-searching sub-problem using the following two iterative schemes:

$$\sigma_{Y,j}^{(k)} = \sqrt{\ln \left[ 1 + \left( \sigma_j^{(k-1)} / d_j^{(k-1)} \right)^2 \right]} \quad (6.25)$$

$$d_{Y,j}^{(k)} = \ln d_j^{(k-1)} - 0.5 \left( \sigma_{Y,j}^{(k)} \right)^2 \quad (6.26)$$

These updating schemes do not cost any additional function calls of the performance constraints; however, the varying standard deviations do decrease the convergence efficiency of the MRIA. In the later session, the optimization processes of solving the mathematical problems with lognormally distributed random variables are demonstrated.

### **Nonlinear Mathematical Problem with Lognormally Distributed Random Variables**

The nonlinear mathematical problem is considered with lognormally distributed random variables. Besides the distributions of the random variables, the problem settings are the same as Eqs. (6.20) and (6.21) while the allowable failure probabilities, the initial designs, the standard deviations, and the termination criteria have no differences as well.

In the case of the feasible design  $[5,5]$ , the TRIA and the MRIA are identical where totally 5 iterations and 582 FCs are used to satisfy the convergence criteria. The iteration history is shown in Figure 6.6. The approximate probabilistic constraints are nonlinear due to transformation from the normal design space to the lognormal design space. The details about the optimal solutions are shown in Table 6.5. The MCS results show the failure probabilities of the optimal solutions are of acceptance. Compared with the optimization process with the normally distributed initial design  $[5,5]$ , more iterations and function calls are required to achieve the same termination criteria because of the updating scheme in Eqs. (27) and (28) for the lognormally distributed random variables.

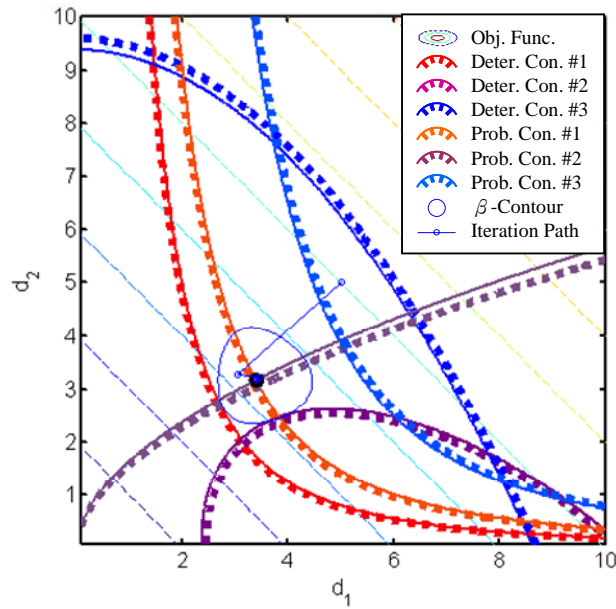


Figure 6.6. Iteration Process of Example 7 with the Lognormally Distributed Initial Design (5, 5).

Table 6.5. Results of Example 3.

	Initial Design	Cost	Optimal Design	$FC_1^*$	$FC_2^\dagger$	$FC_T^\ddagger$	Iter. #	$M_1^\S$	$M_2^{**}$	$M_3^{\dagger\dagger}$
TRIA	(5,5)	6.5854	(3.401,3.1844)	270	312	582	5	0.143%	0.114%	0%
MRIA	(5,5)	6.5854	(3.401,3.1844)	270	312	582	5	0.142%	0.106%	0%
TRIA	(1.5,3.5)	6.5948	(3.4362,3.1586)	300	270	570	5	0.103%	0.172%	0%
MRIA	(1.5,3.5)	6.5885	(3.4003,3.1882)	293	354	647	5	0.137%	0.102%	0%
TRIA	(1,4)	1.4902	(0.9615,0.5287)	311	279	610	5	100%	0.084%	0%
MRIA	(1,4)	6.5900	(3.4001,3.1889)	311	276	587	5	0.135%	0.099%	0%

\*  $FC_1$  stands for the function calls of the MPP-searching sub-problems.

†  $FC_2$  stands for the function calls of the global loops.

‡  $FC_T$  stands for the sum of  $FC_1$  and  $FC_2$ .

§  $M_1$  stands for the MCS of the constraint #1.

\*\*  $M_2$  stands for the MCS of the constraint #2.

††  $M_3$  stands for the MCS of the constraint #3.

In the other case of an infeasible design point  $[1.5, 3.5]$ , both the TRIA and the MRIA can find optimal solutions with acceptable failure probabilities. However, when an infeasible design point  $[1, 4]$  is used, the TRIA leads the optimal solution to  $[0.9615, 0.5287]$  where the failure property of the first constraint is 100 %. The MRIA still can find the optimal solution with acceptable failure probabilities. Table 6.6 shows that the unstableness and inconsistency in which the TRIA finds an acceptable solution for one of the case with the infeasible starting point  $[1.5, 3.5]$  but leads to 100 % of failure probability for the other one with the starting point  $[1, 4]$ . Unlike the unstableness in the TRIA, the MRIA provides the optimal solutions with acceptable failure probabilities in spite of the feasibility of the starting point.

**Table 6.6. Comparison of TRIA and MRIA in Example 3.**

Initial Design	TRIA		MRIA	
	Converged	Efficient	Converged	Efficient
(5, 5)	Yes	Yes	Yes	Yes
(1.5, 3.5)	Accepted*	Yes	Yes	Yes
(1, 4)	No	—	Yes	Yes

---

\* 30 % of violation of the desired failure probability.



#### **6.4. Conclusion and Remarks**

The TRIA suffers from inefficiency and convergence problems. Since the convergence problems from numerical singularities associated with very small standard deviations are not very common in engineering practice, the focus of this paper is on the convergence problems from the incorrect evaluations of the failure probabilities which may happen at the initial design as well as during the optimization iteration. The convergence problem of the latter kind in the TRIA is from the definition of the traditional reliability index. The original reliability index is defined as the shortest distance between the origin and the failure region in the normalized space. If any design is within the failure region, this definition of reliability index becomes invalid. However, the MPP sub-optimization problem of the RIA will still return a MPP “solution”. Consequently, the TRIA may generate erratic solutions.

To correct this problem, a new definition of the reliability index is proposed to correct this problem and a Modified Reliability Index Approach using the new definition is developed. Numerical examples using both the TRIA and the MRIA are compared and discussed. The results show that the TRIA may provide incorrect constraint approximations and lead to the unstableness of the optimization process, while the MRIA can always reach the optimal solution efficiently. Furthermore, the MRIA is also found to be capable of solving RBDO problems with different distributions of random variables using the transformation from the original space to the standard normal space. With the updating schemes of the mapping parameters, the MRIA does require more computational efforts but is able to converge at the correct optimal solution.

The development of the MRIA is very important in the design optimization of the thermal system because the design uncertainties exist in the design variables of the operating conditions. The MRIA is capable of evaluating the failure probabilities in spite of that the designs are feasible or they violate the performance constraints in the optimization process. Another important contribution of the MRIA is that it can solve the RBDO problems of the thermal systems with not only the normally distributed random variables but the non-normally distributed ones. In the next chapter, the proposed MRIA is applied to solve the optimization problems of the thermal systems with the design uncertainties.

## **Chapter 7.**

### **RBDO of the CVD Process**

#### ***7.1. Introduction***

From Chapter 2 to Chapter 4, the simulations and the response surface models of the CVD process have been discussed. The optimization formulations using the response surface models of the deposition rate and the uniformity of the thin films have been studied to find the optimal operating conditions of the CVD process. However, the proposed optimization problems lack for the considerations of the design uncertainties and lead to high risks of the violations of the performance constraints. The most significant impacts of the design uncertainties occur at the design variables, the inlet velocity and the susceptor temperature. Only around two percents of the deviations in the design variables cause more than forty percents of the failure probabilities.

In Chapter 5, the RBDO algorithms have been introduced to solve probabilistic optimization problems. The Reliability Index Approach evaluates the failure probabilities of the performance constraints in terms of the Hasofer-Lind Reliability Index and solves the RBDO problems by constraining those failure probabilities under certain allowable level. Chapter 6 reveals the convergence problem of the TRIA at infeasible design points, which may produce incorrect optimal solutions with unacceptable probabilities of system failures or may have inefficient optimization process. The Modified Reliability Index Approach is proposed with a new definition of the

reliability index. The MRIA is much efficient than the TRIA because it is capable of evaluating the failure probabilities correctly despite of the locations of the design points.

In this chapter, the optimization problems in Chapter 4 are to be solved by the proposed MRIA with the considerations of the design uncertainties in the design variables. Two different distributions of the random variables are studied: session 7.2 shows the RBDO problems of the CVD process with the normally distributed random variables while session 7.3 demonstrates the ones with the lognormally distributed random variables. Session 7.4 includes the detailed information about the obtained optimal solutions and the corresponding failure probabilities evaluated by the Monte Carlo Simulations.

## ***7.2. RBDO Problems of the CVD Process with Normally Distributed Random Variables***

The five optimization formulations in session 4.2 are revisited. With the considerations of the uncertainties in the inlet velocity and the susceptor temperature, probabilistic optimization problems are formulated. In this session, the random variables are assumed mutually independent and normally distributed. The probabilistic constraints of the thin-film performances will be converted to the solvable deterministic formulations in terms of the modified reliability index. The MRIA will be utilized to solve those probabilistic optimization problems and the MCS will be used to verify the failure probabilities of the optimal solutions.

### 7.2.1. Example 1: Maximizing the PWA

First, the optimization problem in Eq. (4.1) is studied. Considering the standard deviations of 0.02 m/s and 20 K for the mutually independent normally distributed random variables,  $V$  and  $T$ , respectively, the probabilistic optimization formulation is given by

$$\begin{aligned}
 & \underset{V, T}{Max} \quad \text{PWA} \\
 & s.t. \quad P[\text{RMS} > \text{RMS}_U] \leq 0.13\% \\
 & \quad \quad P[\text{KUR} > \text{KUR}_U] \leq 0.13\% \\
 & \quad \quad V_L \leq V \leq V_U \\
 & \quad \quad T_L \leq T \leq T_U
 \end{aligned} \tag{7.1}$$

where the acceptable limits of the RMS and the KUR remain the same as the previous conditions, as well as the bounds of the design variables. The same response surface models by the 25-point RBFs are utilized. The allowable failure probabilities are both 0.13 % following the concept of the three-sigma criterion. Due to the nonlinearities of the uniformity constraints and the concave feasible domain, the global optimal solution is obtained by multiple starting design points.

Using the optimization process of the MRIA shown in Figure 6.1, the probabilistic constraints in Eq. (7.1) are converted into linear approximate functions in terms of the MPPs. Figure 7.1 illustrates the approximate probabilistic constraints at the convergence of the optimization process by the MRIA, as well as the optimal solution,  $V^* = 0.74$  m/s and  $T^* = 1068$  K. The blue contour in the figure highlights the 99.87 % of the probability distribution of the optimal solution, which is tangent to the first deterministic constraint. MCS results confirmed the failure probabilities at the optimal

solution. The failure probability of the first constraint improvingly decreases from 43.03 % to 0.107 % and meets the allowable level, 0.13 %, while the original PWA only slightly decreases from 93.78 % to a more conservative PWA, 93.6 %.

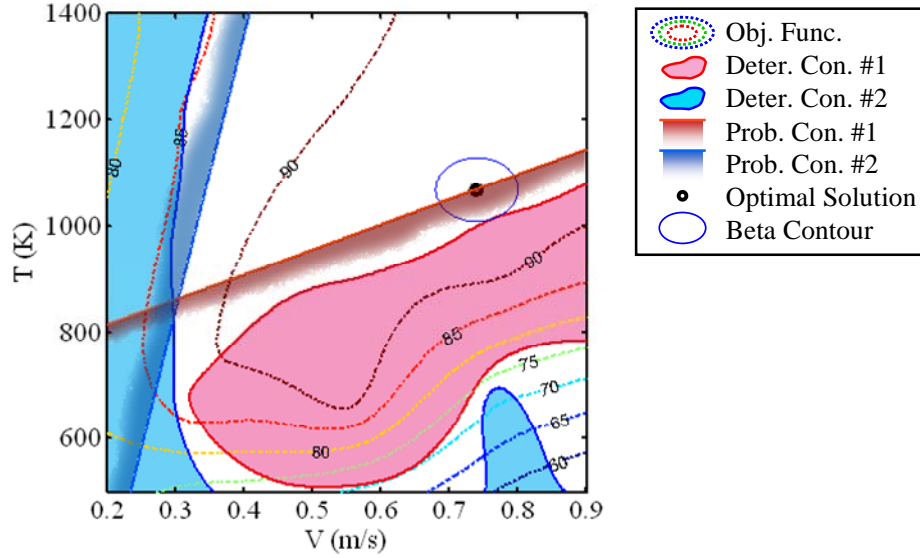


**Figure 7.1. Optimal Solution of Maximizing the PWA with Normally Distributed Random Variables.**

### 7.2.2. Example 2: Maximizing the MDR

The second example is to maximize the deposition rate subject to the probabilistic constraints of the RMS and the KUR with the normally distributed random variables.

The probabilistic optimization formulation is shown as follows:

$$\begin{aligned}
 & \underset{V, T}{Max} \quad MDR \\
 & s.t. \quad P[\text{RMS} > \text{RMS}_U] \leq 0.13\% \\
 & \quad \quad P[\text{KUR} > \text{KUR}_U] \leq 0.13\% \\
 & \quad \quad V_L \leq V \leq V_U \\
 & \quad \quad T_L \leq T \leq T_U
 \end{aligned} \tag{7.2}$$

where the standard deviations and the allowable failure probabilities are under the same conditions as the previous example in session 7.2.1. The optimal solution,  $V^* = 0.9$  m/s and  $T^* = 574$  K, and the corresponding probabilistic constraints are shown in Figure 7.2. The MCS results verify that the failure probabilities accept the desired level. As a result, the optimal susceptor temperature needs to increase from 500 K to 574 K to have acceptable probabilities of system failures, while the optimal MDR decreases 4 % from the original  $2.354 \times 10^{-4}$  kg/m<sup>2</sup>s to  $2.252 \times 10^{-4}$  kg/m<sup>2</sup>s.

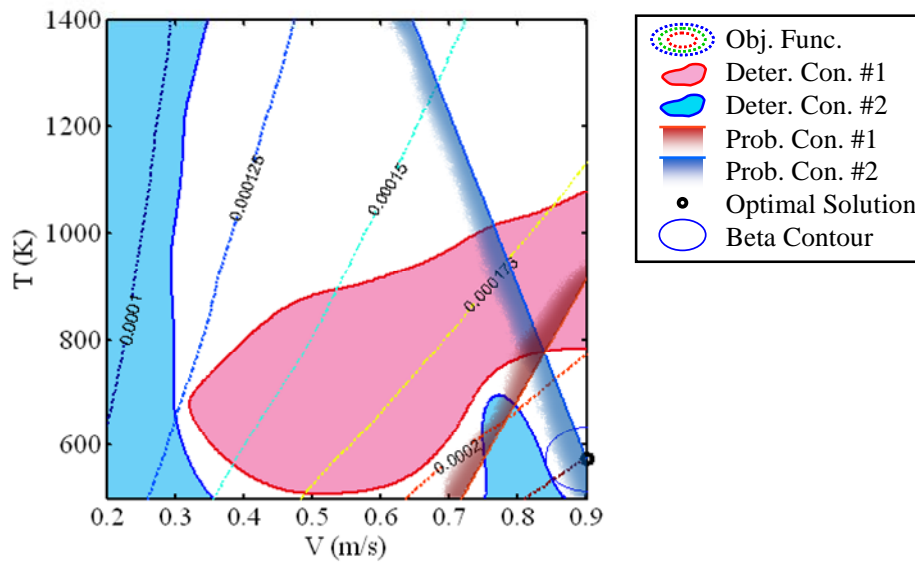


**Figure 7.2. Optimal Solution of Maximizing the MDR with Normally Distributed Random Variables.**

### 7.2.3. Example 3: A Multi-Objective Formulation

The third formulation is the multi-objective function considering the maximization of the PWA and the MDR simultaneously with the same normally

distributed random variables. The same probabilistic constraints are considered and the RBDO problem is given by

$$\begin{aligned}
 & \underset{V, T}{\text{Max}} \quad \frac{\text{PWA}}{\text{PWA}_m} + \frac{\text{MDR}}{\text{MDR}_m} \\
 & \text{s.t.} \quad P[\text{RMS} > \text{RMS}_U] \leq 0.13\% \\
 & \quad \quad P[\text{KUR} > \text{KUR}_U] \leq 0.13\% \\
 & \quad \quad V_L \leq V \leq V_U \\
 & \quad \quad T_L \leq T \leq T_U
 \end{aligned} \tag{7.3}$$

where the two disciplines, the PWA and the MDR, are normalized by their maximum quantities. Using the MRIA, the probabilistic constraints are obtained and the optimal solution is found at  $V^* = 0.9$  m/s and  $T^* = 1148$  K, shown in Figure 7.3. The first approximate probabilistic constraint is active and leads the design point to the optimality with acceptable failure probabilities, which is verified by the MCS results. More detailed information about the optimal solutions is discussed in the latter session.

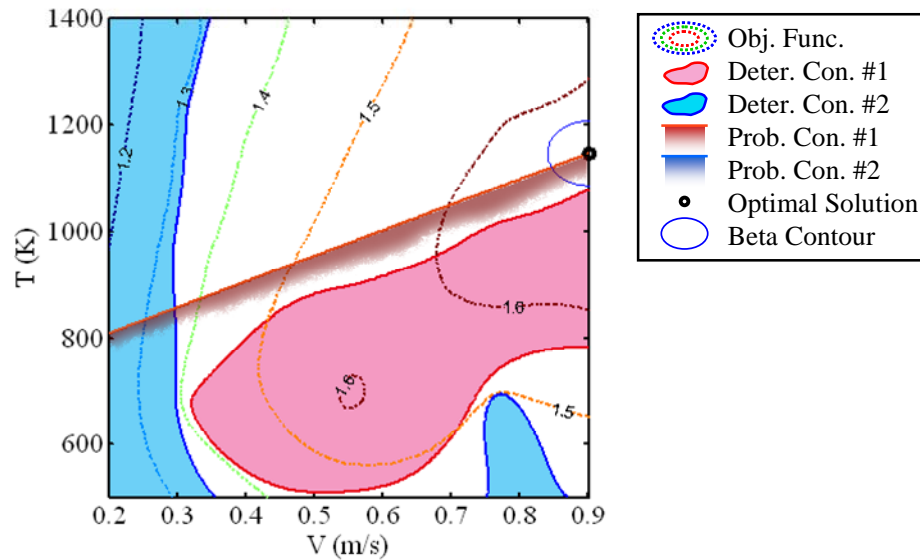


**Figure 7.3. Optimal Solution of the Multi-Objective Formulation with Normally Distributed Random Variables.**



#### 7.2.4. Example 4: Maximizing the PWA Subject to Constraint of Deposition Rate

The next example considers the objective of maximizing the PWA subject to the probabilistic constraints of the uniformity factors and the deposition rate, which is given by

$$\begin{aligned}
 & \underset{V, T}{Max} \quad \text{PWA} \\
 & s.t. \quad P[\text{RMS} > \text{RMS}_U] \leq 0.13\% \\
 & \quad \quad P[\text{KUR} > \text{KUR}_U] \leq 0.13\% \\
 & \quad \quad P[\text{MDR}_L > \text{MDR}] \leq 0.13\% \\
 & \quad \quad V_L \leq V \leq V_U \\
 & \quad \quad T_L \leq T \leq T_U
 \end{aligned} \tag{7.4}$$

The bounds of the performance responses and the design domain remain the same as previous discussion, as well as the probability distribution and the allowable failure probabilities. Figure 7.3 shows the optimal solution and the probabilistic constraints. The optimal solution is found the same as the example in session 7.2.1 because the MDR constraint is not active with the consideration of the design uncertainties, while the MCS results confirm zero failure probability for the MDR constraint. The MCS results also verify the acceptance of the failure probabilities of the other constraints.

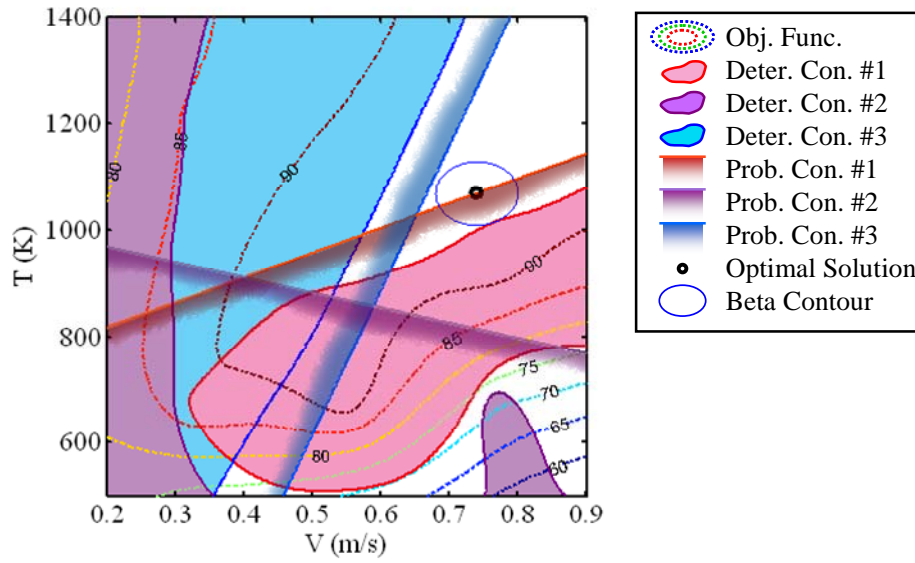


**Figure 7.4. Optimal Solution of Maximizing the PWA Subject to the MDR Constraint with Normally Distributed Random Variables.**

### 7.2.5. Example 5: Maximizing the MDR Subject to Constraint of Working Area

Finally, the MDR is maximized subject to the consideration of the uniformity constraints and the working area with the normally distributed random variables, which is shown as follows:

$$\begin{aligned}
 & \underset{V, T}{Max} && \text{MDR} \\
 & s.t. && P[\text{RMS} > \text{RMS}_U] \leq 0.13\% \\
 & && P[\text{KUR} > \text{KUR}_U] \leq 0.13\% \\
 & && P[\text{PWA}_L > \text{PWA}] \leq 0.13\% \\
 & && V_L \leq V \leq V_U \\
 & && T_L \leq T \leq T_U
 \end{aligned} \tag{7.5}$$

The approximate probabilistic constraints are obtained by the MRJA and the optimal solution is shown in Figure 7.5. With the additional consideration of the PWA constraint,

a higher optimal susceptor temperature,  $T^* = 1148$  K, than the example in session 7.2.2 is needed to produce thin films with acceptable working area. Furthermore, the temperature is slightly higher than the solution in session 4.2.2, 1078 K, to satisfy the allowable failure probabilities, which is confirmed by the MCS results. More detailed information about the optimal solutions is shown in the latter session.

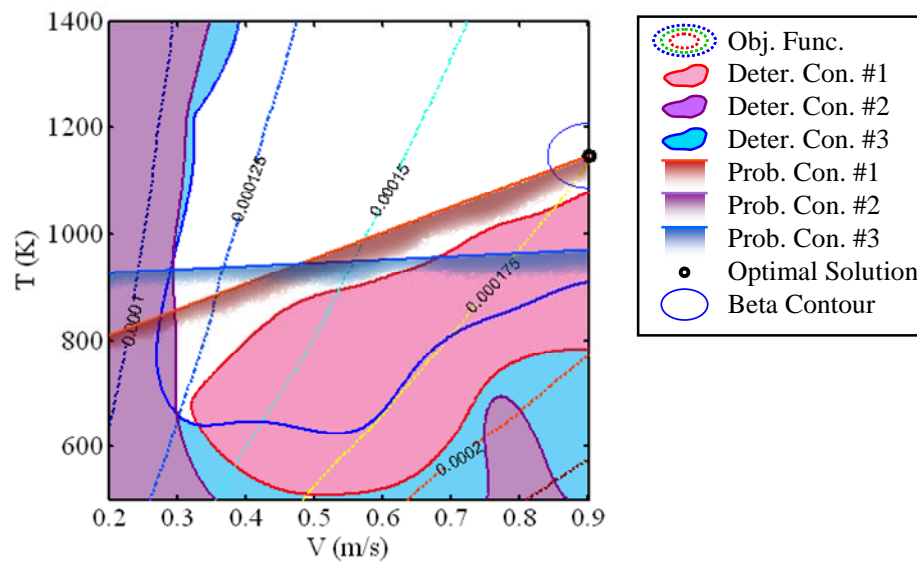


Figure 7.5. Optimal Solution of Maximizing the MDR Subject to the PWA Constraint with Normally Distributed Random Variables.

### 7.3. RBDO Problems of the CVD Process with Lognormally

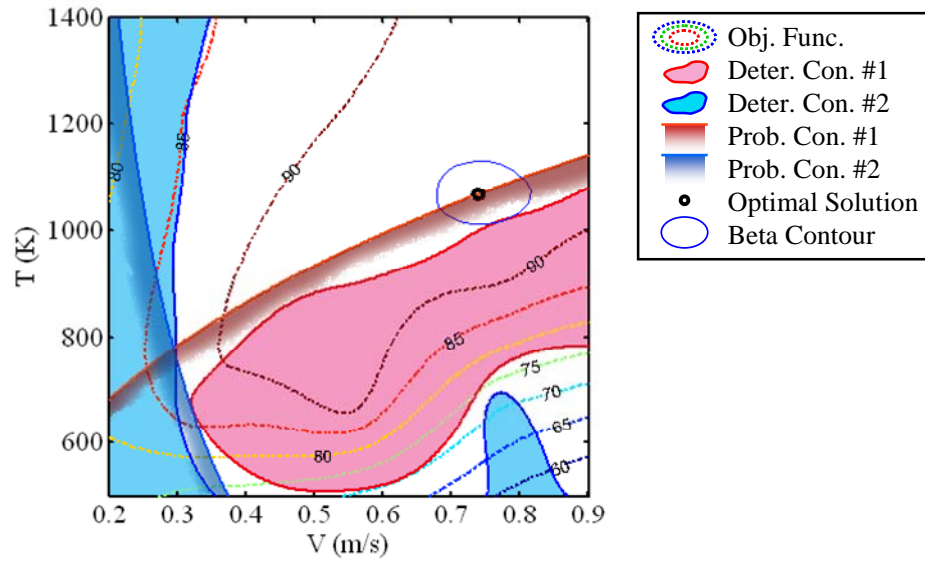
#### *Distributed Random Variables*

The optimization problems of the CVD process with normally distributed random variables have been studied in the previous session. The optimal solutions are obtained in terms of finding the MPPs in the standard normal space, converting the probabilistic constraints into solvable formulations by the definition of the modified reliability index,

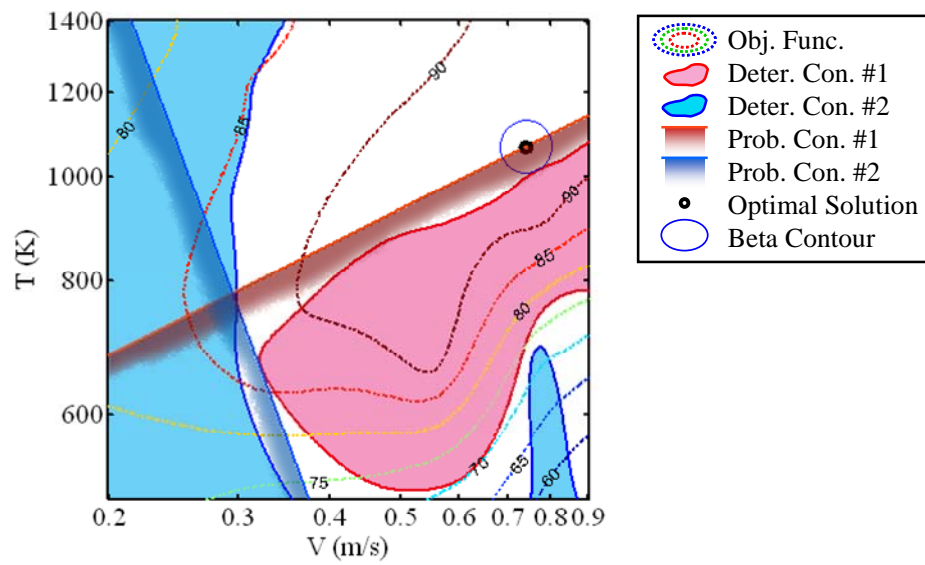
and solving the problems iteratively. For non-normally distributed random variables, the design domain is firstly converted to the normal design space and the MRIA is then utilized to solve the RBDO problem with varying standard deviations. In this session, the five optimization problems with lognormally distributed random variables are studied and solved the proposed MRIA strategy in session 6.3.

### 7.3.1. Example 1: Maximizing the PWA

Considering the probabilistic optimization formulation in Eq. (7.1) with lognormally distributed random variables, the standard deviations of the inlet velocity and the susceptor temperature in the lognormal design space are 0.02 m/s and 20 K respectively. After the conversion from the lognormal space to the normal space, the standard deviations vary with the location of the design point and follow the Eq. (6.22). Figure 7.6 (a) demonstrates the optimization problem of maximizing the PWA in the lognormal design space, where the distribution of the design point is highlighted by the blue non-symmetric contour. The converted design domain in the normal space is shown in the Figure 7.6 (b) where the distribution of random variable is shown by the blue symmetric contour. During the iteration process, the size of the distribution contour changes with variations of the standard deviations. The probabilistic constraints are linearly approximated according to the updated standard deviations in the normal space and they are therefore nonlinear the original design space. Using the MRIA and the updating scheme of the standard deviations in session 6.3, the optimal solution is obtained at  $V^* = 0.74$  m/s and  $T^* = 1068$  K. The MCS results show acceptable failure probabilities at the optimal solution.



(a)



(b)

**Figure 7.6. Optimal Solution of Maximizing the PWA with Lognormally Distributed Random Variables.**

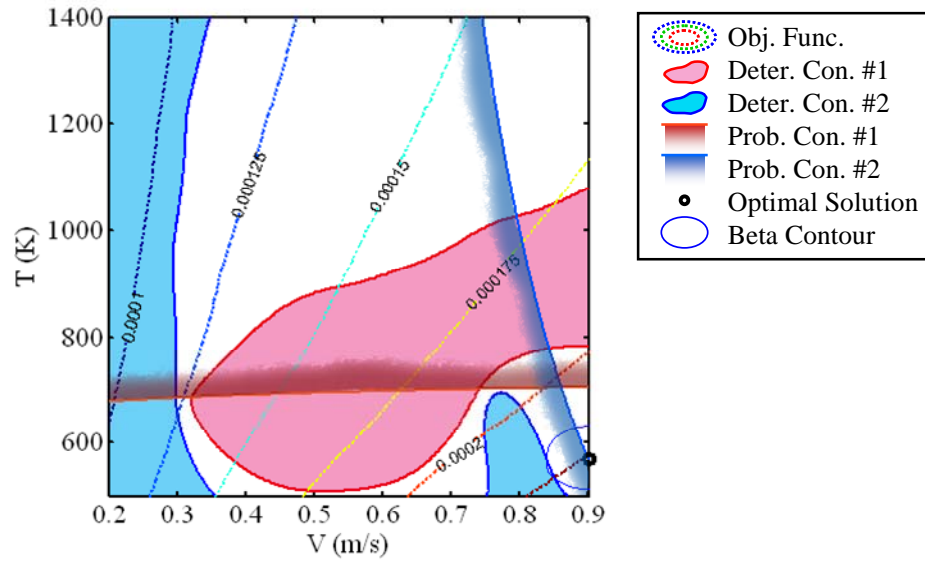
**(a) Visualization in the Lognormal Design Space, and (b) Visualization in the Normal Design Space.**

### 7.3.2. Example 2: Maximizing the MDR

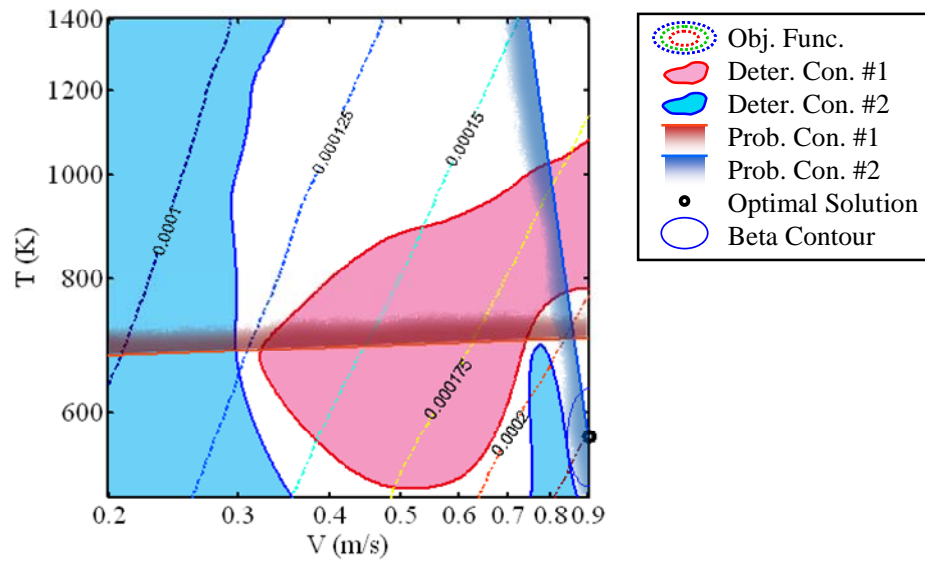
The second optimization formulation is given in Eq. (7.2) with the considerations of the lognormally distributed random variables. The standard deviations in the lognormal space remain the same as the previous discussion. To solve the RBDO problem by the MRIA, the design space is converted to the normal space resulting in varying standard deviations. The iterative updating scheme is utilized to adjust the standard deviations. Figure 7.7 (a) demonstrates the obtained optimal solution in the original lognormal space, while the corresponding configuration in the normal space is shown in Figure 7.7 (b). The second probabilistic constraint is active and the optimal solution is located at  $V^* = 0.9$  m/s and  $T^* = 568$  K, which is different from the solution in session 7.2.2. The MCS results confirm the correctness of the optimal design with lognormal distribution. This implies the necessity of the conversion to the normal space and the updating of the standard deviations for solving the RBDO problems with non-normally distributed random variables.

### 7.3.3. Example 3: A Multi-Objective Formulation

The third optimization problem is the multi-objective formulation in Eq. (7.3). Considering the lognormally distributed random variables and the same conditions as described earlier, the optimal solution is obtained by the MRIA with the updating standard deviations in the normal space. Figure 7.8 illustrates the optimal solution in the lognormal space and the conversion to the normal space. The first probabilistic performance constraint is active and the failure probability is satisfied, verified by MCS.



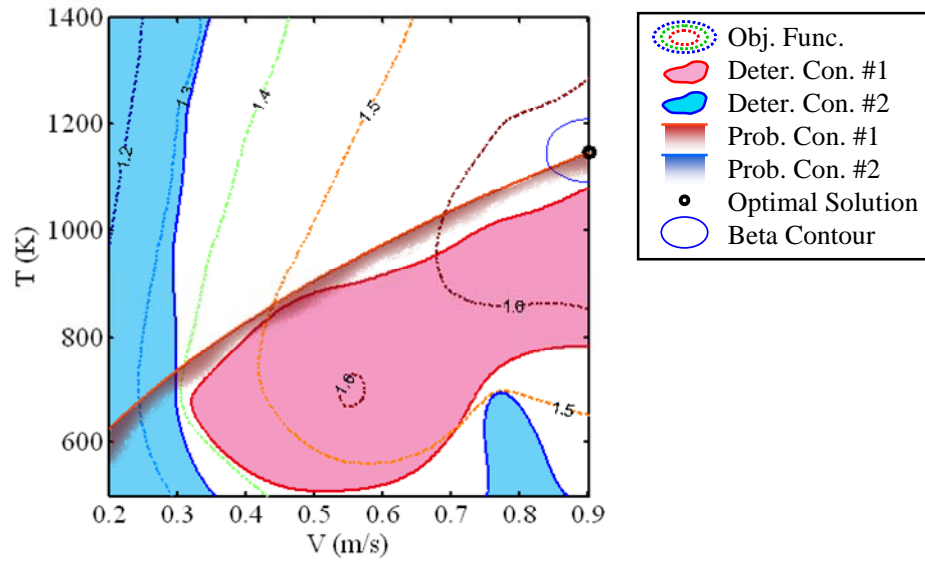
(a)



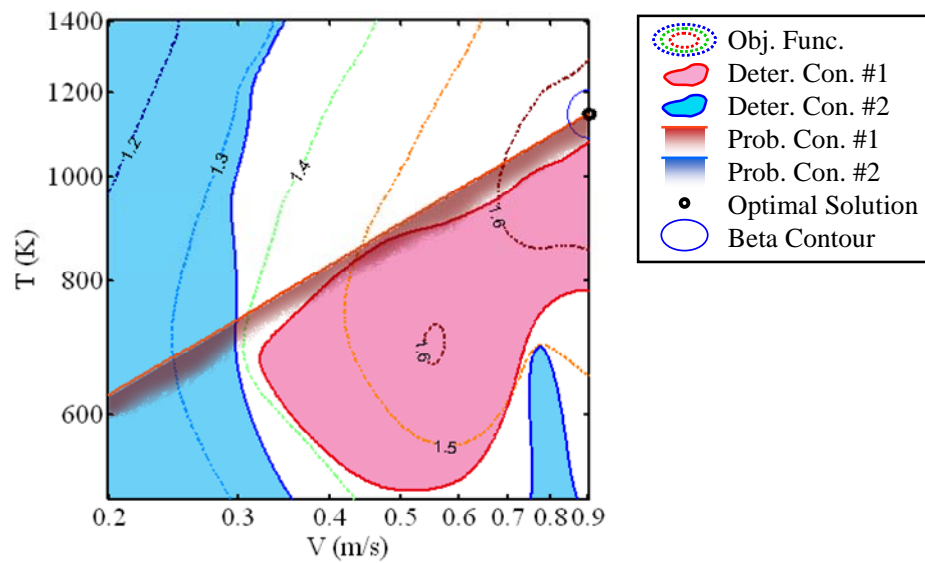
(b)

**Figure 7.7. Optimal Solution of Maximizing the MDR with Lognormally Distributed Random Variables.**

**(a) Visualization in the Lognormal Design Space, and (b) Visualization in the Normal Design Space.**



(a)



(b)

**Figure 7.8. Optimal Solution of the Multi-Objective Formulation with Lognormally Distributed Random Variables.**

**(a) Visualization in the Lognormal Design Space, and (b) Visualization in the Normal Design Space.**

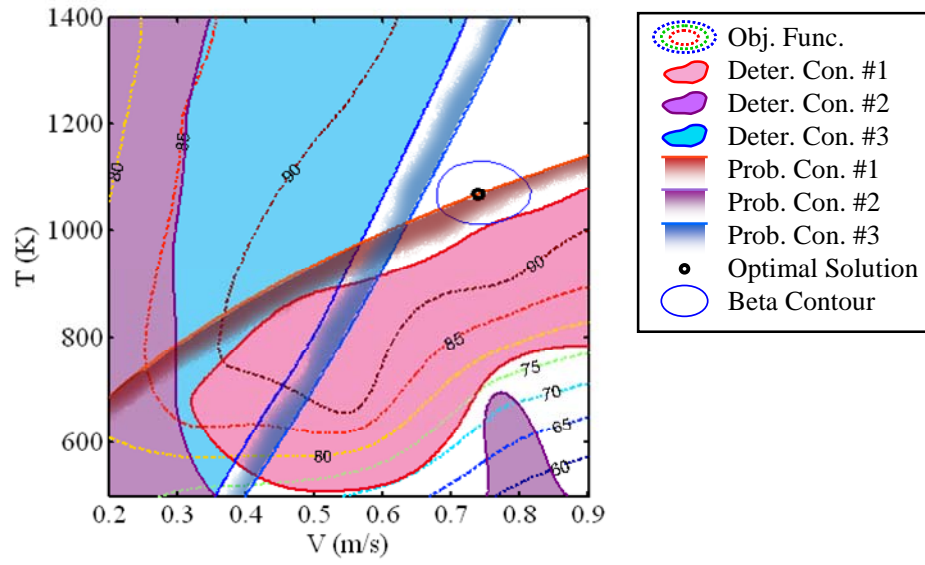


#### **7.3.4. Example 4: Maximizing the PWA Subject to Constraint of Deposition Rate**

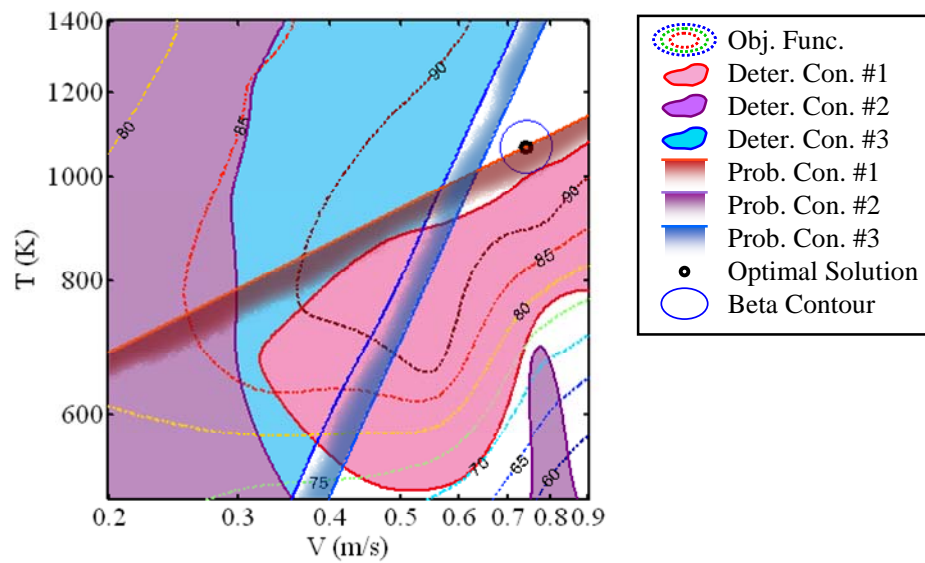
The forth example considers the maximization of the working area subject to the constraints of the uniformity and the deposition rate with the lognormally distributed random variables. The RBDO problem is formulated in Eq. (7.4) and the same considerations about the failure probabilities continue. Using the proposed MRIA, the optimal solution is obtained, shown in Figure 7.9, and verified by the MCS.

#### **7.3.5. Example 5: Maximizing the MDR Subject to Constraint of Working Area**

The final example is to maximize the MDR subject to the constraints of the RMS, the KUR, and the PWA with the lognormally distributed inlet velocity and susceptor temperature. The problem formulation is shown in Eq. (7.5) and it is solved by the proposed method discussed in session 6.3. Figure 7.10 shows the optimal solution in the lognormal space, as well as the corresponding situation in the normal space. More details and comparisons are included in the next session.



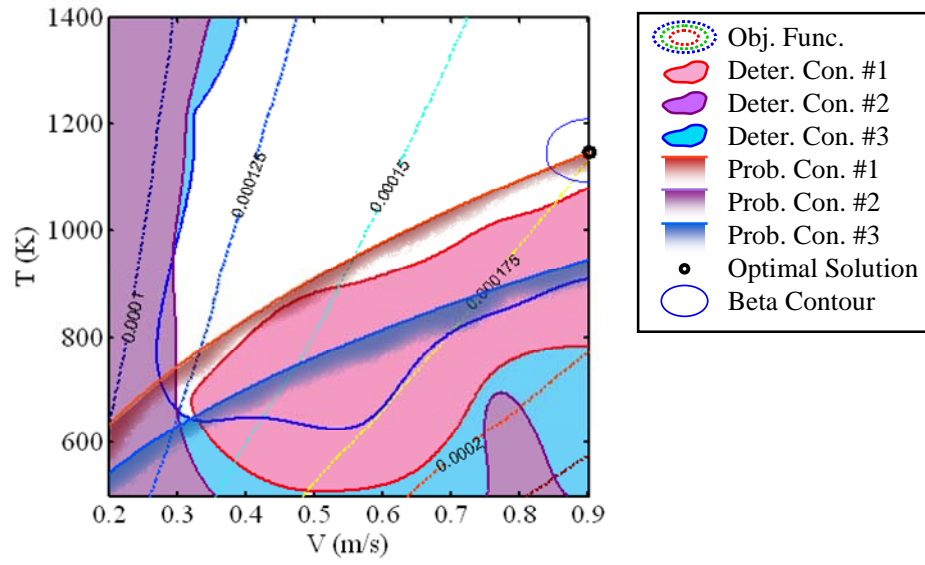
(a)



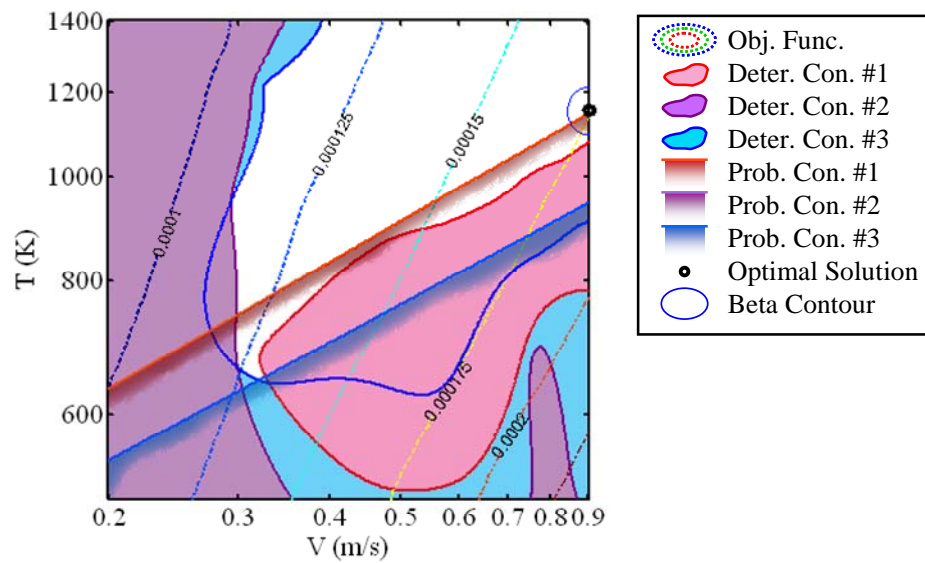
(b)

**Figure 7.9. Optimal Solution of Maximizing the PWA Subject to the MDR Constraint with Lognormally Distributed Random Variables.**

**(a) Visualization in the Lognormal Design Space, and (b) Visualization in the Normal Design Space.**



(a)



(b)

**Figure 7.10. Optimal Solution of Maximizing the MDR Subject to the PWA Constraint with Lognormally Distributed Random Variables.**

**(a) Visualization in the Lognormal Design Space, and (b) Visualization in the Normal Design Space.**

## 7.4. Results

The optimization problems of the CVD process with two different kinds of design uncertainties have been studied, including the normally and the lognormally distributed random variables. For the normally distributed random variables, the RBDO problem is solved directly by the MRIA. On the other hand, the conversion to the normal space and the updating scheme of the varying standard deviations are necessary for non-normally distributed random variables.

The details about the optimal designs with design uncertainties are listed in Table 7.1. Back in the session 4.3, the MCS results have shown that the optimal solutions for the deterministic optimization formulations suffer from high probabilities of the system failures even though they are theoretically the best operating conditions for the CVD process without the design uncertainties. After considering the RBDO formulations and solving them by the MRIA, more conservative operating conditions are found and the failure probabilities of all the constraints are satisfied within certain allowable range. Take the first optimization formulation as an example, the failure probabilities of the first uniformity constraints have greatly reduced from 43.03 % to 0.11 % for the normally distributed random variables; and from 43.13 % to 0.12 % for the lognormally distributed ones, using the comparison between Table 4.2 and Table 7.1. However, the objective functions, the PWA, only slightly decrease from 93.78 % to 93.60 % and 93.61 % for the normally and the lognormally distributed random variables respectively, using the comparison between Table 4.1 and Table 7.1.

**Table 7.1. The Optimal Solutions, the Corresponding Responses, and the Monte Carlo Simulation Results for Examples 1 to 5 with the Normally and the Lognormally Distributed Random Variables.**

Ex. #	Distribution	Optimal Solution	PWA	MDR	RMS	KUR	$M_1^*$	$M_2^\dagger$	$M_3^\ddagger$
1	Normal	(0.74,1068)	93.60	1.643E-4	1.231E-6	1.656	0.107%	0%	—
	Lognormal	(0.74,1068)	93.61	1.643E-4	1.232E-6	1.656	0.122%	0%	—
2	Normal	(0.9,574)	60.05	2.252E-4	1.060E-6	2.595	0%	0.141%	—
	Lognormal	(0.9,568)	59.70	2.261E-4	1.054E-6	2.60	0%	0.154%	—
3	Normal	(0.9,1148)	91.04	1.744E-4	1.230E-6	1.69	0.128%	0%	—
	Lognormal	(0.9,1147)	91.05	1.744E-4	1.232E-6	1.69	0.122%	0%	—
4	Normal	(0.74,1069)	93.60	1.643E-4	1.230E-6	1.66	0.112%	0%	0%
	Lognormal	(0.74,1067)	93.61	1.644E-4	1.233E-6	1.66	0.118%	0%	0%
5	Normal	(0.9,1148)	91.04	1.744E-4	1.230E-6	1.69	0.120%	0%	0%
	Lognormal	(0.9,1147)	91.05	1.744E-4	1.232E-6	1.69	0.110%	0%	0%

## 7.5. Conclusion and Remarks

The MRIA has been successfully applied to solve the RBDO problems of the CVD process with both normally and lognormally distributed random variables, the inlet velocity and the susceptor temperature. For normally distributed variables, the MPPs are firstly found in the standard normal space and then utilized to approximate the probabilistic constraints. Those approximate probabilistic constraints are iteratively updated by the latest MPPs with respect to the mean of the random variables. The global

---

\*  $M_1$  stands for the MCS of the constraint #1.

†  $M_2$  stands for the MCS of the constraint #2.

‡  $M_3$  stands for the MCS of the constraint #3.

optimal operating conditions are found with the updated probabilistic constraints and the multiple starting points due to the concave feasible domains. For the non-normally distributed random variables, the original design space is converted to the normal space and the variant standard deviations are iteratively updated before the RBDO problems are solved by the MRIA. Numerical examples show that the MRIA is capable of solving the RBDO problems of the CVD process with lognormally distributed random variables. The MCS results are utilized to verify the acceptance of the failure probabilities. All the optimal solutions satisfy the allowable probabilities of the system failures with only slight decrement on the optimality.

Similarly, the proposed MRIA can be utilized to solve the RBDO problems of other thermal systems. For the consideration of the normally distributed random variables in the thermal systems, the designer needs to measure the standard deviations so that the design mean can be transformed to the standard normal space and the MPPs can be found for the approximation of the probabilistic constraints. On the other hand, the standard deviations are expected to be updated iteratively for the non-normally distributed random variables. The results of the numerical examples in this chapter have shown that the MRIA is capable of finding the optimal solutions of the thermal systems with the failure probabilities lower than the allowable limits.

## Chapter 8.

### Conclusion and Future Work

#### **8.1. Summary**

A systematic strategy to parametric model and optimize of the thermal systems with design uncertainties has been proposed in this research work. The CVD has been chosen as an example, where the inlet velocity and the susceptor temperature are the design variables. The CVD process is simulated and the responses, the PWA, the MDR, the RMS, and the KUR, are utilized to represent the productivity and the uniformity of the thin-film deposition of silicon from silane. The Radial Basis Function is utilized to model those responses. Then, the response surface models are used to formulate the optimization problems for finding the better operating conditions. The Modified Reliability Index Approach is introduced to solve those optimization problems with both the normally and non-normally distributed random variables. In the optimization process of the MRJA, the MPPs are found and utilized to formulate the approximate probabilistic constraints. The optimal solutions for found and the failure probabilities are of acceptance. As a result, not only the proposed strategy can be utilized to model and optimize the CVD process with design uncertainties, but also it can be applied to other thermal systems.

The proposed strategy to simulate the thin-film growth of silicon, parametrically model the responses of the deposition, and optimize the operating condition with

uncertainties is also very useful for other thin-film fabrications in semiconductors. One of the examples is the spin-coating process of polymers on the silicon wafer, which is a critical post-process of photolithography [127]. The design variables include the velocity of the spin-coater, the position of the silicon wafer, and the amount of the applied polymers. The responses include the thickness and the uniformity of the polymer thin-film, which can be modeled by the Radial Basis Functions in terms of experiment data. The proposed method can be utilized to find the optimal operating conditions for the desired thickness with the allowable uniformity in terms of the root mean square and the surface kurtosis. In the optimization process of the thin-film growth, the design uncertainties in the design variables, including the spin velocity and the position of the wafer, should be considered. The Modified Reliability Index Approach provides the evaluations of the failure probabilities and generates the approximate probabilistic constraints. The optimization problems with design uncertainties can then be solved and the optimal operating condition can be obtained. Similarly, the proposed strategy can be directly applied to any other thin-film growth of the thermal systems.

Besides the thermal systems with thin-film growth, the proposed method can also be applied to other thermal systems, such as the cooling design of the heat sink on the CPU chip of a computer. In the example of the cooling design of the heat sink in Figure 1.1 (c), the fluid mechanics and heat transfer is different from the CVD process. Either experiments or numerical simulations should be designed with the different hardware parameters or operating conditions. The hardware parameters include the dimension of the heat sink, the dimension of the fin, the orientation of the heat sink, and



the working space of the desktop case; on the other hand, the operating conditions include the temperature of the CPU chip and the velocity of the cooling fan in the case. Collecting the data from the experiments/simulations, some responses need to be defined to quantitatively describe the performance of the design. The responses are then modeled parametrically by the Radial Basis Functions and utilized to formulate the optimization problems. The recognitions of the design uncertainties and the distributions of the random variables are also important for the formulation of the Reliability-Based Design Optimization problems. Once the probabilistic optimization problems are formulated, the Modified Reliability Index Approach can be used to find optimal designs with allowable failure probabilities. To sum up, the following summarize the key steps for applying the proposed method to design and optimize other thermal systems with design uncertainties:

- The design and execution of the experiments or the simulations.
- The definition of the responses.
- The formulation of the optimization problems.
- The recognition of the design uncertainties.

With the achievements of the above four key steps, the proposed system strategy can be applied to the specific thermal systems and find the optimal design variables with design uncertainties.

## **8.2. Future Work**

The proposed strategy of parametric modeling and optimization with design uncertainties can be applied to many other thermal systems, which have been well introduced in Chapter 1. In the future study of the CVD process, the proposed methodology can be applied to find the optimal operating conditions for the depositions of different materials, such as the high-hardness materials – boron nitride (BN), silicon carbide (SiC), boron carbide ( $B_4C$ ), and titanium nitride (TiN). Different reaction kinetics of the deposition should be studied. Different configurations of the CVD processes also can be considered with different hardware variables, such as the shape of the CVD chamber, the orientation of the susceptor, and the direction of the reactant flow.

Another focus for the future work should be devoted to the thermal systems that are related to the safety of human lives, the energy crisis, and the biotechnology. Especially for the system that requires high performance and cannot afford system failures, the operating conditions of the thermal systems should be determined by the proposed method. One of the examples is the next-generation design of the carbon fuel cells [128], where the efficiency for electricity production may be possibly higher than the traditional hydrogen fuel cells. The operating conditions of producing the carbon fuel cells differ the disorderedness of the carbon atoms, which is much related to the electricity yield.

In the viewpoint of the RBDO problems, there are many different kinds of statistical distributions for the random variables besides the normal distributions. In the

future study of the MRIA, the nonlinear transformations and the updating schemes should be studied for the other distributions, such as Weibull, Gumbel, and uniform distributions. Furthermore, the comparison between the MRIA and the other RBDO algorithms, such as the PMA and the SORA, can be studied. The comparison results will help the designers determine the RBDO algorithms for different applications of the thermal systems.

## Appendices

### *I. Detailed Information about the 437 Sampling Points*

**Table I.1. Responses of the 437 Sampling Points.**

V	T	PWA	MDR	RMS	KUR	V	T	PWA	MDR	RMS	KUR
0.1	400	80.39	8.886E-5	9.391E-7	3.305	0.15	800	81.86	8.879E-5	6.546E-7	3.457
0.1	450	80.39	8.608E-5	8.422E-7	3.409	0.15	850	81.37	8.760E-5	6.166E-7	3.549
0.1	500	80.39	8.373E-5	7.723E-7	3.546	0.15	900	80.88	8.653E-5	5.850E-7	3.642
0.1	550	79.90	8.176E-5	7.046E-7	3.671	0.15	950	80.88	8.556E-5	5.742E-7	3.817
0.1	600	79.41	8.007E-5	6.530E-7	3.801	0.15	1000	80.39	8.469E-5	5.518E-7	3.907
0.1	650	78.92	7.861E-5	6.137E-7	3.930	0.15	1050	79.90	8.390E-5	5.329E-7	3.990
0.1	700	78.43	7.735E-5	5.835E-7	4.050	0.15	1100	79.41	8.317E-5	5.169E-7	4.063
0.1	750	78.43	7.624E-5	5.777E-7	4.222	0.15	1150	79.41	8.250E-5	5.192E-7	4.222
0.1	800	77.94	7.527E-5	5.599E-7	4.313	0.15	1200	78.92	8.189E-5	5.075E-7	4.275
0.1	850	77.45	7.441E-5	5.467E-7	4.384	0.15	1250	78.43	8.133E-5	4.975E-7	4.316
0.1	900	76.96	7.365E-5	5.358E-7	4.436	0.15	1300	78.43	8.081E-5	5.050E-7	4.441
0.1	950	76.47	7.297E-5	5.279E-7	4.468	0.15	1350	77.94	8.033E-5	4.974E-7	4.459
0.1	1000	76.47	7.234E-5	5.395E-7	4.550	0.15	1400	77.45	7.989E-5	4.912E-7	4.467
0.1	1050	75.98	7.179E-5	5.348E-7	4.548	0.15	1450	77.45	7.947E-5	5.023E-7	4.554
0.1	1100	75.49	7.129E-5	5.312E-7	4.534	0.15	1500	76.96	7.908E-5	4.972E-7	4.542
0.1	1150	75.00	7.083E-5	5.285E-7	4.508	0.2	400	73.53	1.227E-4	1.105E-6	2.933
0.1	1200	75.00	7.040E-5	5.444E-7	4.531	0.2	450	79.41	1.180E-4	1.236E-6	2.929
0.1	1250	74.51	7.001E-5	5.427E-7	4.488	0.2	500	83.82	1.141E-4	1.292E-6	2.883
0.1	1300	74.51	6.964E-5	5.597E-7	4.492	0.2	550	85.29	1.109E-4	1.217E-6	2.850
0.1	1350	74.02	6.931E-5	5.584E-7	4.438	0.2	600	85.29	1.082E-4	1.100E-6	2.832
0.1	1400	73.53	6.899E-5	5.573E-7	4.380	0.2	650	85.29	1.058E-4	1.004E-6	2.837
0.1	1450	73.53	6.868E-5	5.749E-7	4.367	0.2	700	84.80	1.037E-4	9.088E-7	2.842
0.1	1500	73.04	6.840E-5	5.736E-7	4.305	0.2	750	84.80	1.019E-4	8.449E-7	2.891
0.15	400	78.43	1.071E-4	1.127E-6	3.028	0.2	800	84.31	1.002E-4	7.772E-7	2.926
0.15	450	81.37	1.033E-4	1.115E-6	3.027	0.2	850	84.31	9.875E-5	7.351E-7	3.021
0.15	500	82.84	1.002E-4	1.053E-6	3.042	0.2	900	83.82	9.742E-5	6.868E-7	3.080
0.15	550	82.84	9.757E-5	9.503E-7	3.060	0.2	950	83.33	9.622E-5	6.447E-7	3.145
0.15	600	82.84	9.531E-5	8.700E-7	3.105	0.2	1000	82.84	9.512E-5	6.088E-7	3.214
0.15	650	82.84	9.334E-5	8.062E-7	3.181	0.2	1050	82.84	9.410E-5	5.925E-7	3.370
0.15	700	82.35	9.164E-5	7.392E-7	3.243	0.2	1100	82.35	9.318E-5	5.657E-7	3.447
0.15	750	82.35	9.012E-5	7.005E-7	3.369	0.2	1150	81.86	9.233E-5	5.426E-7	3.523

**Table I.1. Responses of the 437 Sampling Points (Continued).**

V	T	PWA	MDR	RMS	KUR	V	T	PWA	MDR	RMS	KUR
0.2	1200	81.86	9.153E-5	5.370E-7	3.700	0.3	700	88.73	1.241E-4	1.251E-6	2.485
0.2	1250	81.37	9.079E-5	5.192E-7	3.770	0.3	750	88.24	1.217E-4	1.134E-6	2.456
0.2	1300	80.88	9.011E-5	5.037E-7	3.834	0.3	800	88.24	1.195E-4	1.041E-6	2.443
0.2	1350	80.88	8.946E-5	5.050E-7	4.007	0.3	850	87.75	1.176E-4	9.510E-7	2.431
0.2	1400	80.39	8.887E-5	4.928E-7	4.056	0.3	900	87.25	1.159E-4	8.742E-7	2.427
0.2	1450	79.90	8.831E-5	4.820E-7	4.097	0.3	950	87.25	1.142E-4	8.195E-7	2.460
0.2	1500	79.90	8.777E-5	4.877E-7	4.249	0.3	1000	86.76	1.128E-4	7.627E-7	2.474
0.25	400	69.12	1.364E-4	1.045E-6	2.867	0.3	1050	86.27	1.114E-4	7.108E-7	2.492
0.25	450	74.02	1.312E-4	1.145E-6	2.877	0.3	1100	86.27	1.102E-4	6.787E-7	2.571
0.25	500	83.33	1.265E-4	1.450E-6	2.834	0.3	1150	85.78	1.090E-4	6.396E-7	2.604
0.25	550	86.76	1.227E-4	1.450E-6	2.740	0.3	1200	85.29	1.079E-4	6.054E-7	2.641
0.25	600	87.25	1.196E-4	1.324E-6	2.687	0.3	1250	85.29	1.069E-4	5.882E-7	2.763
0.25	650	87.25	1.168E-4	1.201E-6	2.653	0.3	1300	84.80	1.060E-4	5.612E-7	2.808
0.25	700	86.76	1.144E-4	1.080E-6	2.627	0.3	1350	84.31	1.051E-4	5.372E-7	2.855
0.25	750	86.76	1.123E-4	9.947E-7	2.630	0.3	1400	84.31	1.042E-4	5.280E-7	3.006
0.25	800	86.27	1.104E-4	9.080E-7	2.629	0.3	1450	83.82	1.034E-4	5.089E-7	3.055
0.25	850	86.27	1.086E-4	8.488E-7	2.670	0.3	1500	83.82	1.027E-4	5.040E-7	3.226
0.25	900	85.78	1.071E-4	7.849E-7	2.692	0.35	400	64.22	1.603E-4	1.009E-6	2.793
0.25	950	85.29	1.057E-4	7.301E-7	2.722	0.35	450	67.65	1.539E-4	1.060E-6	2.802
0.25	1000	85.29	1.044E-4	6.963E-7	2.816	0.35	500	72.06	1.485E-4	1.154E-6	2.807
0.25	1050	84.80	1.032E-4	6.547E-7	2.862	0.35	550	89.22	1.432E-4	1.884E-6	2.619
0.25	1100	84.31	1.021E-4	6.185E-7	2.913	0.35	600	89.71	1.393E-4	1.708E-6	2.517
0.25	1150	83.82	1.011E-4	5.872E-7	2.967	0.35	650	89.71	1.360E-4	1.538E-6	2.441
0.25	1200	83.82	1.001E-4	5.727E-7	3.112	0.35	700	89.71	1.330E-4	1.394E-6	2.378
0.25	1250	83.33	9.923E-5	5.484E-7	3.172	0.35	750	89.71	1.304E-4	1.273E-6	2.333
0.25	1300	82.84	9.841E-5	5.272E-7	3.232	0.35	800	89.22	1.280E-4	1.152E-6	2.296
0.25	1350	82.84	9.763E-5	5.211E-7	3.401	0.35	850	88.73	1.259E-4	1.050E-6	2.268
0.25	1400	82.35	9.690E-5	5.039E-7	3.458	0.35	900	88.73	1.239E-4	9.748E-7	2.257
0.25	1450	82.35	9.621E-5	5.023E-7	3.636	0.35	950	88.24	1.222E-4	8.979E-7	2.245
0.25	1500	81.86	9.557E-5	4.886E-7	3.685	0.35	1000	88.24	1.205E-4	8.425E-7	2.261
0.3	400	66.67	1.489E-4	1.038E-6	2.830	0.35	1050	87.75	1.190E-4	7.836E-7	2.263
0.3	450	70.59	1.430E-4	1.103E-6	2.839	0.35	1100	87.25	1.176E-4	7.320E-7	2.270
0.3	500	76.47	1.380E-4	1.257E-6	2.835	0.35	1150	87.25	1.163E-4	6.976E-7	2.324
0.3	550	88.24	1.334E-4	1.679E-6	2.668	0.35	1200	86.76	1.151E-4	6.567E-7	2.341
0.3	600	88.73	1.298E-4	1.526E-6	2.586	0.35	1250	86.27	1.140E-4	6.211E-7	2.363
0.3	650	88.73	1.268E-4	1.377E-6	2.527	0.35	1300	86.27	1.129E-4	5.997E-7	2.452

**Table I.1. Responses of the 437 Sampling Points (Continued).**

V	T	PWA	MDR	RMS	KUR	V	T	PWA	MDR	RMS	KUR
0.35	1350	85.78	1.119E-4	5.712E-7	2.482	0.45	850	90.69	1.408E-4	1.241E-6	2.062
0.35	1400	85.78	1.110E-4	5.564E-7	2.599	0.45	900	90.69	1.385E-4	1.144E-6	2.021
0.35	1450	85.29	1.101E-4	5.335E-7	2.635	0.45	950	90.20	1.364E-4	1.049E-6	1.991
0.35	1500	84.80	1.093E-4	5.131E-7	2.670	0.45	1000	90.20	1.345E-4	9.762E-7	1.968
0.4	400	62.25	1.709E-4	9.873E-7	2.763	0.45	1050	89.71	1.328E-4	9.030E-7	1.950
0.4	450	65.69	1.641E-4	1.045E-6	2.777	0.45	1100	89.71	1.311E-4	8.476E-7	1.946
0.4	500	69.61	1.582E-4	1.123E-6	2.785	0.45	1150	89.22	1.296E-4	7.904E-7	1.937
0.4	550	75.00	1.531E-4	1.268E-6	2.779	0.45	1200	88.73	1.282E-4	7.398E-7	1.932
0.4	600	91.18	1.481E-4	1.908E-6	2.445	0.45	1250	88.73	1.268E-4	7.028E-7	1.951
0.4	650	91.18	1.445E-4	1.714E-6	2.359	0.45	1300	88.24	1.256E-4	6.626E-7	1.954
0.4	700	90.69	1.413E-4	1.532E-6	2.296	0.45	1350	88.24	1.244E-4	6.345E-7	1.992
0.4	750	90.69	1.384E-4	1.395E-6	2.236	0.45	1400	87.75	1.233E-4	6.022E-7	2.002
0.4	800	90.20	1.359E-4	1.260E-6	2.190	0.45	1450	87.75	1.222E-4	5.812E-7	2.062
0.4	850	90.20	1.335E-4	1.159E-6	2.152	0.45	1500	87.25	1.212E-4	5.551E-7	2.077
0.4	900	89.71	1.314E-4	1.060E-6	2.122	0.5	400	59.31	1.904E-4	9.587E-7	2.718
0.4	950	89.22	1.295E-4	9.737E-7	2.099	0.5	450	62.25	1.826E-4	1.003E-6	2.729
0.4	1000	89.22	1.277E-4	9.091E-7	2.090	0.5	500	65.20	1.760E-4	1.047E-6	2.733
0.4	1050	88.73	1.261E-4	8.429E-7	2.079	0.5	550	69.12	1.702E-4	1.135E-6	2.742
0.4	1100	88.73	1.246E-4	7.945E-7	2.093	0.5	600	74.51	1.652E-4	1.288E-6	2.734
0.4	1150	88.24	1.232E-4	7.427E-7	2.092	0.5	650	92.65	1.601E-4	1.994E-6	2.249
0.4	1200	87.75	1.219E-4	6.971E-7	2.096	0.5	700	92.16	1.565E-4	1.780E-6	2.177
0.4	1250	87.75	1.206E-4	6.657E-7	2.140	0.5	750	92.16	1.532E-4	1.616E-6	2.100
0.4	1300	87.25	1.195E-4	6.294E-7	2.152	0.5	800	91.67	1.503E-4	1.457E-6	2.046
0.4	1350	87.25	1.184E-4	6.063E-7	2.221	0.5	850	91.67	1.476E-4	1.334E-6	1.987
0.4	1400	86.76	1.173E-4	5.773E-7	2.241	0.5	900	91.18	1.452E-4	1.217E-6	1.949
0.4	1450	86.76	1.163E-4	5.606E-7	2.336	0.5	950	91.18	1.430E-4	1.124E-6	1.908
0.4	1500	86.27	1.154E-4	5.370E-7	2.361	0.5	1000	90.69	1.409E-4	1.034E-6	1.881
0.45	400	60.78	1.809E-4	9.771E-7	2.741	0.5	1050	90.69	1.391E-4	9.634E-7	1.856
0.45	450	63.73	1.736E-4	1.017E-6	2.749	0.5	1100	90.20	1.373E-4	8.935E-7	1.838
0.45	500	67.16	1.673E-4	1.079E-6	2.757	0.5	1150	90.20	1.357E-4	8.390E-7	1.828
0.45	550	71.57	1.619E-4	1.184E-6	2.762	0.5	1200	89.71	1.342E-4	7.839E-7	1.819
0.45	600	92.16	1.564E-4	2.080E-6	2.388	0.5	1250	89.71	1.327E-4	7.417E-7	1.823
0.45	650	91.67	1.525E-4	1.846E-6	2.308	0.5	1300	89.22	1.314E-4	6.978E-7	1.821
0.45	700	91.67	1.491E-4	1.666E-6	2.225	0.5	1350	88.73	1.301E-4	6.586E-7	1.822
0.45	750	91.18	1.460E-4	1.499E-6	2.167	0.5	1400	88.73	1.289E-4	6.300E-7	1.844
0.45	800	91.18	1.433E-4	1.367E-6	2.105	0.5	1450	88.24	1.278E-4	5.984E-7	1.851

**Table I.1. Responses of the 437 Sampling Points (Continued).**

V	T	PWA	MDR	RMS	KUR	V	T	PWA	MDR	RMS	KUR
0.5	1500	88.24	1.267E-4	5.764E-7	1.889	0.6	1000	92.16	1.529E-4	1.158E-6	1.769
0.55	400	58.33	1.993E-4	9.567E-7	2.704	0.6	1050	91.67	1.508E-4	1.069E-6	1.748
0.55	450	60.78	1.912E-4	9.826E-7	2.707	0.6	1100	91.67	1.488E-4	9.953E-7	1.719
0.55	500	63.73	1.842E-4	1.031E-6	2.715	0.6	1150	91.18	1.470E-4	9.252E-7	1.706
0.55	550	67.65	1.781E-4	1.123E-6	2.729	0.6	1200	91.18	1.453E-4	8.676E-7	1.688
0.55	600	71.57	1.728E-4	1.212E-6	2.724	0.6	1250	90.69	1.437E-4	8.119E-7	1.683
0.55	650	93.14	1.673E-4	2.120E-6	2.211	0.6	1300	90.69	1.422E-4	7.665E-7	1.674
0.55	700	93.14	1.635E-4	1.910E-6	2.118	0.6	1350	90.20	1.407E-4	7.218E-7	1.674
0.55	750	92.65	1.600E-4	1.715E-6	2.055	0.6	1400	90.20	1.394E-4	6.859E-7	1.674
0.55	800	92.65	1.569E-4	1.560E-6	1.984	0.6	1450	89.71	1.381E-4	6.498E-7	1.678
0.55	850	92.16	1.541E-4	1.415E-6	1.938	0.6	1500	89.71	1.369E-4	6.214E-7	1.686
0.55	900	92.16	1.515E-4	1.300E-6	1.884	0.65	400	55.88	2.162E-4	9.161E-7	2.665
0.55	950	91.67	1.492E-4	1.190E-6	1.852	0.65	450	58.82	2.072E-4	9.706E-7	2.679
0.55	1000	91.67	1.470E-4	1.102E-6	1.814	0.65	500	61.27	1.995E-4	1.003E-6	2.681
0.55	1050	91.18	1.451E-4	1.017E-6	1.792	0.65	550	64.22	1.929E-4	1.057E-6	2.689
0.55	1100	91.18	1.432E-4	9.494E-7	1.767	0.65	600	67.65	1.871E-4	1.132E-6	2.695
0.55	1150	90.69	1.415E-4	8.830E-7	1.753	0.65	650	72.55	1.819E-4	1.273E-6	2.695
0.55	1200	90.20	1.399E-4	8.243E-7	1.743	0.65	700	93.63	1.766E-4	2.105E-6	2.069
0.55	1250	90.20	1.383E-4	7.776E-7	1.734	0.65	750	93.63	1.728E-4	1.904E-6	1.983
0.55	1300	90.20	1.369E-4	7.363E-7	1.733	0.65	800	93.63	1.694E-4	1.729E-6	1.908
0.55	1350	89.71	1.355E-4	6.941E-7	1.733	0.65	850	93.14	1.663E-4	1.568E-6	1.865
0.55	1400	89.22	1.343E-4	6.565E-7	1.734	0.65	900	93.14	1.634E-4	1.437E-6	1.808
0.55	1450	89.22	1.330E-4	6.279E-7	1.748	0.65	950	92.65	1.609E-4	1.315E-6	1.779
0.55	1500	88.73	1.319E-4	5.973E-7	1.754	0.65	1000	92.65	1.585E-4	1.214E-6	1.737
0.6	400	57.35	2.079E-4	9.495E-7	2.690	0.65	1050	92.16	1.563E-4	1.120E-6	1.718
0.6	450	59.80	1.993E-4	9.788E-7	2.693	0.65	1100	92.16	1.542E-4	1.041E-6	1.689
0.6	500	62.75	1.920E-4	1.030E-6	2.703	0.65	1150	91.67	1.523E-4	9.672E-7	1.679
0.6	550	66.18	1.856E-4	1.104E-6	2.714	0.65	1200	91.67	1.505E-4	9.053E-7	1.660
0.6	600	69.61	1.801E-4	1.175E-6	2.712	0.65	1250	91.18	1.488E-4	8.467E-7	1.656
0.6	650	93.63	1.742E-4	2.241E-6	2.175	0.65	1300	91.18	1.472E-4	7.976E-7	1.645
0.6	700	93.63	1.701E-4	2.017E-6	2.080	0.65	1350	90.69	1.457E-4	7.506E-7	1.647
0.6	750	93.14	1.665E-4	1.811E-6	2.017	0.65	1400	90.69	1.443E-4	7.114E-7	1.644
0.6	800	93.14	1.633E-4	1.646E-6	1.943	0.65	1450	90.69	1.429E-4	6.765E-7	1.644
0.6	850	92.65	1.603E-4	1.493E-6	1.898	0.65	1500	90.20	1.416E-4	6.421E-7	1.651
0.6	900	92.65	1.576E-4	1.369E-6	1.842	0.7	400	55.39	2.240E-4	9.240E-7	2.659
0.6	950	92.16	1.552E-4	1.253E-6	1.810	0.7	450	57.84	2.147E-4	9.589E-7	2.663

**Table I.1. Responses of the 437 Sampling Points (Continued).**

V	T	PWA	MDR	RMS	KUR	V	T	PWA	MDR	RMS	KUR
0.7	500	60.29	2.067E-4	9.941E-7	2.668	0.75	1150	92.65	1.623E-4	1.050E-6	1.659
0.7	550	63.24	1.998E-4	1.051E-6	2.678	0.75	1200	92.65	1.603E-4	9.802E-7	1.645
0.7	600	66.18	1.938E-4	1.107E-6	2.681	0.75	1250	92.16	1.585E-4	9.163E-7	1.647
0.7	650	70.59	1.884E-4	1.229E-6	2.687	0.75	1300	92.16	1.568E-4	8.605E-7	1.641
0.7	700	94.12	1.828E-4	2.206E-6	2.038	0.75	1350	91.67	1.551E-4	8.093E-7	1.649
0.7	750	94.12	1.788E-4	1.994E-6	1.952	0.75	1400	91.67	1.536E-4	7.645E-7	1.649
0.7	800	93.63	1.752E-4	1.800E-6	1.901	0.75	1450	91.67	1.521E-4	7.241E-7	1.651
0.7	850	93.63	1.720E-4	1.642E-6	1.836	0.75	1500	91.18	1.507E-4	6.866E-7	1.663
0.7	900	93.14	1.691E-4	1.496E-6	1.802	0.8	400	53.92	2.390E-4	9.099E-7	2.637
0.7	950	93.14	1.663E-4	1.375E-6	1.755	0.8	450	56.37	2.290E-4	9.494E-7	2.642
0.7	1000	93.14	1.638E-4	1.268E-6	1.715	0.8	500	58.82	2.204E-4	9.892E-7	2.648
0.7	1050	92.65	1.615E-4	1.170E-6	1.699	0.8	550	61.27	2.130E-4	1.029E-6	2.653
0.7	1100	92.65	1.594E-4	1.086E-6	1.672	0.8	600	63.73	2.065E-4	1.068E-6	2.654
0.7	1150	92.16	1.574E-4	1.009E-6	1.664	0.8	650	67.16	2.008E-4	1.150E-6	2.663
0.7	1200	92.16	1.555E-4	9.430E-7	1.647	0.8	700	72.06	1.956E-4	1.299E-6	2.664
0.7	1250	91.67	1.538E-4	8.817E-7	1.647	0.8	750	94.61	1.902E-4	2.156E-6	1.922
0.7	1300	91.67	1.521E-4	8.291E-7	1.637	0.8	800	94.61	1.864E-4	1.956E-6	1.851
0.7	1350	91.18	1.505E-4	7.799E-7	1.642	0.8	850	94.12	1.829E-4	1.775E-6	1.814
0.7	1400	91.18	1.490E-4	7.378E-7	1.638	0.8	900	94.12	1.797E-4	1.623E-6	1.763
0.7	1450	91.18	1.476E-4	7.000E-7	1.638	0.8	950	93.63	1.768E-4	1.486E-6	1.741
0.7	1500	90.69	1.462E-4	6.640E-7	1.648	0.8	1000	93.63	1.741E-4	1.369E-6	1.707
0.75	400	54.41	2.317E-4	9.070E-7	2.642	0.8	1050	93.63	1.716E-4	1.265E-6	1.680
0.75	450	56.86	2.220E-4	9.443E-7	2.648	0.8	1100	93.14	1.692E-4	1.172E-6	1.675
0.75	500	59.31	2.137E-4	9.819E-7	2.654	0.8	1150	93.14	1.671E-4	1.090E-6	1.660
0.75	550	62.25	2.065E-4	1.041E-6	2.666	0.8	1200	92.65	1.650E-4	1.016E-6	1.662
0.75	600	65.20	2.003E-4	1.100E-6	2.672	0.8	1250	92.65	1.631E-4	9.503E-7	1.656
0.75	650	68.63	1.947E-4	1.180E-6	2.675	0.8	1300	92.65	1.613E-4	8.917E-7	1.654
0.75	700	75.00	1.897E-4	1.397E-6	2.664	0.8	1350	92.16	1.596E-4	8.386E-7	1.664
0.75	750	94.12	1.846E-4	2.070E-6	1.949	0.8	1400	92.16	1.580E-4	7.911E-7	1.668
0.75	800	94.12	1.809E-4	1.879E-6	1.875	0.8	1450	91.67	1.564E-4	7.482E-7	1.681
0.75	850	94.12	1.775E-4	1.713E-6	1.812	0.8	1500	91.67	1.550E-4	7.096E-7	1.690
0.75	900	93.63	1.745E-4	1.561E-6	1.781	0.85	400	52.94	2.462E-4	8.886E-7	2.620
0.75	950	93.63	1.716E-4	1.433E-6	1.736	0.85	450	55.88	2.358E-4	9.524E-7	2.636
0.75	1000	93.14	1.690E-4	1.317E-6	1.718	0.85	500	57.84	2.269E-4	9.720E-7	2.634
0.75	1050	93.14	1.666E-4	1.218E-6	1.687	0.85	550	60.29	2.193E-4	1.014E-6	2.639
0.75	1100	92.65	1.644E-4	1.128E-6	1.678	0.85	600	62.75	2.126E-4	1.055E-6	2.643



**Table I.1. Responses of the 437 Sampling Points (Continued).**

V	T	PWA	MDR	RMS	KUR	V	T	PWA	MDR	RMS	KUR
0.85	650	66.18	2.067E-4	1.140E-6	2.655	0.9	1300	93.14	1.700E-4	9.534E-7	1.699
0.85	700	69.61	2.014E-4	1.222E-6	2.652	0.9	1350	93.14	1.681E-4	8.961E-7	1.709
0.85	750	95.10	1.956E-4	2.238E-6	1.897	0.9	1400	92.65	1.664E-4	8.453E-7	1.724
0.85	800	94.61	1.917E-4	2.022E-6	1.853	0.9	1450	92.65	1.647E-4	7.985E-7	1.739
0.85	850	94.61	1.880E-4	1.842E-6	1.795	0.9	1500	92.16	1.631E-4	7.572E-7	1.755
0.85	900	94.12	1.847E-4	1.680E-6	1.769	0.95	400	52.45	2.598E-4	9.084E-7	2.616
0.85	950	94.12	1.817E-4	1.542E-6	1.730	0.95	450	54.41	2.488E-4	9.311E-7	2.613
0.85	1000	94.12	1.789E-4	1.420E-6	1.700	0.95	500	56.37	2.394E-4	9.544E-7	2.612
0.85	1050	93.63	1.763E-4	1.310E-6	1.693	0.95	550	58.82	2.313E-4	1.000E-6	2.621
0.85	1100	93.63	1.739E-4	1.214E-6	1.676	0.95	600	61.27	2.242E-4	1.045E-6	2.626
0.85	1150	93.14	1.717E-4	1.128E-6	1.677	0.95	650	63.73	2.179E-4	1.089E-6	2.629
0.85	1200	93.14	1.696E-4	1.052E-6	1.671	0.95	700	66.67	2.123E-4	1.154E-6	2.632
0.85	1250	93.14	1.676E-4	9.839E-7	1.669	0.95	750	71.08	2.073E-4	1.285E-6	2.633
0.85	1300	92.65	1.657E-4	9.226E-7	1.679	0.95	800	91.67	2.019E-4	2.106E-6	2.036
0.85	1350	92.65	1.639E-4	8.676E-7	1.685	0.95	850	91.18	1.981E-4	1.921E-6	1.993
0.85	1400	92.16	1.622E-4	8.183E-7	1.698	0.95	900	90.69	1.945E-4	1.760E-6	1.956
0.85	1450	92.16	1.606E-4	7.734E-7	1.709	0.95	950	90.20	1.913E-4	1.619E-6	1.924
0.85	1500	92.16	1.591E-4	7.329E-7	1.721	0.95	1000	90.20	1.883E-4	1.500E-6	1.872
0.9	400	52.45	2.531E-4	8.878E-7	2.613	0.95	1050	89.71	1.855E-4	1.390E-6	1.851
0.9	450	54.90	2.424E-4	9.312E-7	2.620	0.95	1100	89.71	1.829E-4	1.294E-6	1.813
0.9	500	57.35	2.332E-4	9.751E-7	2.628	0.95	1150	89.71	1.805E-4	1.208E-6	1.782
0.9	550	59.31	2.254E-4	9.967E-7	2.625	0.95	1200	89.71	1.783E-4	1.130E-6	1.759
0.9	600	62.25	2.184E-4	1.062E-6	2.639	0.95	1250	89.71	1.761E-4	1.059E-6	1.743
0.9	650	64.71	2.124E-4	1.104E-6	2.639	0.95	1300	93.14	1.741E-4	9.853E-7	1.723
0.9	700	68.14	2.069E-4	1.189E-6	2.643	0.95	1350	93.14	1.722E-4	9.258E-7	1.735
0.9	750	75.00	2.019E-4	1.437E-6	2.634	0.95	1400	93.14	1.704E-4	8.722E-7	1.751
0.9	800	92.16	1.969E-4	2.050E-6	1.999	0.95	1450	92.65	1.687E-4	8.251E-7	1.767
0.9	850	91.67	1.932E-4	1.868E-6	1.956	0.95	1500	92.65	1.671E-4	7.810E-7	1.786
0.9	900	91.18	1.897E-4	1.710E-6	1.920	1	400	51.47	2.664E-4	8.827E-7	2.599
0.9	950	90.69	1.866E-4	1.572E-6	1.890	1	450	53.92	2.551E-4	9.296E-7	2.607
0.9	1000	90.69	1.837E-4	1.454E-6	1.840	1	500	55.88	2.454E-4	9.547E-7	2.606
0.9	1050	90.69	1.810E-4	1.349E-6	1.799	1	550	58.33	2.370E-4	1.002E-6	2.615
0.9	1100	93.63	1.785E-4	1.255E-6	1.692	1	600	60.29	2.297E-4	1.027E-6	2.614
0.9	1150	93.63	1.761E-4	1.167E-6	1.685	1	650	62.75	2.233E-4	1.073E-6	2.618
0.9	1200	93.63	1.740E-4	1.088E-6	1.684	1	700	65.69	2.175E-4	1.140E-6	2.624
0.9	1250	93.14	1.719E-4	1.017E-6	1.693	1	750	69.61	2.124E-4	1.250E-6	2.628

**Table I.1. Responses of the 437 Sampling Points (Continued).**

<b>V</b>	<b>T</b>	<b>PWA</b>	<b>MDR</b>	<b>RMS</b>	<b>KUR</b>	<b>V</b>	<b>T</b>	<b>PWA</b>	<b>MDR</b>	<b>RMS</b>	<b>KUR</b>
1	800	91.18	2.068E-4	2.159E-6	2.076	1	1200	88.73	1.824E-4	1.167E-6	1.800
1	850	90.69	2.028E-4	1.972E-6	2.031	1	1250	88.73	1.802E-4	1.095E-6	1.778
1	900	90.20	1.992E-4	1.809E-6	1.993	1	1300	88.73	1.782E-4	1.030E-6	1.762
1	950	90.20	1.959E-4	1.673E-6	1.932	1	1350	88.73	1.762E-4	9.709E-7	1.753
1	1000	89.71	1.928E-4	1.545E-6	1.906	1	1400	88.73	1.743E-4	9.167E-7	1.751
1	1050	89.22	1.899E-4	1.432E-6	1.884	1	1450	93.14	1.726E-4	8.509E-7	1.794
1	1100	89.22	1.873E-4	1.335E-6	1.842	1	1500	93.14	1.709E-4	8.054E-7	1.815
1	1150	88.73	1.848E-4	1.245E-6	1.829						

## References

- [1] Y. Jaluria, *Design and Optimization of Thermal Systems*, McGraw-Hill, 1998.
- [2] Atomic Physics, Göteborg University. URL: <http://www.fy.chalmers.se>
- [3] J. Wang, Y. Dai, L. Gao, and S. Ma, "A New Combined Cooling, Heating and Power System Driven by Solar Energy," *Renewable Energy*, vol. 34, no. 12, pp. 2780-2788, 2009.
- [4] Y.-T. Yang and H.-S. Peng, "Numerical Study of the Heat Sink with Un-Uniform Fin Width Designs," *International Journal of Heat and Mass Transfer*, vol. 52, no. 15-16, pp. 3473-3480, 2009.
- [5] <http://www.tva.gov>.
- [6] V-2 Rocket Diagram. URL: <http://en.wikipedia.org>
- [7] <https://wiki-land.wikispaces.com>.
- [8] <http://www.summersmotors.co.uk>.
- [9] <http://www.wedotanks.com>.
- [10] <http://www.k2plumbing.com>.
- [11] G. J. Van Wylen and R. E. Sonntag, *Fundamentals of Classical Thermodynamics*, 3<sup>rd</sup> ed., Wiley, New York, 1986.
- [12] D. S. Steinberg, *Cooling Techniques for Electronic Equipment*, Wiley-Interscience, New York, 1980.
- [13] Y.-T. Yang and H.-S. Peng, "Numerical Study of Pin-Fin Heat Sink with Un-Uniform Fin Height Design," *International Journal of Heat and Mass Transfer*, vol. 51, no. 19-20, pp. 4788-4796, 2008.
- [14] W. F. Stoecker and J. W. Jones, *Refrigeration and Air Conditioning*, 2<sup>nd</sup> ed., McGraw-Hill, New York, 1982.
- [15] J. F. Kreider and A. Rabl, *Heating and Cooling of Buildings: Design for Efficiency*, McGraw-Hill, New York, 1994.
- [16] R. W. Fox and A. T. McDonald, *Introduction to Fluid Mechanics*, 4<sup>th</sup> ed., Wiley, New York, 1992.
- [17] W. M. Kays and A. L. London, *Compact Heat Exchangers*, McGraw-Hill, New York, 1984.
- [18] R. L. Mahajan, "Transport Phenomena in Chemical Vapor-Deposition Systems," *Advances in Heat Transfer*, vol. 28, pp. 339-425, Academic Press, 1996.
- [19] D. B. Fraser, "Metallization," *VLSI Technology*, S. M. Sze, Ed., p. 347, McGraw-Hill, New York, 1983.
- [20] C. T. Foxon, "Principles of Molecular Beam Epitaxy," *Handbook of Crystal Growth*, D. Hurlé, Ed., vol. 3a, Elsevier, Amsterdam, 1994.
- [21] <http://www.intel.com>.
- [22] <http://www.imec.be>.
- [23] <http://www.techeblog.com>.
- [24] "Lab Notes," *Gems & Gemology*, vol. 44, no. 1, pp. 67-69, 2008.
- [25] J. G. E. Gardeniers, W. E. J. R. Maas, R. Z. C. Van Meerten, and L. J. Giling, "Influence of Temperature on the Crystal Habit of Silicon in the Si-H-Cl CVD System: I. Experimental Results," *Journal of Crystal Growth*, vol. 96, pp. 821-842, 1989.

- [26] W. G. Breiland and M. E. Coltrin, "Si Deposition Rates in a Two-Dimensional CVD Reactor and Comparisons with Model Calculations," *Journal of The Electrochemical Society*, vol. 137, pp. 2313-2319, 1990.
- [27] A. Sherman, *Chemical Vapor Deposition for Microelectronics*, Noyes Publications, Park Ridge, New Jersey, USA, 1987.
- [28] D. I. Fotiadis, M. Boekholt, K. F. Jensen, and W. Richter, "Flow and Heat Transfer in CVD Reactors: Comparison of Raman Temperature Measurements and Finite Element Predictions," *Journal of Crystal Growth*, vol. 100, pp. 577-599, 1990.
- [29] J. R. Creighton and J. E. Parmeter, "Metal CVD for Microelectronic Applications: An Examination of Surface Chemistry and Kinetics," *Critical Reviews in Solid State and Materials Sciences*, vol. 18, pp. 175-238, 1993.
- [30] W. L. Gladfelter, "Selective Metallization by Chemical Vapor Deposition," *Chemistry of Materials*, vol. 5, pp. 1372-1388, 1993.
- [31] H. E. Rebenne and D. G. Bhat, "Review of CVD TiN Coatings for Wear-Resistant Applications: Deposition Processes, Properties and Performance," *Surface and Coatings Technology*, vol. 63, pp. 1-13, 1994.
- [32] H.-E. Cheng, M.-J. Chiang, and M.-H. Han, "Growth Characteristics and Properties of TiN Coating by Chemical Vapor Deposition," *Journal of The Electrochemical Society*, vol. 142, pp. 1573-1578, 1995.
- [33] H. E. Hintermann, "Advances and Development in CVD Technology," *Materials Science and Engineering*, vol. A209, pp. 366-371, 1996.
- [34] G. B. Stringfellow, "Fundamental Aspects of Organometallic Vapor Phase Epitaxy," *Materials Science and Engineering*, vol. B87, pp. 97-116, 2001.
- [35] S. Kurtz, D. Friedman, J. Geisz, and W. McMahon, "Using MOVPE Growth to Generate Tomorrow's Solar Electricity," *Journal of Crystal Growth*, vol. 298, pp. 748-753, 2007.
- [36] S. D. Allen, "Laser Chemical Vapor Deposition: A Technique for Selective Area Deposition," *Journal of Applied Physics*, vol. 52, no. 11, pp. 6501-6505, 1981.
- [37] J. G. Eden, "Photochemical Vapor Deposition," *Thin Film Processes II*, J. L. Vossen and W. Kern, Eds., Academic Press, Inc., San Diego, CA, 1991.
- [38] R. Naslain and F. Langlais, "CVD Processing of Ceramic-Ceramic Composite Materials," *Materials Science Research*, vol. 20, p. 145, 1986.
- [39] K. K. S. Lau, H. G. P. Lewis, S. J. Limb, M. C. Kwan, and K. K. Gleason, "Hot-Wire Chemical Vapor Deposition (HWCVD) of Fluorocarbon and Organosilicon Thin Films," *Thin Solid Films*, vol. 395, no. 1-2, pp. 288-291, 2001.
- [40] O. Nilsen, "Growth of Thin Films of Functional Oxides with the ALCVD Method," Doctor Scientiarum Thesis, Department of Chemistry, Faculty of Mathematics and Natural Sciences, University of Oslo, Norway, 2003.
- [41] P. George, "Simulation and Optimization of the Chemical Vapor Deposition Process," Ph.D Thesis, Mechanical and Aerospace Engineering, Rutgers University, New Brunswick, New Jersey, 2007.
- [42] P. T. Lin, Y. Jaluria, and H. C. Gea, "Parametric Modeling and Optimization of Chemical Vapor Deposition Process," *Journal of Manufacturing Science and Engineering*, vol. 131, no. 1, p. 011011, 2009.

- [43] I. Dimitrios, A. M. Kremer, D. R. McKenna, and K. F. Jensen, "Complex Flow Phenomena in Vertical MOCVD Reactors: Effects on Deposition Uniformity and Interface Abruptness," *Journal of Crystal Growth*, vol. 85, pp. 154-164, 1987.
- [44] K. F. Jensen, E. O. Einset, and D. I. Fotiadis, "Flow Phenomena in Chemical Vapor Deposition of Thin Films," *Annual Review of Fluid Mechanics*, vol. 23, pp. 197-232, 1991.
- [45] W. K. S. Chiu and Y. Jaluria, "Continuous Chemical Vapor Deposition Processing with a Moving Finite Thickness Susceptor," *Journal of Materials Research*, vol. 15, pp. 317-328, 2000.
- [46] W. K. S. Chiu, C. J. Richards, and Y. Jaluria, "Flow Structure and Heat Transfer in a Horizontal Converging Channel Heated From Below," *Physics of Fluids*, vol. 12, pp. 2128-2136, 2000.
- [47] G. Wahl, "Hydrodynamic Description of CVD (Chemical Vapour Deposition) Processes " *Thin Solid Films*, vol. 40, no. 1-3, pp. 13-26, 1977.
- [48] L. J. Giling, "Gas Flow Patterns in Horizontal Epitaxial Reactor Cells Observed by Interference Holography," *Journal of The Electrochemical Society*, vol. 129, no. 3, pp. 634-644, 1982.
- [49] C. A. Wang, S. H. Groves, S. C. Palmateer, D. W. Weyburne, and R. A. Brown, "Flow Visualization Studies for Optimization of OMVPE Reactor Design " *Journal of Crystal Growth*, vol. 77, no. 1-3, pp. 136-143, 1986.
- [50] F. C. Eversteyn, P. J. W. Severin, C. H. J. van den Brekel, and H. L. Peek, "A Stagnant Layer Model for the Epitaxial Growth of Silicon from Silane on a Horizontal Reactor," *Journal of The Electrochemical Society*, vol. 117, pp. 925-931, 1970.
- [51] K. Sugawara, "Silicon Epitaxial Growth by Rotating Disk Model," *Journal of The Electrochemical Society*, vol. 119, no. 12, pp. 1749-1760, 1972.
- [52] H. Moffat and K. F. Jensen, "Complex Flow Phenomena in MOCVD Reactors: I. Horizontal Reactors," *Journal of Crystal Growth*, vol. 77, pp. 108-119, 1986.
- [53] G. Evans and R. Greif, "A Numerical Model of the Flow and Heat Transfer in a Rotating Disk Chemical Vapor Deposition Reactor," *Journal of Heat Transfer*, vol. 109, pp. 928-935, 1987.
- [54] E. P. Visser, C. R. Kleijn, C. A. M. Govers, C. J. Hoogendoorn, and L. J. Giling, "Return Flows in Horizontal MOCVD Reactors Studied with the use of TiO<sub>2</sub> Particle Injection and Numerical Calculations," *Journal of Crystal Growth*, vol. 94, pp. 924-946, 1989.
- [55] J. Quazzani and F. Rosenberger, "Three- Dimensional Modeling of Horizontal Chemical Vapor Deposition I. MOCVD at Atmospheric Pressure," *Journal of Crystal Growth*, vol. 100, pp. 545-576, 1990.
- [56] R. L. Mahajan and C. Wei, "Buoyancy, Soret, Dufour, and Variable Property Effects in Silicon Epitaxy," *Journal of Heat Transfer*, vol. 113, pp. 688-695, 1991.
- [57] K. C. Karki, P. S. Sathiyamurthy, and S. V. Patankar, "Three-Dimensional Mixed Convection in a Horizontal Chemical Vapor Deposition Reactor," *Journal of Heat Transfer*, vol. 115, no. 3, pp. 803-806, 1993.
- [58] K. C. Karki, P. S. Sathiyamurthy, and S. V. Patankar, "Laminar Flow over a Confined Heated Disk: Effect of Buoyancy and Rotation," *ASME Heat Transfer Divison*, vol. 241, pp. 73-81, 1993.

- [59] R. J. Kee, A. Ting, and P. A. Spence, "Understanding and Improving Materials Processing Through Interpreting and Manipulating Predictive Models," *Chemical Vapor Deposition of Refractory Metals and Ceramics III*, Materials Research Society, vol. 363, p. 314, 1995.
- [60] W. K. S. Chiu and Y. Jaluria, "Effect of Buoyancy, Susceptor Motion, and Conjugate Transport in Chemical Vapor Deposition Systems," *Journal of Heat Transfer*, vol. 121, pp. 757-761, 1999.
- [61] W. K. S. Chiu, Y. Jaluria, and N. G. Glumac, "Numerical Simulation of Chemical Vapor Deposition Processes Under Variable and Constant Property Approximations," *Numerical Heat Transfer*, vol. 37, pp. 113-132, 2000.
- [62] W. K. S. Chiu, C. J. Richards, and Y. Jaluria, "Experimental and Numerical Study of Conjugate Heat Transfer in a Horizontal Channel Heated From Below," *Journal of Heat Transfer*, vol. 123, pp. 688-697, 2001.
- [63] H. Yoo and Y. Jaluria, "Thermal Aspects in the Continuous Chemical Vapor Deposition in Silicon," *Journal of Heat Transfer*, vol. 124, pp. 938-946, 2002.
- [64] Q. Wang, H. Yoo, and Y. Jaluria, "Convection in a Horizontal Duct under Constant and Variable Property Formulations," *International Journal of Heat and Mass Transfer*, vol. 46, pp. 297-310, 2003.
- [65] S. V. Patankar, *Numerical Heat Transfer and Fluid Flow*, Series in Computational Methods in Mechanics and Thermal Sciences, Hemisphere Publishing Corporation, 1980.
- [66] L. L. Raja, R. J. Kee, R. Serban, and L. R. Petzold, "Computational Algorithm for Dynamic Optimization of Chemical Vapor Deposition Processes in Stagnation Flow Reactors," *Journal of The Electrochemical Society*, vol. 147, no. 7, pp. 2718-2726, 2000.
- [67] B. Gebhart, Y. Jaluria, R. L. Mahajan, and B. Sammakia, *Buoyancy-Induced Flows and Transport*, Taylor & Francis, Philadelphia, PA, 1988.
- [68] R. E. Spall, "Unsteady Mixed Convection in Horizontal Ducts with Applications to Chemical Vapor Deposition Processes," *International Communications in Heat and Mass Transfer*, vol. 23, no. 1, pp. 115-122, 1996.
- [69] D. D. Gray and A. Giorgini, "The Validity of the Boussinesq Approximation for Liquids and Gases," *International Journal of Heat and Mass Transfer*, vol. 19, pp. 545-551, 1976.
- [70] W. K. S. Chiu and Y. Jaluria, "Heat Transfer in Horizontal and Vertical CVD Reactors," *ASME Heat Transfer Division*, vol. 347, pp. 293-311, 1997.
- [71] J. Quazzani, K. C. Chiu, and F. Rosenberger, "On the 2D Modelling of Horizontal CVD Reactors and Its Limitations," *Journal of Crystal Growth*, vol. 91, pp. 497-508, 1988.
- [72] W. K. S. Chiu, Y. Jaluria, and N. G. Glumac, "Control of Thin Film Growth In Chemical Vapor Deposition Manufacturing Systems: A Feasibility Study," *Journal of Manufacturing Science and Engineering*, vol. 124, pp. 715-724, 2002.
- [73] M.-J. Mouche, J.-L. Mermet, F. Pires, E. Richard, J. Torres, J. Palleau, and F. Braud, "Process Optimization of Copper MOCVD Using Modeling Experimental Design," *Applied Surface Science*, vol. 91, pp. 129-133, 1995.
- [74] R. P. Southwell, M. A. Mendicino, and E. G. Seebauer, "Optimization of Selective  $\text{TiSi}_2$  Chemical Vapor Deposition by Mechanistic Chemical Kinetics,"

- The Journal of Vacuum Science and Technology A*, vol. 14, no. 3, pp. 928-934, 1996.
- [75] W. K. S. Chiu, "Simulation, Design and Optimization of Chemical Vapor Deposition systems for Advanced Materials," Ph.D Thesis, Mechanical and Aerospace Engineering, Rutgers University, New Brunswick, New Jersey, 1999.
  - [76] H. V. Ly and H. T. Tran, "Proper Orthogonal Decomposition for Flow Calculations and Optimal Control in a Horizontal CVD Reactor," *Quarterly of Applied Mathematics*, vol. 60, no. 4, pp. 631-656, 2002.
  - [77] T. O. Mitchell, J. L. Hoyt, and J. F. Gibbons, "Substitutional Carbon Incorporation in Epitaxial  $\text{Si}_{1-y}\text{C}_y$  Layers Grown by Chemical Vapor Deposition," *Applied Physics Letters*, vol. 71, no. 12, pp. 1688-1690, 1997.
  - [78] D. G. Goodwin, "Scaling Laws for Diamond Chemical Vapor Deposition. I. Diamond Surface Chemistry," *Journal of Applied Physics*, vol. 74, no. 11, pp. 6888-6894, 1993.
  - [79] FLUENT 6.1 Documentation.
  - [80] Mixture database, FLUENT 6.2.16.
  - [81] D. N. Joanes and C. A. Gill, "Comparing Measures of Sample Skewness and Kurtosis," *Journal of the Royal Statistical Society (Series D): The Statistician*, vol. 47, no. 1, pp. 183-189, 1998.
  - [82] W. C. M. van Beers and J. P. C. Kleijnen, "Kriging for Interpolation in Random Simulation," *Journal of the Operational Research Society*, vol. 54, no. 3, pp. 255-262, 2003.
  - [83] W. C. M. van Beers and J. P. C. Kleijnen, "Kriging Interpolation in Simulation: A Survey," *Proceedings of the 36<sup>th</sup> Conference on Winter Simulation*, R. G. Ingalls, et al., Eds., pp. 113-121, 2004.
  - [84] M. E. Mortenson, *Geometric Modeling*, 3<sup>rd</sup> ed., Industrial Press Inc., New York, 2006.
  - [85] R. H. Myers, D. C. Montgomery, and C. M. Anderson-Cook, *Response Surface Methodology: Process and Product Optimization Using Designed Experiments*, Wiley Series in Probability and Statistics, 3<sup>rd</sup> ed., John Wiley & Sons, Inc., Hoboken, New Jersey, 2009.
  - [86] L. Lebensztajn, C. A. R. Marretto, M. C. Costa, and J.-L. Coulomb, "Kriging: A Useful Tool for Electromagnetic Device Optimization," *IEEE Transaction on Magnetics*, vol. 40, no. 2, pp. 1196-1199, 2004.
  - [87] T. W. Simpson, J. D. Peplinski, P. N. Koch, and J. K. Allen, "Metamodels for Computer-Based Engineering Design: Survey and Recommendations," *Engineering with Computers*, vol. 17, pp. 129-150, 2001.
  - [88] P. Giesl, "Construction of Global Lyapunov Functions Using Radial Basis Functions," *Lecture Notes in Mathematics*, C. J.-M. Morel, et al., Eds., Springer-Verlag Berlin Heidelberg, 2007.
  - [89] H. Wendland, "Piecewise Polynomial, Positive Definite and Compactly Supported Radial Functions of Minimal Degree," *Advances in Computational Mathematics*, vol. 4, no. 1, pp. 389-396, 1995.
  - [90] D. den Hertog, J. P. C. Kleijnen, and A. Y. D. Siem, "The Correct Kriging Variance Estimated by Bootstrapping," *Journal of the Operational Research Society*, vol. 57, no. 4, pp. 400-409, 2006.

- [91] J. Duchon, "Splines Minimizing Rotation-Invariant Semi-Norms in Sobolev Spaces," *Constructive Theory of Functions of Several Variables*, Lecture Notes in Mathematics, W. Schempp and K. Zeller, Eds., vol. 571, pp. 85-100, Springer Berlin / Heidelberg, 1977.
- [92] S. Jeong, M. Murayama, and K. Yamamoto, "Efficient Optimization Design Method Using Kriging Model " in *42<sup>nd</sup> AIAA Aerospace Sciences Meeting and Exhibit*, Reno, NV, 2004.
- [93] M. Stein, "Large Sample Properties of Simulations Using Latin Hypercube Sampling," *Technometrics*, vol. 29, no. 2, p. 143, 1987.
- [94] C. A. Cornell, "A Probability-Based Structural Code," *Journal of the American Concrete Institute*, vol. 66, no. 12, pp. 974-985, 1969.
- [95] H. O. Madsen, S. Krenk, and N. C. Lind, *Methods of Structural Safety*, Prentice-Hall, Englewood Cliffs, NJ, 1986.
- [96] A. Charnes and W. W. Cooper, "Chance Constrained Programming," *Management Science*, vol. 6, pp. 73-79, 1959.
- [97] J. W. Davidson, L. P. Felton, and G. C. Hart, "Optimum Design of Structures with Random Parameters," *Computers & Structures*, vol. 7, pp. 481-486, 1977.
- [98] S. S. Rao, "Structural Optimization by Chance Constrained Programming Techniques," *Computers & Structures*, vol. 12, pp. 777-781, 1980.
- [99] S. F. Jozwiak, "Minimum Weight Design of Structures with Random Parameters," *Computers & Structures*, vol. 23, pp. 481-485, 1986.
- [100] E. Nikolaidis and R. Burdisso, "Reliability Based Optimization: A Safety Index Approach," *Computers & Structures*, vol. 28, no. 6, pp. 781-788, 1988.
- [101] M. V. Reddy, R. V. Grandhi, and D. A. Hopkins, "Reliability Based Structural Optimization: A Simplified Safety Index Approach," *Computers & Structures*, vol. 53, no. 6, pp. 1407-1418, 1994.
- [102] B. D. Youn and K. K. Choi, "Selecting Probabilistic Approaches for Reliability-Based Design Optimization," *AIAA Journal*, vol. 42, no. 1, pp. 124-131, 2004.
- [103] D. Veneziano, *Contributions to Second-Moment Reliability Theory*, Department of Civil Engineering, Massachusetts Institute of Technology, Cambridge, MA, 1974.
- [104] A. M. Hasofer and N. C. Lind, "Exact and Invariant Second-Moment Code Format," *Journal of the Engineering Mechanics Division*, vol. 100, no. EM1, pp. 111-121, 1974.
- [105] R. Rackwitz and B. Fiessler, "Structural Reliability under Combined Random Load Sequences," *Computers & Structures*, vol. 9, pp. 489-494, 1978.
- [106] B. M. Ayyub and A. Haldar, "Practical Structural Reliability Techniques," *Journal of Structural Engineering*, vol. 110, no. 8, pp. 1707-1724, 1984.
- [107] L. P. Wang and R. V. Grandhi, "Efficient Safety Index Calculation for Structural Reliability Analysis," *Computers & Structures*, vol. 52, no. 1, pp. 103-111, 1994.
- [108] Y. T. Wu, O. H. Burnside, and T. A. Cruse, "Probabilistic Methods for Structural Response Analysis," *Computational Mechanics of Probabilistic and Reliability Analysis*, W. K. Lam and T. Belytschko, Eds., pp. 181-196, Elsevier Press International, Lausanne, Switzerland, 1989.
- [109] J. Tu, K. K. Choi, and Y. H. Park, "A New Study on Reliability Based Design Optimization," *Journal of Mechanical Design*, vol. 121, pp. 557-564, 1999.



- [110] Y. T. Wu, H. R. Millwater, and T. A. Cruse, "Advanced Probabilistic Structural Analysis Method for Implicit Performance Function," *AIAA Journal*, vol. 28, no. 9, pp. 1663-1669, 1990.
- [111] Y. T. Wu, "Computational Methods for Efficient Structural Reliability and Reliability Sensitivity Analysis," *AIAA Journal*, vol. 32, no. 8, pp. 1717-1723, 1994.
- [112] B. D. Youn, K. K. Choi, and Y. H. Park, "Hybrid Analysis Method for Reliability-Based Design Optimization," *Journal of Mechanical Design*, vol. 125, pp. 221-232, 2003.
- [113] X. Du and W. Chen, "Sequential Optimization Reliability Assessment Method for Efficient Probabilistic Design," *Journal of Mechanical Design*, vol. 126, pp. 225-233, 2004.
- [114] I. Enevoldsen, "Reliability-Based Optimization as an Information Tool," *Mechanics of Structures and Machines*, vol. 22, no. 1, pp. 117-135, 1994.
- [115] I. Enevoldsen and J. D. Sorensen, "Reliability-Based Optimization in Structural Engineering," *Structural Safety*, vol. 15, pp. 169-196, 1994.
- [116] S. V. L. Chandu and R. V. Grandhi, "General Purpose Procedure for Reliability Based Structural Optimization under Parametric Uncertainties," *Advances in Engineering Software*, vol. 23, pp. 7-14, 1995.
- [117] D. M. Frangopol and R. B. Corotis, "Reliability-Based Structural System Optimization: State-of-the-Art versus State-of-Practice," *Analysis and Computation: Proceedings of the 12<sup>th</sup> Conference held in Conjunction with Structures Congress XIV*, F. Y. Cheng, Ed., pp. 67-78, 1996.
- [118] Y. T. Wu and W. Wang, "A New Method for Efficient Reliability-Based Design Optimization," *Probabilistic Mechanics & Structural Reliability. Proceedings of the 7th Special Conference*, D. M. Frangopol and M. D. Grigoriu, Eds., pp. 274-277, 1996.
- [119] A. D. S. Carter, *Mechanical Reliability and Design*, Wiley, New York, 1997.
- [120] R. V. Grandhi and L. P. Wang, "Reliability-Based Structural Optimization Using Improved Two-Point Adaptive Nonlinear Approximations," *Finite Elements in Analysis and Design*, vol. 29, pp. 35-48, 1998.
- [121] B. D. Youn and K. K. Choi, "An Investigation of Nonlinearity of Reliability-Based Design Optimization Approaches," *Journal of Mechanical Design*, vol. 126, no. 3, pp. 403-411, 2004.
- [122] R. J. Yang and L. Gu, "Experience with Approximate Reliability-Based Optimization Methods," *Structural and Multidisciplinary Optimization*, vol. 26, no. 2, pp. 152-159, 2004.
- [123] H. C. Gea and K. Oza, "Two-Level Approximation Method for Reliability-Based Design Optimisation," *International Journal of Materials and Product Technology*, vol. 25, no. 1/2/3, pp. 99-111, 2006.
- [124] G. Cheng, L. Xu, and L. Jiang, "A Sequential Approximate Programming Strategy for Reliability-Based Structural Optimization," *Computers & Structures*, vol. 84, no. 21, pp. 1353-1367, 2006.
- [125] P. Yi, G. Cheng, and L. Jiang, "A Sequential Approximate Programming Strategy for Performance-Measure-Based Probabilistic Structural Design Optimization," *Structural Safety*, vol. 30, no. 2, pp. 91-109, 2008.

- [126] P. Yi and G. Cheng, "Further Study on Efficiency of Sequential Approximate Programming for Probabilistic Structural Design Optimization," *Structural and Multidisciplinary Optimization*, vol. 35, no. 6, pp. 509-522, 2008.
- [127] R. C. Jaeger, *Introduction to Microelectronic Fabrication*, Modular Series on Solid State Devices, 2<sup>nd</sup> ed., vol. 5, Prentice-Hall, Inc., Upper Saddle River, New Jersey, 2002.
- [128] M. Steinberg, J. F. Cooper, and N. Cherepy, "High Efficiency Direct Carbon and Hydrogen Fuel Cells for Fossil Fuel Power Generation," presented at the Conference: American Institute of Chemical Engineers 2002 Spring Meeting, New Orleans, LA, 2002.
- [129] P. T. Lin, Y. Jaluria, and H. C. Gea, "Parametric Modeling and Optimization of Chemical Vapor Deposition Process," in *2008 ASME International Design Engineering Technical Conferences & Computers and Information in Engineering Conference (IDETC/CIE)*, New York City, NY, USA, pp. DETC2008-50054, 2008.
- [130] P. T. Lin, H. C. Gea, and Y. Jaluria, "A Modified Reliability Index Approach for Reliability-Based Design Optimization," in *2009 ASME International Design Engineering Technical Conferences & Computers and Information in Engineering Conference (IDETC/CIE)*, San Diego, CA, USA, pp. DETC2009-87804, 2009.
- [131] P. T. Lin, H. C. Gea, and Y. Jaluria, "A Modified Reliability Index Approach for Reliability-Based Design Optimization," *submitted to Journal of Mechanical Design*.

## Acknowledgment for Previous Publications

The studies presented in Chapters 2 – 4 have appeared in the following:

- *Po Ting Lin, Yogesh Jaluria, and Hae Chang Gea, "Parametric Modeling and Optimization of Chemical Vapor Deposition Process," in 2008 ASME International Design Engineering Technical Conferences & Computers and Information in Engineering Conference (IDETC/CIE), New York City, NY, USA, 2008, DETC2008-50054. [129]*
- *Po Ting Lin, Yogesh Jaluria, and Hae Chang Gea, "Parametric Modeling and Optimization of Chemical Vapor Deposition Process," Journal of Manufacturing Science and Engineering, vol. 131, p. 011011, 2009. [42]*

The studies presented in Chapters 5 – 7 have appeared in the following:

- *Po Ting Lin, Hae Chang Gea, and Yogesh Jaluria, "A Modified Reliability Index Approach for Reliability-Based Design Optimization," in 2009 ASME International Design Engineering Technical Conferences & Computers and Information in Engineering Conference (IDETC/CIE), San Diego, CA, USA, DETC2009-87804. [130]*
- *Po Ting Lin, Hae Chang Gea, and Yogesh Jaluria, "A Modified Reliability Index Approach for Reliability-Based Design Optimization," submitted to Journal of Mechanical Design. [131]*

# Index

## C

chemical reactions ..... 2, 12, 22, 34  
     Arrhenius rate ..... 23, 30  
 Chemical Vapor Deposition ..... 8, 11  
     applications ..... 13  
     configuration of CVD reactors . 16, 22, 23, 29,  
     34  
     materials ..... 15, 70  
     optimization of CVD processes ..... 23, 61  
     responses ..... 20  
     sequence of steps ..... 11  
     types of CVD processes ..... 14  
 CVD of silicon ..... 14, 30, 69  
     hydrogen ..... 30, 34  
     silane ..... 30, 34, 69

## D

design uncertainties ..... 3, 23, 71, 74  
 design variables ..... 20, 24  
     hardware settings ..... 20  
     inlet velocity ..... 20, 23, 31, 34, 52, 69, 71  
     operating conditions ..... 20, 24, 29, 61, 129  
     operating temperature ..... 34, 36  
     susceptor temperature ... 20, 23, 31, 34, 52, 69,  
     71  
 dimensionless numbers  
     Grashof number ..... 22  
     Nusselt number ..... 21  
     Reynolds number ..... 22

## E

energy conversion ..... 1, 8, 10  
 experiments of CVD processes ..... 19, 21, 23  
     holography observation ..... 21  
 experiments of CVD processes ..... 35

## F

failure probabilities ..... 71, 75, 94, 129  
 fluid mechanics ..... 2, 10, 19, 20, 22

## G

governing equations ..... 31  
     continuity conservation ..... 22, 30  
     elliptic equations ..... 22  
     energy conservation ..... 30  
     momentum conservation ..... 22, 30  
     parabolic equations ..... 22  
     species transportation ..... 30

## H

heat transfer ..... 2, 4, 8, 9, 11, 19, 20, 21, 22

## K

Kronecker delta ..... 93

## L

Lagrangian Multiplier ..... 93

## M

mass transfer ..... 2, 10  
 Monte Carlo Simulation ..... 71, 76, 107, 113, 129  
 Most Probable Point ..... 80, 82, 87, 92, 96  
     Advanced First-Order Second-Moment  
     method *See* First-Order Reliability Method  
     First-Order Reliability Method ..... 82, 84  
     HL-RF algorithm ... *See* First-Order Reliability  
     Method  
     Normal Tail Approximation ..... 82  
     Second-Order Reliability Method ..... 83  
     sensitivity ..... 96

## N

numerical results of CVD processes ..... 35  
     deposition profile ..... 32, 37  
     streamlines ..... 32  
     temperature distribution ..... 32

## O

optimization ..... 2, 24  
     convexity ..... 63  
     deterministic optimization ..... 3, 25, 74  
     fmincon ..... 62, 84  
     non-deterministic optimization ..... 3  
     penalty function ..... 62  
     probabilistic optimization ..... 71, 74, 87, 95

## P

parametric modeling ..... 2, 19, 24  
     best fitting ..... 45, 47, 49  
     covariance functions ..... 49, 50  
     Euclidean distance ..... 50, 52  
     curve fitting ..... 45  
     exact fitting ..... 45, 48, 49  
     geometric modeling ..... 50  
     Least Square Approximation ..... 48, 54  
     metamodeling ..... 45  
     Response Surface Method ..... 24, 45  
     Kriging ..... 48  
     Polynomial Response Surface ..... 45, 47, 54  
     Radial Basis Function ..... 45, 50, 52  
 Physical Vapor Deposition ..... 12  
 Probability Density Function ..... 75, 79, 87

**R**

random variables .....	71, 74
expected value .....	74
lognormal distribution .....	105, 120
non-normal distribution .....	24, 105
normal distribution .....	24, 71, 87, 98, 113
standard deviation.....	74
reliability index .....	75, 84, 86
allowable reliability index .....	78, 87, 95
Cornell reliability index.....	75
First-Order Second-Moment method.....	76
Hasofer-Lind reliability index .....	80, 87
Mean-Value First-Order Second-Moment method .....	77, 78
modified reliability index .....	92, 113
Veneziano reliability index.....	79
Reliability-Based Design Optimization.....	24, 74, 92, 112
Approximate Moment Approach.....	78
Chance Constrained Programming .....	77
Modified Reliability Index Approach.....	24, 92, 95, 113
Performance Measure Approach .....	85, 86
Safety Index Approach .....	<i>See</i> Traditional Reliability Index Approach
Sequential Optimization and Reliability Assessment .....	85
three-sigma criterion.....	114
Traditional Reliability Index Approach .....	24, 79, 86, 92
responses .....	19, 24, 29, 37
deposition rate .....	39, 61
kurtosis .....	21, 42, 61
root mean square.....	21, 40, 61
uniformity .....	<i>See</i> root mean square and kurtosis
working area .....	37
effective working area .....	38, 40
isolated working area.....	38

percentage of working area .....	38, 61
----------------------------------	--------

**S**

simulations of CVD processes.....	19, 21, 23, 29
boundary conditions.....	20, 31
Boussinesq approximations .....	22
Buoyancy effect .....	22
constant properties .....	22
Coupled algorithm .....	31
FLUENT.....	29, 30, 31, 34, 35, 63
laminar finit-rate model .....	30
mass diffusivity of silane .....	35, 36
PISO algorithm .....	31
power-law discretization scheme .....	31
quad meshes.....	32
sampling nodes .....	40
silane mass fraction.....	31, 34
variable properties .....	22
Standard Normal Cumulative Distribution Function.....	75, 78, 79, 87

**T**

Taylor expansion .....	76, 82, 83, 84, 95
thermal efficiency .....	8
thermal systems .....	1, 3, 24
aerospace .....	1, 4, 9
air conditioning.....	1, 4, 10
automobiles.....	2
chemical processing.....	1
cooling systems.....	4, 8
energy systems.....	4, 8
environmental and safety systems .....	4, 9
fluid flow systems.....	4, 10
material processing .....	1, 4, 8
power systems.....	1
transportation systems .....	4, 10
thermodynamics .....	8, 10

## Curriculum Vitae

Po Ting Lin

- 1999 – 2003 Bachelor of Science, Department of Mechanical Engineering, National Central University, Jhongli City, Taiwan
- 2001 – 2003 Machine Assembler, Shin-I Machinery Works, Co., LTD., Taichung, Taiwan
- 2003 – 2004 CAD Designer, Shin-I Machinery Works, Co., LTD., Taichung, Taiwan
- 2004 – 2007 Master of Science, Department of Mechanical and Aerospace Engineering, Rutgers University, New Brunswick, New Jersey, USA
- 2004 – 2009 CAD Instructor, Department of Mechanical and Aerospace Engineering, Rutgers University, New Brunswick, New Jersey, USA

### Publications

1. Po Ting Lin, Hae Chang Gea, Yogesh Jaluria, “A Modified Reliability Index Approach for Reliability-Based Design Optimization,” submitted to *Journal of Mechanical Design*.
2. Po Ting Lin, Hae Chang Gea, Yogesh Jaluria, “A Modified Reliability Index Approach for Reliability-Based Design Optimization,” *ASME 2009 International Design Engineering Technical Conferences & Computers and Information in Engineering Conference (IDETC/CIE 2009)*, DETC2009-87804.
3. Pradeep George, Po Ting Lin, Hae Chang Gea, Yogesh Jaluria, “Reliability-Based Optimisation of Chemical Vapor Deposition Process,” *International Journal of Reliability and Safety*, Vol. 3, No. 4, pp. 363-383, 2009.
4. Po Ting Lin, Yogesh Jaluria, Hae Chang Gea, “Parametric Modeling and Optimization of Chemical Vapor Deposition Process,” *Journal of Manufacturing Science and Engineering*, Vol. 131, No. 1, pp. 011011, 2009.
5. Po Ting Lin, Yogesh Jaluria, Hae Chang Gea, “Parametric Modeling and Optimization of Chemical Vapor Deposition Process,” *ASME 2008 International Design Engineering Technical Conferences & Computers and Information in Engineering Conference (IDETC/CIE 2008)*, DETC2008-50054.
6. Yen Wen Lu, Po Ting Lin, “Bonding Characterization of Polydimethylsiloxane (PDMS) Elastomer with Nanoscale Features,” *1<sup>st</sup> Annual IEEE International Conference on Nano/Molecular Medicine and Engineering, IEEE-NANOMED 2007*.
7. Yen Wen Lu, Po Ting Lin, Chien Shing Pai, “Polydimethylsiloxane (PDMS) Bonding Strength Characterization by a Line Force Model in Blister Tests,” *The 14<sup>th</sup> International Conference on Solid-State Sensors, Actuators and Microsystems, Transducers & Eurosensors 2007*, pp. 2095-2098.
8. Po Ting Lin, Yen Wen Lu “A Line Force Model to Measure the Strength of Polydimethylsiloxane (PDMS)-to-PDMS Bonding Using Blister Tests,” *2007 NSTI Nanotechnology Conference and Trade Show, Nanotech 2007*.
9. Yen Wen Lu, Ching Jui Chang, Po Ting Lin, Hae Chang Gea, “Negative-Poisson's-Ratio Microstructural Material by Soft-Joint Mechanism,” *2006 NSTI Nanotechnology Conference and Trade Show, Nanotech 2006*.